UNIVERSITA' DEGLI STUDI DI BOLOGNA

FACULTY OF ELECTRICAL ENGINEERING
SCIENTIFIC FIELD ING-IND/31
XXII CYCLE

Diagnostic Techniques for MHD in Hypersonic Flows

PhD Thesis
Veronica Maria Granciu

Advisor:
Chiar.mo Prof.
CARLO ANGELO BORGHI

Second Advisor:
Prof.
ANDREA CRISTOFOLINI

Ph.D. Coordinator:
Chiar.mo Prof.
FRANCESCO NEGRINI

Bologna, March 2010

UNIVERSITA’ DEGLI STUDI DI BOLOGNA

FACULTY OF ELECTRICAL ENGINEERING
SCIENTIFIC FIELD ING-IND/31
XXII CYCLE

Diagnostic Techniques for MHD in Hypersonic Flows

PhD Thesis
Veronica Maria Granciu

Advisor:
Chiar.mo Prof.
CARLO ANGELO BORGHI

Second Advisor:
Prof.
ANDREA CRISTOFOLINI

Ph.D. Coordinator:
Chiar.mo Prof.
FRANCESCO NEGRINI

Bologna, March 2010

ACKNOWLEDGEMENTS

I would like to express my heartfelt gratitude to my advisors Professor Carlo Borghi and Professor Andrea Cristofolini for excellent guidance and motivation. Their encouragement and understanding during the study has been a source of inspiration for me.

My special thank belongs to my lab co-worker Gabriele, who gave me the first live taste of the beauty plasma research. It was a very great experience to work with him. Thanks Hugo!

I'm also grateful to my colleagues Chiara and Fabio, "i plasmatici", for their suggestions and moral support.

In conclusion, I wish to dedicate this work to my family and to Marco, who offer me courage, hope and a lot of patience. Without his love, I never would have made it. Thank you for believing in me.

Index

PART I

Diagnostic procedures theory

Chapter 1

Microwave Transmission System

Chapter 2

Spectroscopic Diagnostics

Chapter 3

Electrostatic Probes

PART II

Diagnostics in MHD experiments

Chapter 4

Fundamentals of MHD

Chapter 5

Non-intrusive Nozzle Characterization

Chapter 6

MHD Hypersonically Bodies

PART III

Langmuir Probe technique

Chapter 7

A New Development of the LP Approach

PART I

Diagnostic techniques theory

CHAPTER 1

MICROWAVE TRANSMISSION SYSTEM

1.1 Introduction

Microwaves were not studies until the Second World War, when high power microwave sources became available as the result of research on radio and radar detection.

Now, microwave area is more wider, found in communications, satellite transmission, navigation, cellular and broadcast television, bluetooth, wireless LAN or cable TV, commercial and consumer heating, drying ovens, avionics, military and medical application.

Microwaves can be use also to transmit power over long distance. NASA for 10 years worked to research the possibilities of using solar power satellite systems with large solar arrays that would beam power down to the earth’s surface via microwaves.

1.2 Electromagnetic waves in collisionless plasmas

The plasma frequency is of fundamental importance with regard to the behaviour of the plasma as a medium for the propagation of an electromagnetic wave. It is in fact possible to determine two different conditions.

Considering a collisionless plasma, if the electromagnetic wave frequency ω is lower than the plasma frequency $(\omega \prec \omega_p)$ the free electrons interact with the electric field of the incident wave and are able to rearrange themselves. The electromagnetic wave (i.e. the disturbance) does not propagate beyond the point in which it exists.

If $\omega_p \prec \omega$, there is no interaction between electrons and wave, and a lossless propagation occurs.

If we consider now a bounded plasma, and an incident electromagnetic wave coming from the external space, the behaviour of the plasma considered as a medium still be can studied with reference to the plasma frequency.

If $\omega \prec \omega_p$ the electrons react to the electric field and they can be considered as dipoles able to re-irradiate the incident wave and to totally reflect it without losses. The inner plasma electrons don't experience the presence of the electromagnetic wave because of the shielding behaviour of the outer electrons.

On the contrary, if $\omega_p \prec \omega$ the incident wave can pass through the plasma without any loss (here reflections due to eventually abrupt changes in the interface gas and plasma are not considered).

The plasma behaviour depicted above, can also be described in terms of electron density because of the direct relation between plasma frequency and electron density.

Indeed if we consider the situation $\omega_p = \omega$ which is the condition that separate the propagation and non-propagation regime, it is possible to calculate the so called critical electron density n_{ec}.

$$n_{ec} = \frac{\omega^2 m_e \varepsilon_0}{e^2} = \frac{4\pi^2 m_e \varepsilon_0}{e^2} v^2 \tag{1.1}$$

where v is the frequency of the incident electromagnetic wave, ε_0 the vacuum dielectric constant, e the electron charge and m_e the electron mass.

The condition $n = n_{ec}$ (or the equivalent $\omega_p = \omega$) divides thus two different regimes. If $n \prec n_{ec}$ ($\omega_p \prec \omega$) the so called *collective interaction regime* exists and the plasma acts as a dielectric through which the electromagnetic wave passes without losses.

If $n \succ n_{ec}$ ($\omega_p \succ \omega$) the *particle interaction regime* holds and the plasma totally reflects the incident wave.

From Figure 1.1 it is possible to relate the plasma electron density and the incident wave frequencies needed to reach collective interaction regime. The plasmas examined in this work are characterized by electron density in the order of 10^{16} - 10^{19} $[part / m^3]$ and the condition $\omega_p \prec \omega$ is reached for frequency in the microwave regime (1 - 100 $[GHz]$) .

Let's now express the relations between the electromagnetic wave behaviour inside a plasma and plasma frequency.

If we consider a collisionless plasma and a time-harmonic electric field $E(t) = E_0 e^{j\omega t}$ due to both the contribution of the external electric field, imposed by a source outside the plasma, and the internal electric field associated to the electron space charge displacement, it is possible to formulate the motion equation as

$$m_e \ddot{\xi} = -e \vec{E} \tag{1.2}$$

which has the solution

$$\xi = \frac{e}{m_e \omega^2} \vec{E} \tag{1.3}$$

The current density becomes:

$$\vec{J} = -n_e e \xi = -j \frac{n_e e^2}{m_e \omega} \vec{E} \tag{1.4}$$

As a consequence of the Ohm law, the electrical conductivity takes a new form:

$$\sigma = -j \frac{n_e e^2}{m_e \omega} \tag{1.5}$$

Expressing $\sigma + j\omega\varepsilon \rightarrow j\omega\breve{\varepsilon}$ we can rewrite the complex dielectric constant:

$$\breve{\varepsilon} \equiv (\varepsilon)_{\Re} - (j\varepsilon)_{\Im} = 1 - j\frac{\sigma}{\omega}$$

$$\Longrightarrow \qquad \breve{\varepsilon} = \varepsilon_0 (1 - j\frac{\breve{\sigma}}{\varepsilon_0 \omega}) = \varepsilon_0 (1 - \frac{n_e e^2}{m_e \varepsilon_0 \omega^2}) = \varepsilon_0 (1 - \frac{\omega_p^2}{\omega^2}) \tag{1.6}$$

where $\breve{\sigma}$ is the complex conductivity , and also the *complex relative permittivity*

$$\breve{\varepsilon}_r = \frac{\breve{\varepsilon}}{\varepsilon_0} = 1 - \frac{\omega_p^2}{\omega^2} \tag{1.7}$$

This analysis can be applied to a plane wave travelling in the direction aligned with the z axis and vary with $e^{j\omega t-\breve{\gamma} z}$, where $\breve{\gamma}$ is the *complex propagation coefficient:*

$$\breve{\gamma}=\alpha+j\beta \tag{1.8}$$

α and β are the *attenuation* and the *phase coefficient* respectively.

For $\omega<\omega_p$ the *effective dielectric constant* ε_r becomes negative and $\breve{\gamma}\in\Re$

$$\begin{aligned}&\alpha=(\frac{\omega_p^2}{\omega^2}-1)^{1/2}\ \frac{\omega}{c},\quad \text{if } \omega^2<<\omega_p^2 \quad\Rightarrow\quad \alpha=\frac{\omega_p}{c}\\&\beta=0\end{aligned} \tag{1.9}$$

For $\omega>\omega_p$ and $\breve{\gamma}\in\mathcal{C}$

$$\begin{aligned}&\alpha=0\\&\beta=(1-\frac{\omega_p^2}{\omega^2})^{1/2}\ \frac{\omega}{c},\quad \text{if } \omega^2>>\omega_p^2 \quad\Rightarrow\quad \beta=\frac{\omega}{c}\end{aligned} \tag{1.10}$$

where c is the vacuum *light velocity.*

Solving the wave equation and for ($\mu_r=1$), the following equation is derived:

$$\breve{\gamma}^2=-\breve{\varepsilon}_r\frac{\omega}{c} \tag{1.11}$$

This leads to the dispersion relation:

$$\breve{\gamma}=j\ \breve{\varepsilon}_r^{1/2}\frac{\omega}{c} \tag{1.12}$$

We can define the refractive index η:

$$\eta=\frac{c}{v_\phi} \tag{1.13}$$

Expressing $\beta=\frac{2\pi}{\lambda}=\frac{\omega}{v_\phi}$ we obtain:

$$\eta=\frac{\beta\, c}{\omega}=(1-\frac{\omega_p^2}{\omega^2})^{1/2} \tag{1.14}$$

where v_ϕ is the phase velocity in the medium

1.3 Electromagnetic waves in collisional plasmas

The warm plasmas studied in this work, can be well approximated with a Lorentzian plasma model that includes a viscous damping term in the motion equation. With this new term the equation (1.2) becomes:

$$m_e \ddot{\xi} = -eE - m_e \upsilon_{eH} \dot{\xi} \tag{1.15}$$

The new dumping term $m_e \upsilon_{eH} \dot{\xi}$ is related to the Coulombian interaction between electrons and heavy particles; it takes into account that, on the average, an electron loses direct momentum $m_e \dot{\xi}$ due to the collisions with heavy particles. The entity of this loss is measurable by means of the *electron-heavy collision frequency* (also called *collision frequency for momentum transfer*).

Being $E(t) = E_0 e^{j\omega t}$ the solution of the equation is given by:

$$\xi = \frac{e\ \vec{E}}{m_e \omega\ (\omega - j\upsilon_{eH})} \tag{1.16}$$

The $m_e \upsilon_{eH} \dot{\xi}$ component represents the Colombian interaction between electrons and heavy particles.

By applying the same procedure developed for ideal plasmas, it is possible to define the *complex conductivity* $\breve{\sigma}$ and the *complex relative permittivity* $\breve{\varepsilon}_r$:

$$\breve{\sigma} \equiv (\sigma)_{\Re} + (j\ \sigma)_{\Im} = \frac{n_e e_2}{m_e(\upsilon_{eH} + j\ \omega)} = \frac{n_e e_2}{m_e} \cdot \frac{\upsilon_{eH} - j\ \omega}{\upsilon_e^2 + \omega^2} \tag{1.17}$$

$$\begin{aligned} \breve{\varepsilon}_r &\equiv (\varepsilon_r)_{\Re} + (j\ \varepsilon_r)_{\Im} = 1 - j\ \frac{\breve{\sigma}}{\varepsilon_0 \omega} = 1 - \frac{\omega_p^2}{\omega(\omega - j\upsilon_{eH})} = \\ &= (1 - \frac{\omega_p^2}{\omega^2 + \upsilon_{eH}^2}) - j(\frac{\frac{\omega^2 \upsilon_{eH}^2}{\omega}}{\omega^2 + \upsilon_{eH}^2}) \end{aligned} \tag{1.18}$$

where υ_{eH} is the collision frequency for moment transfer

The subscripts $\Re$ and $\Im$ identify the *real* and the *imaginary parts* respectively.

The solution of the equation (1.15) is given by

$$\xi = \frac{e\ \vec{E}}{m_e \omega\ (\omega - j\upsilon_{eH})} \tag{1.19}$$

The dispersion relation (1.12), showed that the *complex propagation coefficient* $\breve{\gamma}$ can be expressed in term of *complex relative permittivity* $\breve{\varepsilon}_r$. In this way we introduce a *complex refractive index:*

$$\breve{\eta} \equiv \eta + j\,\mathcal{X} = -j\,\breve{\gamma}\,\frac{c}{\omega} = \breve{\varepsilon}_r^{\,1/2} \tag{1.20}$$

where the η and $\mathcal{X}$ are the *refractive index* and the *attenuation index*.

After this we can write:

$$\alpha = \mathcal{X}\,\frac{\omega}{c} \tag{1.21}$$

$$\beta = \eta\,\frac{\omega}{c} \tag{1.22}$$

Recalling the equation (1.7) it is possible to determine the refractive and the attenuation index as a function of plasma and the electromagnetic incident wave frequencies and the electron-heavy collision frequency:

$$\mu \equiv (\breve{\varepsilon}_r^{1/2})_{\Re} = \left\{ \frac{1}{2}\left(1 - \frac{\omega_p^2}{\omega^2 + \upsilon_{eH}^2}\right) + \frac{1}{2}\left[\left(1 - \frac{\omega_p^2}{\omega^2 + \upsilon_{eH}^2}\right)^2 + \left(\frac{\omega_p^2}{\omega^2 + \upsilon_{eH}^2}\,\frac{\upsilon_{eH}}{\omega}\right)^2\right] \right. \tag{1.25}$$

$$x \equiv (\breve{\varepsilon}_r^{1/2})_{-\Im} = \left\{ -\frac{1}{2}\left(1 - \frac{\omega_p^2}{\omega^2 + \upsilon_{eH}^2}\right) + \frac{1}{2}\left[\left(1 - \frac{\omega_p^2}{\omega^2 + \upsilon_{eH}^2}\right)^2 + \left(\frac{\omega_p^2}{\omega^2 + \upsilon_{eH}^2}\,\frac{\upsilon_{eH}}{\omega}\right)^2\right]^{1} \right. \tag{1.26}$$

Considering now the attenuation and the phase coefficients from the two previous expressions (1.25) and (1.26), the difference in behaviour between an ideal plasma and a real one is apparent. The electromagnetic waves incident in a real plasma have more smoothed variations in a transition regime with partial reflection and partial attenuation. In this case we don’t have an ideal transmission with total reflection and without attenuation.

Note that, when $\upsilon/\omega \geq 1$, the refractive index is bigger than one, and the phase velocity exceeds the light velocity.

The measurement of this two coefficients permits the determination of the plasma frequency, the electron density and the electron-heavy collision frequency.

The attenuation of an electromagnetic wave causes a finite penetrations depth, this depend on thickness of the plasma.

From the equations (1.41) and (1.12) it is useful to introduce the *attenuation length* δ. This coefficient represent the penetration depth into a material that is , in our case, into the plasma:

$$\delta = \frac{1}{\alpha} \tag{1.23}$$

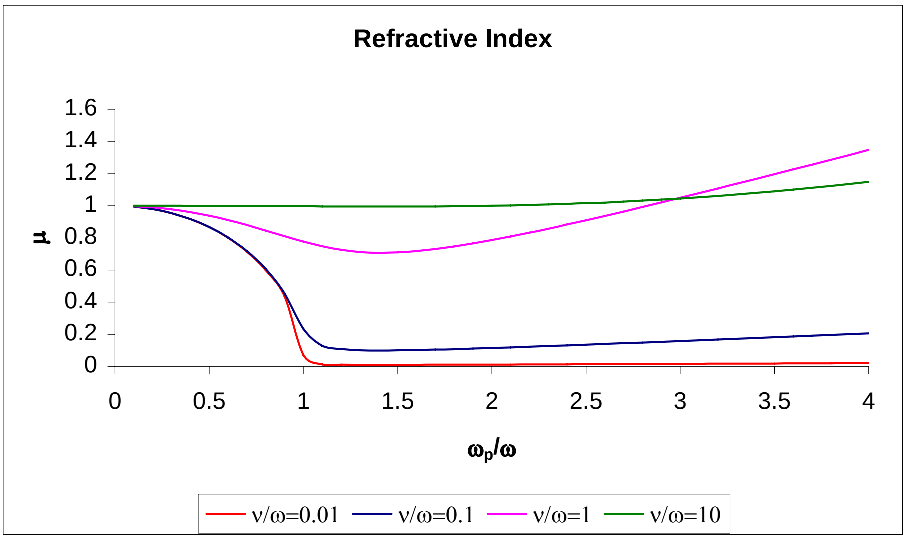

Figure 1.2 Refractive index for various collision frequencies

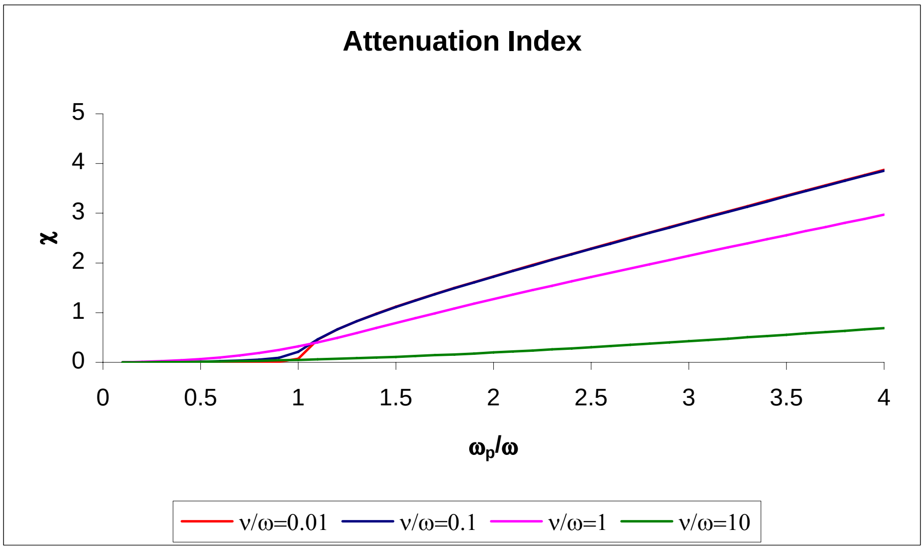

Figure 1.3 Attenuation index for various collision frequencies

In a conductive plasma, the complex propagation coefficient becomes:

$$\breve{\gamma} = -\sqrt{-j\omega\mu\upsilon} = \sqrt{\frac{\omega\mu\upsilon}{2}} + j\sqrt{\frac{\omega\mu\upsilon}{2}} \tag{1.24}$$

Then the attenuation length is then expressed as

$$\delta = \sqrt{\frac{2}{\omega\mu\sigma}} \tag{1.25}$$

This is the usual expression for the skin depth in metals. For example an electromagnetic wave of 12$[GHz]$ have a penetration depth equal to 2 $[\mu\ m]$.

In a partial transmittance regime, the transmission factor T_f of an electromagnetic wave a crossing a certain plasma volume can be defined as:

$$T_f = \frac{P_2}{P_1} = e^{(-\chi\frac{\omega}{c}\Delta x)} \tag{1.26}$$

where P_1 is the baseline transmitted power, i.e. the power transmitted without the plasma and P_2 is the transmitted power in present of plasma and Δx is the plasma dimension saw by the microwave.

The transmission factor is a function of plasma frequency and collisional frequency. In Figure 1.4 we have plot the transmission factors with fixed electron-heavy collision frequency and variable microwave frequency and in the Figure 1.5 the microwave frequency is fixed and the electron-heavy collision frequency is variable.

The plots show how the condition at which there is no wave propagation ($T_f = 0$) is only a function of the electron number density.

By means of a variable microwave frequency source, the frequency at which does not correspond any wave transmission can be found.

Under the assumption of $\omega >> \nu_{eH}$ (with $\upsilon_{eH} = const$) the critical electron number density corresponding to that frequency can be calculated as:

$$n_{ec} = \frac{\omega^2 m_e \varepsilon_0}{e^2} = \frac{4\pi^2 m_e \varepsilon_0}{e^2}\nu^2 = 1.2404\times10^{10} f^2\ [cm^{-3}] \tag{1.27}$$

where f is the microwave frequency

Then, the frequency can be lower down and allowing a partial transmission mode. From the known electron number density and the measured transmission factor, is then possible to calculate the electron collision frequency.

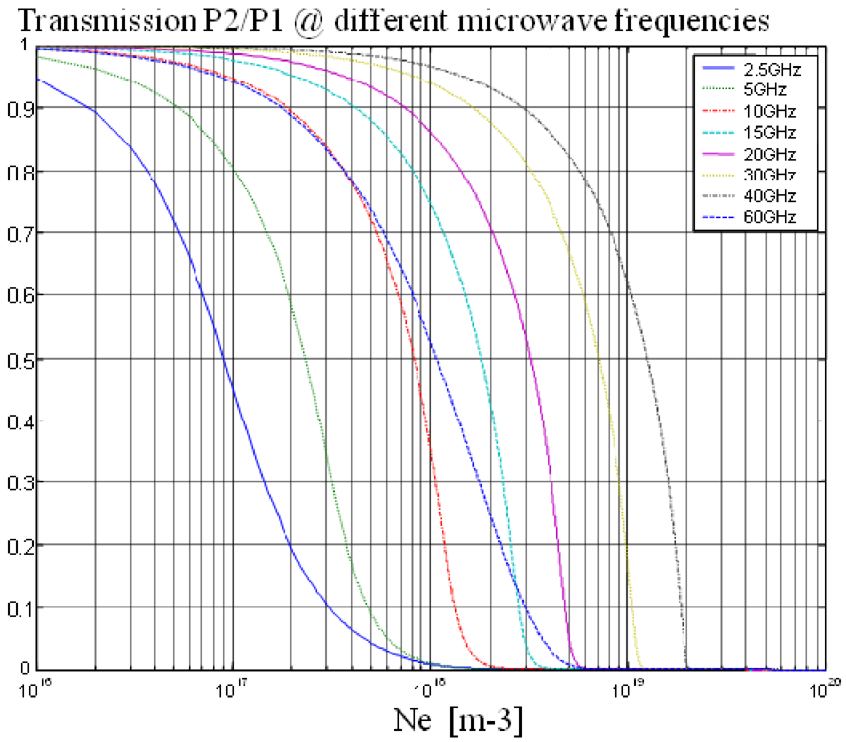

Figure 1.2 Transmission factor with an electron collisional frequency of 2[GHz] and variable microwave frequency

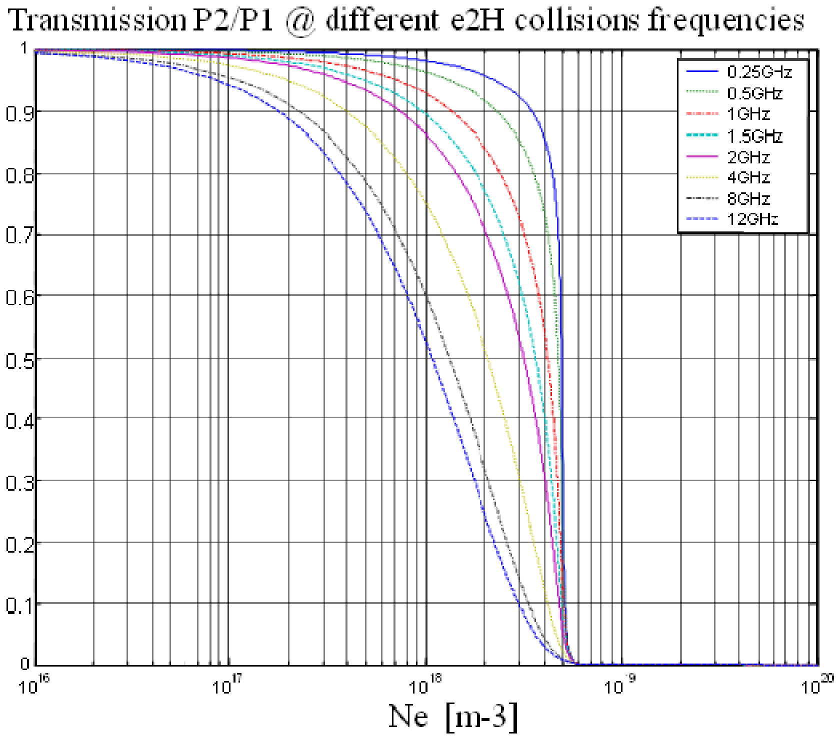

Figure 1.3 Transmission factor with a microwave frequency of 20[GHz] and variable electron-heavy collision frequency

1.4 Microwave propagation theory

Microwave plasma diagnostic techniques practice the measuring of the wave reflection from the wave transmission through or the wave absorption in a plasma or any other combination. Consequently, the goal of the measurement is to extract from the resulting some information about certain plasma properties.

In our case we consider the fluid refractive, dispersive, resonant, anisotropic, nonreciprocal, nonlinear and inhomogeneous, then we assume a Lorenz plasma propagation, which mean an uniform medium, without magnetic field acting on it.

If we consider a unvarying electron distribution function with *electron density* n_e, and an external one-dimensional perturbation in the x direction, a displacement $\xi(x)$ in the electron distribution along the x direction is realized.

The local electron density departs from the uniform density by an increment of:

$$\delta n_e = -n_e \frac{d\xi}{dx} \tag{1.28}$$

Assuming that the *electron density* is equal to the *ion density*: $n_e = n_i$ in the total plasma volume (net *charge density* ρ is zero), the actual perturbed charge density can be expressed as:

$$\delta\rho = -e\delta n_e = e\frac{d\xi}{dx}n_e \tag{1.29}$$

where $-e$ is the *electron charge*

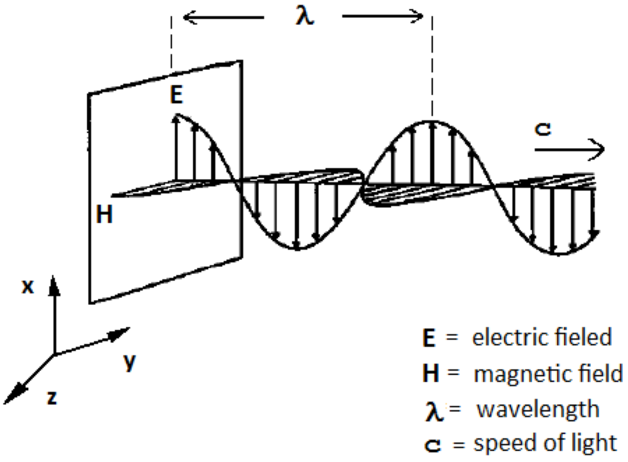

Figure 1.4 Microwave transmission

The charge displacement creates an electric field that must be take into account in the charge conservation by mean the Gauss' Law:

$$\frac{d\vec{E}}{dx} = e\frac{d\xi}{dx}n_e \Rightarrow \vec{E} = \frac{n_e e}{\varepsilon_0}\xi \tag{1.30}$$

The electric force for unit charge is:

$$\vec{F} = -e\vec{E} = -\frac{n_e e^2}{n_e e^2} \tag{1.31}$$

If we neglect the viscous damping forces generated by the collisions between electrons and heavy particles, that is, a collisionless plasma, the Newton equation of motion becomes:

$$m_e\ddot{\xi} + \frac{n_e e^2}{\varepsilon_0} = \vec{F}_{EXT} \tag{1.32}$$

where m_e is the electron mass, ε_0 the permittivity of vacuum, $\ddot{\xi} = \frac{\theta^2\xi}{\theta^2 t}$ the electron acceleration, $\vec{F}_{EXT}$ the external force required to cause the perturbation.

If the external force is removed, the electrons start to oscillate about their equilibrium positions with a simple harmonic motion, this calls plasma frequency:

$$\omega_p = \left(\frac{n_e e^2}{\varepsilon_0 m_e}\right)^{1/2} \tag{1.33}$$

This treatment is valid in the most general case, so an arbitrary spatial distribution of $\xi(x)$ can be considered. This assumption implies that a plasma oscillation does not transfer energy; a disturbance, therefore, does not propagate beyond the region in which it exists.

As all electromagnetic waves, microwaves can be described by *electric* and *magnetic fields*, $\vec{E}$ and $\vec{H}$, which are functions of space and time. The *electric* and *magnetic flux densities*, $\vec{D}$ and $\vec{B}$, in a linear and isotropic medium, at any point are related to the field intensities by:

$$\vec{D} = \varepsilon\ \vec{E} = \varepsilon_r\varepsilon_0\vec{E} \tag{1.34}$$

$$\vec{B} = \mu\ \vec{H} = \mu_r\mu_0\vec{H} \tag{1.35}$$

where ε_0 is the permittivity in vacuum, ε_r the dielectric constant, μ_0 the permeability in vacuum and μ_r the relative permeability of the medium.

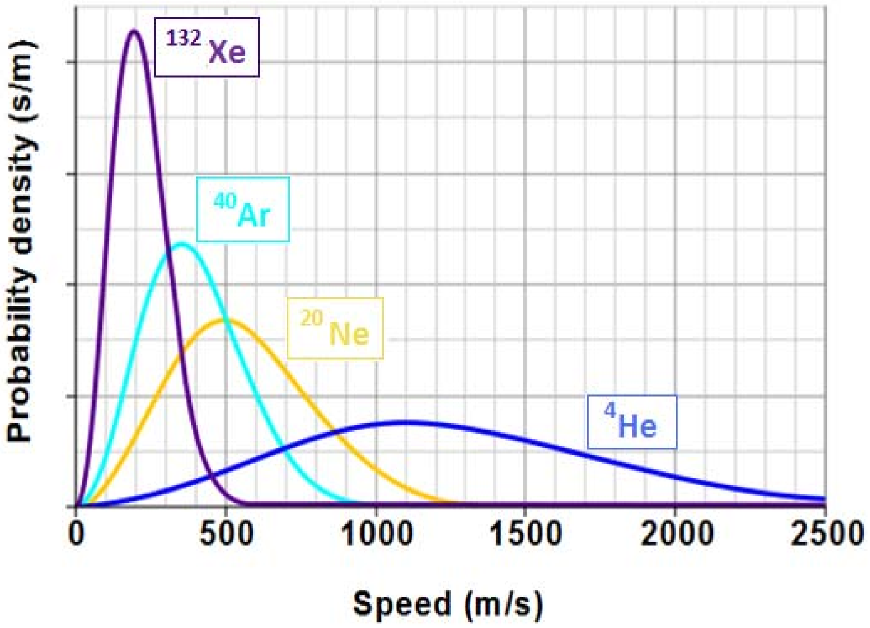

Figure 1.7 Maxwell molecular distribution for noble gases
Xenon 100 [K], Argon 200[K], Neon 400[K] and Helium 800[K]

Let' s introduce :

$$\varepsilon = \varepsilon_r \varepsilon_0 \qquad (1.36)$$
$$\mu = \mu_r \mu_0$$

These vectors are linked by the Maxwell's equations:

$$\nabla \bullet \vec{J} = -\frac{\partial \rho}{\partial t}$$
$$\nabla \times \vec{H} = \vec{J} + \frac{\partial \vec{D}}{\partial t} \qquad (1.37)$$
$$\nabla \times \vec{E} = -\frac{\partial \vec{B}}{\partial t}$$

The relation between $\vec{E}$ and $\vec{J}$ is expressed by means of the Ohm law:

$$\vec{J} = \sigma \ \vec{E} \qquad (1.38)$$

where $\vec{J}$ is the current density and σ the conductivity of the medium.

The electromagnetic proprieties of a medium can be thus specified by three independent constants ε_r , μ_r , σ .

We obtain a separate equation for each field under the assumption of $\xi(x)$ in the region of interest. For the electric field we have:

$$\nabla \times \nabla \times \vec{E} = -\frac{\partial(\nabla \times \vec{B})}{\partial t} = -\mu \frac{\partial(\nabla \times \vec{H})}{\partial t}$$
$$\nabla \times \nabla \times \vec{E} = \nabla(\nabla \bullet \vec{E}) - \nabla^2 \vec{E} = -\mu\ \varepsilon\ \frac{\partial^2 \vec{E}}{\partial^2 t} \tag{1.39}$$

Since $\rho = 0$ and $\varepsilon = const$ we finally obtain:

$$\nabla^2 \vec{E} - \mu\ \varepsilon\ \frac{\partial^2 \vec{E}}{\partial t^2} = 0 \quad \Rightarrow \quad \nabla^2 u = \frac{1\partial^2 u}{v^2 \partial^2 t} \tag{1.40}$$

where u is the solution of the equation, v the propagation velocity of the wave and $c = (\mu\ \varepsilon\ )^{1/2}$ the light velocity.

From the Maxwell's equations, by neglecting the electric field $\vec{E}$, we obtain the wave relation for the magnetic field $\vec{H}$:

$$\nabla^2 \vec{H} - \mu\ \varepsilon\ \frac{\partial^2 \vec{H}}{\partial t^2} = 0 \tag{1.41}$$

For an harmonic variation of the fields as $e^{j\,\omega\,t}$ and recalling that $k^2 = \omega^2 \mu\ \varepsilon$ the Helmholtz equations are obtained:

$$\nabla^2 \vec{E} - k^2 \vec{E} = 0 \tag{1.42}$$

$$\nabla^2 \vec{H} - k^2 \vec{H} = 0 \tag{1.43}$$

where $k = \omega\sqrt{\mu\ \varepsilon\ } = \frac{\omega}{v} = \frac{2\pi}{\lambda}$ is the wave number and $\lambda = \frac{v}{f}$ the wavelength.

In the free space the wave number is normally expressed as:

$$k_0 = \omega\sqrt{\mu_0 \varepsilon_0} = \frac{2\pi}{\lambda_0} \tag{1.44}$$

The general solution for the equations of Helmholtz can be found by separation of the variables. In our study only plane waves are considered.

For the electric field we can expressed each component as

$$\frac{\partial^2 \vec{E}_i}{\partial x^2}+\frac{\partial^2 \vec{E}_i}{\partial y^2}+\frac{\partial^2 \vec{E}_i}{\partial z^2}+k_0^2 \vec{E}_i=0 \quad i=x,y,z \tag{1.45}$$

Let start with the x component :

$$\vec{E}_x = f(x)g(y)h(z) \tag{1.46}$$

Substituting this expression in the equation (1.44) we find:

$$\frac{f''}{f}+\frac{g''}{g}+\frac{h''}{h}+k_0^2=0 \tag{1.47}$$

The separation of variables determine the following relations:

$$\begin{gathered}\frac{d^2 f}{dx^2}+k_x^2 f=0\\ \frac{d^2 g}{dy^2}+k_y^2 g=0\\ \frac{d^2 h}{dz^2}+k_z^2 h=0\end{gathered} \tag{1.48}$$

$$k_x^2+k_y^2+k_z^2=k_0^2 \tag{1.49}$$

The three equations (1.47) are simple harmonic differential equations with exponential solution of the form $e^{-jk_x x}, e^{-jk_y y}, e^{-jk_z z}$ One suitable solution for $\vec{E}_x$ may be chosen as:

$$\vec{E}_x = Ae^{-jk_x x-jk_y y-jk_z z} \tag{1.50}$$

where A is the amplitude

If we consider now the more general case of a medium with finite conductivity σ , the relation (1.38) holds and a certain amount of energy will be dissipated by Joule effect. For this case, the wave equation presents a dumping term due to the conductivity. IN this case the Maxwell's equations for $J \neq 0$ the following relation for the electric field is obtained:

$$\nabla^2 \vec{E} - \mu\,\sigma\,\frac{\partial \vec{E}}{\partial t} - \mu\,\sigma\,\frac{\partial^2 \vec{E}}{\partial t^2} = 0 \tag{1.51}$$

For the magnetic field $\vec{H}$ the following equation holds:

$$\nabla^2 \vec{H} - \mu\,\sigma\,\frac{\partial \vec{H}}{\partial t} - \mu\,\sigma\,\frac{\partial^2 \vec{H}}{\partial t^2} = 0 \tag{1.52}$$

In the case of time-harmonic fields varying as $e^{j\omega t}$, damping effects enter in the expression of $\vec{H}$:

$$\nabla \times \vec{H} = (\sigma + j\omega\varepsilon)\,\vec{E} \tag{1.53}$$

The equation (1.51) can be written as:

$$\nabla^2 \vec{E} + \omega^2 \mu_0 \varepsilon_0 (1 - j\frac{\sigma}{\omega\varepsilon_0}) = 0 \tag{1.54}$$

For metals, the conduction current $\tau \vec{E}$ is generally larger than the displacement current $\omega\varepsilon_0 \vec{E}$, therefore in the previous equation the latter term can be neglected leading to:

$$\nabla^2 \vec{E} - \mu\sigma\frac{\partial \vec{E}}{\partial t} = 0 \tag{1.55}$$

For the time-harmonic case we obtain:

$$\begin{gathered} \nabla^2 \vec{E} - j\omega\mu_0\sigma\ \vec{E} = 0 \\ \nabla^2 \vec{H} - j\omega\mu_0\sigma\ \vec{H} = 0 \end{gathered} \tag{1.56}$$

Lets now consider the propagation of time-harmonic electric and magnetic fields which are governed by the Helmholtz equations (1.41) and (1.42).

The type of solution we are looking for corresponds to a wave that propagates in a preferential direction, let’s say along z. Since the Helmholtz equation is separable, in our study, solutions in the form *f(z) g(x; y)*, where f is a function of *z* only and *g* is a function of *x* and *y* can be found.

The second derivative with respect to *z* enters into the wave equation in a manner similar to the second derivative with respect to time.

By analogy with $e^{j\omega t}$ time dependence, the *z* dependence can be assumed to be $e^{\pm j\beta z}$. This assumption will lead to wave solution in the form $\cos(\omega t + \beta z)$ and $\sin(\omega t \pm \beta z)$ which are appropriate to describing wave propagation alongthe *z* axis.

With an assumed *z* dependence $e^{-j\beta z}$ (i.e. a wave propagation in the positive *z* direction) the *"del"* operator can be decomposed as

$$\nabla = \nabla_t + \nabla_z = \nabla_t - j\beta\hat{a}_z \tag{1.57}$$

since $\nabla_z = \frac{\hat{a}_z\partial}{\partial z}$. Note that ∇_t is the transverse part and equals $\frac{\hat{a}_x\partial}{\partial x} + \frac{\hat{a}_y\partial}{\partial y}$ in rectangular coordinates.

With these considerations, the propagation constant β will depend on the waveguide configuration.

The decomposition of the fields into transverse and axial component and the separation of the *z* component, allow to simplify the Maxwell's equations. Electric and magnetic fields can be expressed as:

$$\vec{E} = (e_t + e_z)e^{j(\omega t - \beta z)} \tag{1.58}$$

$$\vec{H} = (h_t + h_z)e^{j(\omega t - \beta z)} \tag{1.59}$$

where the subscript term *t* refers to the transverse component, the subscript term z refers to the axial one. All the components depend only by the transverse coordinates x and y.

The Maxwell's equations become:

$$\nabla_t \times e_t = -j\omega\mu h_z \tag{1.60}$$

$$\nabla_t \times e_z - j\beta\hat{k} \times e_t = -\hat{k} \times \nabla_t e_z + -j\beta\hat{k} \times e_t = -j\omega\mu h_t \tag{1.61}$$

$$\nabla_t \times h_t = -j\omega\varepsilon e_z \tag{1.62}$$

$$-\hat{k} \times \nabla_t h_z + j\beta\hat{k} \times h_t = -j\omega\varepsilon e_t \tag{1.63}$$

$$\nabla_t \cdot h_t = +j\beta h_z \tag{1.64}$$

$$\nabla_t \cdot e_t = +j\beta h_z \tag{1.65}$$

where as introduced before ε and μ are the permittivity and the permeability of the considered medium.

For a large variety of waveguides of practical interest it turns out that all boundary conditions can be satisfied by fields that do not have all components present.

Because of the widespread occurrence of such field solutions, the following classification of solutions is of practical interest.

- *transverse electric*, referred to as *TE or H modes*, for which $e_z = 0, h_z \neq 0$
- *transverse magnetic*, referred to as *TM or E modes*, for which $h_z = 0, e_z \neq 0$
- *transverse electromagnetic*, or *TEM waves*, for which $e_z = h_z = 0$

The transverse electric TE mode case is considered at first. In this case, h_z plays the role of a potential function from which the rest of the field components may be obtained.
We recall now the Helmholtz equation for the magnetic field (1.42) and separating the above equation into transverse and axial parts and replacing ∇ with $\nabla_t^2 - \beta^2$ yield, come out the new equation:

$$\nabla_t^2 h + k_c^2 h \tag{1.66}$$

where $k_c^2 = k_0^2 - \beta^2$ (1) (2)

When this equation is solved, subjected to appropriate boundary conditions, the value k_c^2 will be found to be a function of the particular waveguide configuration.
Solutions for the equation (1.65) can be found by the separating variable method, obtaining

$$h_z = \left(A\cos(k_x x) + B\sin(k_x x)\right) * \left(C\cos(k_y y) + D\sin(k_y y)\right) \tag{1.67}$$

where A, B, C and D are arbitrary constant.

We consider now a waveguide, sketched in Figure 1.8, stretched out along the z direction.

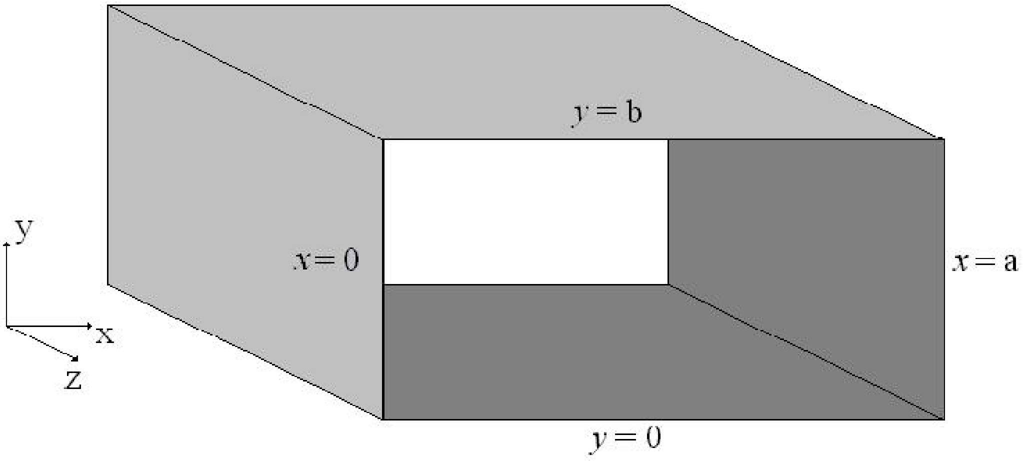

Figure1.8 Hollow rectangular waveguide

Setting e_t and e_z equal to zero at the boundaries, the magnetic boundary conditions can be found from equations (1.60) and (1.61):

$$\frac{\partial h_z}{\partial x} = 0 \quad \Rightarrow \quad x = 0, a \tag{1.68}$$

$$\frac{\partial h_z}{\partial y} = 0 \quad \Rightarrow \quad y = 0, b \tag{1.69}$$

Applying these conditions to equations (1.66) we obtain:

$$h_z = A_{mn} \cos\left(\frac{n\pi x}{a}\right)\cos\left(\frac{m\pi y}{b}\right) \tag{1.70}$$

only for integer values of *n* and *m*. The new coefficients for *x* and *y* are the eigenvalues of the propagation constants k_x and k_y. The remaining magnetic field components and the electric field components are found by the substitution of this result into equations (1.59) and (1.64). A solution with given values of *n* and *m* is referred to as a TE_{nm} mode.

Lets now consider the *TM modes*. The wave equation for the axial electric field is:

$$\nabla_t^2 e_z + k_c^2 e_z = 0 \tag{1.71}$$

The boundary condition for which the tangential component of the electric field must go to zero at the wall is imposed:

$$\begin{cases} e_z = 0 \\ x = 0, a \\ y = 0, b \end{cases} \tag{1.72}$$

which leads to a solution in the form

$$e_z = A_{nm} \sin\left(\frac{n\pi\ x}{a}\right)\sin\left(\frac{m\pi\ y}{b}\right) \tag{1.73}$$

The remaining electric field components and the magnetic field components are found from the equations (1.59) through (1.64) using this result for e_z.

Note that in the solutions for the TE and TM waves, each mode corresponds to a different eigenvalue, k_c determined by the relation

$$k_{c,nm}^2 = \left(\frac{n\pi}{a}\right)^2\left(\frac{m\pi}{b}\right)^2 \tag{1.74}$$

We recall now that the constant k_c is defined by $k_c^2 = k^2 - \beta^2$. By using the relation for k_c and the definition $k = \sqrt{\omega^2 \mu \varepsilon} = 2\dfrac{\pi}{\lambda}$ the propagation constant γ can be expressed as

$$\gamma \equiv j\beta = j\sqrt{k^2 k_c^2} = j\sqrt{\left(\frac{2\pi}{\lambda}\right)^2 - \left(\frac{n\pi}{a}\right)^2 - \left(\frac{m\pi}{b}\right)^2} \tag{1.75}$$

where λ is the wavelength of the wave. The propagation constant can be either real or imaginary, depending on the sign of the quantity $k^2 - k_c^2$. The cut-off wavelength λ_c, defined for γ equal to zero, is given by:

$$\lambda_c = \frac{2\pi}{\sqrt{\left(\frac{n\pi}{a}\right)^2 - \left(\frac{m\pi}{b}\right)^2}} = \frac{2ab}{\sqrt{n^2 b^2 + m^2 a^2}} \tag{1.76}$$

At wavelengths less than λ_c, γ is imaginary and microwaves propagate with a sinusoidal variation in the *z* direction of $e^{-\gamma z}$. However, at wavelengths greater than λ_c, γ is real and the factor $e^{-\gamma z}$ corresponds to an exponentially decaying wave. This is what is meant by cut-off.

Because the propagation constants are different for each mode, some modes may be propagating while others are not. A standard rectangular waveguide typically has one dimension twice the length of the other, *a = 2b*. For this type of waveguide, the cut-off wavelengths for the first three modes are listed in table 1.1.

nm	λ_c
10	2a
01	a
11	2a/$\sqrt{5}$

Table 1.1 Cut-off wavelengths for cavity modes

Comparing equations (1.69) and (1.72) for TE and TM modes, it can be seen that the lowest order TM mode is the TM11, since the trivial solution is obtained by setting n and m to zero. However, nontrivial TE modes exist for either n or m equal to zero. Between wavelengths of a and 2a only the TE10 mode propagates and all other modes are cut off. For this reason, the TE10 mode is known as the dominant mode, and it is in this single mode condition that microwave waveguides are typically operated.

The TE10 mode is sketched in Figures (1.7), (1.8) and (1.9), showing the electric and magnetic field lines. Physically, the mode number for TE modes corresponds to the number of half wave oscillations of the electric field in the perpendicular and parallel directions, respectively. So for a TE10 mode, the electric field has a one half period sinusoidal oscillation perpendicular to the polarization vector, and is constant in the parallel direction.

A brief discussion of the third class of propagating wave solutions, the transverse electromagnetic wave TEM, is in order. Following the form of equations (1.59) through (1.64)and setting the axial components of the electric and magnetic fields equal to zero, the Maxwell's equations may be written as:

$$\nabla_t \times e_t = 0 \tag{1.77}$$

$$\beta \, \hat{k} \times e_t = \omega\mu h_t \tag{1.78}$$

$$\nabla_t \times h_t = 0 \tag{1.79}$$

$$\beta \, \hat{k} \times h_t = \omega\varepsilon e_t \tag{1.80}$$

$$\nabla_t \cdot h_t = 0_z \tag{1.81}$$

$$\nabla_t \cdot e_t = 0 \tag{1.82}$$

Equation (1.76) shows that e_t must be the gradient of a scalar potential function. In order to satisfy also the equation (1.81), the scalar function must be a solution to the Laplace's equation:

$$\nabla_t^2 \Phi = 0$$

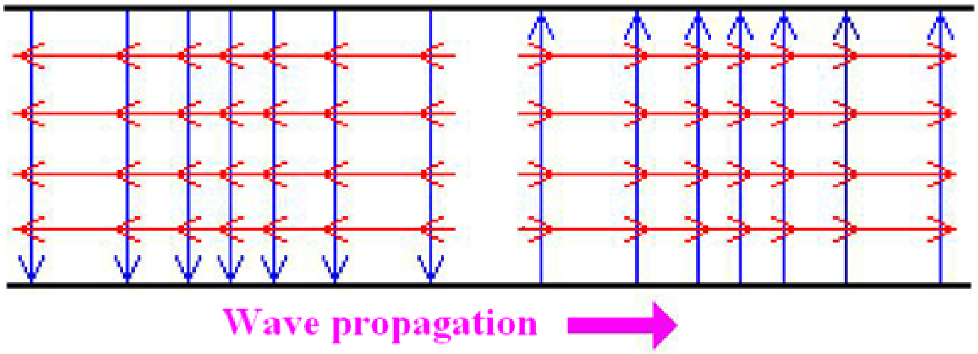

Figure 1.9 Electric and magnetic field lines for a TE10 mode

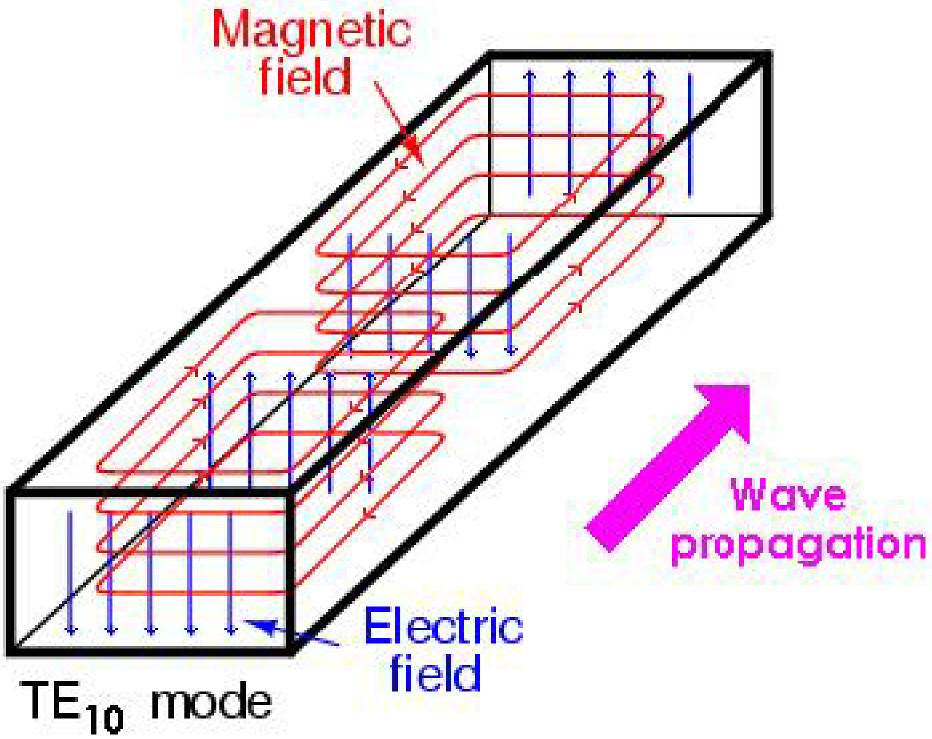

Figure1.10 Electric and magnetic field lines for a *TE10* mode

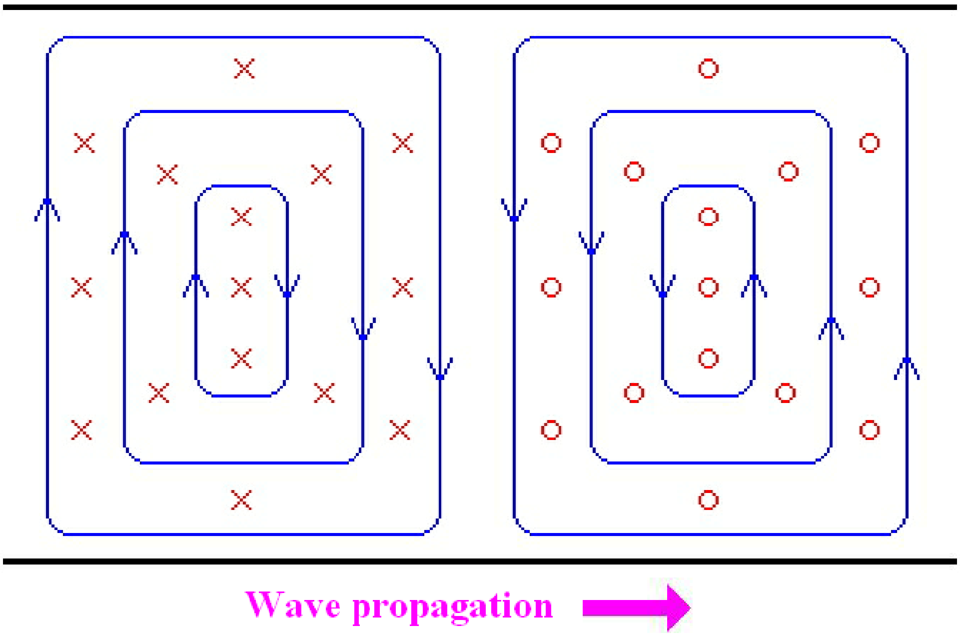

Figure 1.11 H-plane electric and magnetic field lines for the TE10 mode (top view)

The boundary condition for e_t implies that the gradient of Φ in the tangential direction must be zero along the boundary. The unique solution to Laplace's equation is then Φ equal to a constant. Physically, this states that the voltage is uniform along the boundary, which clearly must be true for the infinitely conductive walls assumed in the problem. In this case $E = -\nabla\Phi = 0$ everywhere inside the perimeter of the waveguide, and the only solution is the trivial one. Therefore, TEM modes cannot be sustained by hollow conducting waveguides.

In a rectangular waveguide the propagation constant, for a TE or TM mode, may be determined from equation (1.74), and it is seen to depend upon the waveguide dimensions. A guide wavelength may be defined as

$$\lambda_g = \frac{2\pi}{\beta} = \frac{2\pi}{\sqrt{\left(\frac{2\pi}{\lambda}\right)^2 - \left(\frac{n\pi}{a}\right)^2 - \left(\frac{m\pi}{b}\right)^2}} \tag{1.83}$$

In this case of a single propagating *TE₁₀* mode, this expression becomes

$$\lambda_g = \frac{2\pi}{\beta} = \frac{2\pi}{\sqrt{\left(\frac{2\pi}{\lambda}\right)^2 - \left(\frac{\pi}{a}\right)^2}} \tag{1.84}$$

and depends only on the larger dimension, a of the rectangular guide.

The guide wavelength is always greater than the free space wavelength, Φ. It may vary between λ as $a \to \infty$ and infinity at $a \to \lambda/2$. A guide which has a varying cross section along its length will allow propagation with a similarly varying guide wavelength. If the guide should become smaller than the cut-off dimension, corresponding to $a < \lambda/2$, then the wave will cease to propagate and instead will decay exponentially as an evanescent wave over a characteristic length scale $1/\gamma$, where

$$\gamma = \sqrt{\frac{2\pi}{\left(\frac{\pi}{a}\right)^2 - \left(\frac{2\pi}{\lambda}\right)^2}} \tag{1.85}$$

CHAPTER 2

SPECTROSCOPIC DIAGNOSTIC

2.1 Thermodynamic equilibrium

A plasma is a fluid in which electrons, ions, and neutral particles coexist. The description of a plasma that lies in Thermodynamic Equilibrium (*TE*) is rather simple: its state is fully described by relative few quantities, such as mass density, temperature and chemical composition. Everything is ruled by statistics.

At a given temperature the velocity distribution is described by the Maxwell equation, the populations of the excited states distribution is given by the Boltzmann equation, the density relation between ions and the electrons is given by the Saha equation and the radiation intensity by the Plank law. In *TE* all these phenomena are governed by the same temperature.

Different deviations from the thermodynamic equilibrium can be described in different approximated ways.

When radiations leave the plasma, the Plank relation is no more valid. Atoms, ions and electrons are still in equilibrium among them. This regime is known as *Local Thermodynamic Equilibrium* (*LTE*).

In *LTE* conditions, the populations of the excited states for each species are distributed according to the Boltzmann factor. The temperature defined by the ratio of the populations is called *excitation temperature* T_{EXT}. Departure from *TE* and radiation escape can result in departure from the equilibrium distribution within the excited states of the same species.

A further departure from *LTE* occurs when different particles are subjected to different forces. Usually the electrons are accelerated by the electromagnetic field and transfer the acquired energy to the other species. Since the rate of energy transfer from electrons *e* to heavy particles *H* is not efficient due the large difference in mass $m_H \geq 1836\ m_e$, the Maxwellization of the same species is much faster than one belonging to different groups. In this situation, the electrons and heavy particles are lightly coupled and their distribution functions can be referred to two different temperatures.

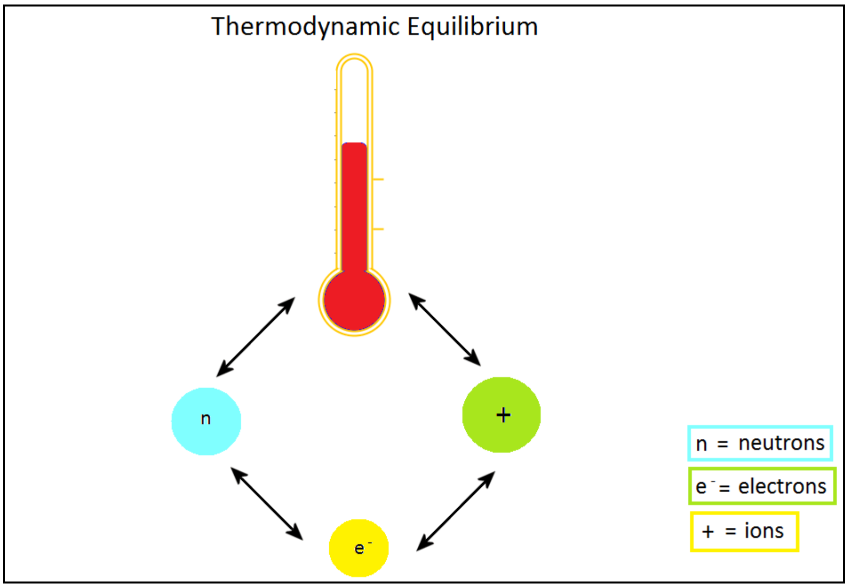

Figure 2.1 Thermodynamic equilibrium

This is called *Partial Local Thermodynamic Equilibrium PLTE*. Boltzmann and Saha equations still hold, but different Maxwellian distributions hold for the electrons at the electron temperature T_e and for the heavy particles at a temperature T_H.

2.2 Atomic and Molecular Emission Spectroscopy

The determination of the thermodynamic equilibrium properties of a plasma can be evaluated by means of emission spectroscopy. The radiation source generated by an atom can be associated to three phenomena:

→ bound-bound radiation related to the de-excitation of a bound electron,
→ free-bound radiation related to electron recombination processes,
→ free-free radiation related to the change of kinetic energy of an electron colliding against another charged particle or due to the centripetal acceleration due to the presence of a magnetic field.

In the bound-bound spontaneous emission an electron in an upper energy level falls to a level characterized by a lower energy. As a result a photon with energy $h\nu$ is emitted:

$$A^{(u)} \rightarrow A^{(l)} + h\upsilon \qquad (0.1)$$

where A is the atom in an upper (u) and lower (l) energy state, h is the Plank constant and υ the frequency of the emitted photon.

In the bound-bound stimulated emission an excited atom must interact with a photon characterized by an energy $h\upsilon$ equal to the energy gap of an allowed transition. After the de-excitation two photons with energy $h\upsilon$ are emitted.

$$A^{(u)} + h\upsilon_{lu} \rightarrow A^{(l)} + 2h\upsilon_{lu} \tag{0.2}$$

As the energy distribution of the electron levels is discrete, the frequency ν of the emitted photon can assume only a discrete series of values. Therefore bound-bound radiation is characterized by a discrete distribution of energy with a spectrum made of lines corresponding only to the allowed transitions.

The free-bound radiation is generated by the recombination of electrons with positive ion. The free electron falls into an energy level of the recombined particle becoming thereafter a bond electron. The energy corresponding to this transition is emitted in the form of a photon.

$$A^{+} + e(\varepsilon_e) \rightarrow A^{(l)} + h\upsilon \tag{0.3}$$

And the photon energy is:

$$h\upsilon = \frac{1}{2} m_e v_e^2 + \varepsilon_{il} \tag{0.4}$$

where the first term in the right hand side of the equation represents the kinetic energy owned by the colliding electron and the second term is the energy gap between the ionization level i (i.e. the maximum energy held by a bound electron) and the level l to which the electron falls.

As the kinetic energy of the free electron can assume a continuous distribution of values, the total energy $h\nu$ and thus the frequency ν of the emitted radiation can assume a continuous range of values. The free-free radiation is due to the deceleration of free electrons by means of the electric field of another charged particle or to the centripetal acceleration due to the presence of a magnetic field. In the first case we are dealing with a bremsstrahlung radiation in the second one with a cyclotron radiation. As the change regards the kinetic energy of free electrons, in free-free processes the energy spectrum of this radiation is continuous.

Usually the whole spectrum emitted by a plasma is composed by the contribution of discrete and continuous radiations. The radiation theory exposed above is valid both for atoms and molecules. However for molecules the bound-bound radiation depends on the internal structure of the emitting molecule. The radiation processes of diatomic molecules as the Nitrogen is considered as it is used in this work for diagnostics on plasmas in air.

When an atom is excited, it changes its electronic arrangement with a different distribution of the bound electrons in the atomic energy levels. Because of its internal structure, a molecule owns more degrees of freedom. Excited by collisions, a molecule can also rotate about the molecule axis, or the atoms of the molecule can vibrate around their equilibrium position. The amount of thermal energy associated to each degree of freedom (translations, rotations, and vibrations) is 1/2 kT.

For a Nitrogen gas below 80° K only translational level can be excited. Rising at ambient temperature, rotational excitations can occur. There are three rotational degrees of freedom, corresponding to the rotations around each of the coordinate axis. However just two degrees of freedom will contribute to the rotational energy. This is because the moment of inertia about the axis containing the two nuclei is negligible due to the extremely small radii of the atomic nuclei, compared to the distance between them in a molecule. By means of quantum mechanics theory it can be shown that the interval between successive rotational energy states is inversely proportional to the moment of inertia. As the moment of inertia corresponding to the rotation about the axis between the two nuclei is very small when compared to the other two rotational axes, the energy spacing can be considered so high that no excitations of the rotational state can occur unless the temperature is extremely high. Therefore the total thermal energy, which includes translation (with three degrees of freedom) and rotation (with only two degrees of freedom), is given by

$$\frac{3}{2}\mathrm{kT}+\frac{2}{2}\mathrm{kT}=\frac{5}{2}\mathrm{kT} \tag{0.5}$$

If the temperature is again increased, also the vibrational states are excited. Considering that the total degrees of freedom of a diatomic molecule in a tridimensional space are six, and by now three translational and two rotational degrees have been considered, linear molecules present only one vibrational degree of freedom. Each vibration mode develops both potential and kinetic energy, so the total vibrational energy can be expressed as

$$\frac{1}{2}+\frac{1}{2}kT=kT \tag{0.6}$$

The total internal energy of a linear molecule with all the modes excited is thus 7/2 kT.

De-excitation of excited rotational and vibrational levels of Nitrogen results in emission of radiation.

For the rotation modes the quantum mechanics theory leads to a rotation energy expressed by

$$E_{rot}=\frac{J(J+1)h^2}{8\pi^2 I} \tag{0.7}$$

where J is the rotational quantum number $J = (0,1,..n)$, I is the moment of inertia of the molecule and *h* is the Plank constant.

The radiation frequencies of allowed transitions are:

$$\upsilon_{J+1,\ J} = \frac{E_{J+1} - E_J}{h} = \frac{(J+1)h}{4\pi^2 I} \tag{0.8}$$

Selection rules allows only variation in the rotation quantum number of $\Delta J = \pm 1$. The rotation spectrum consists of series of even-spaced spectral lines.

The rotational levels are pretty close one to the other and rotational modes are therefore the most easily excitable in nature. For an H_2 molecule, rotational modes are excited starting from a number of collisions with other molecules in the order of 350. For heavier molecules this number quickly decreases. The collisional transport processes related with translational temperature are connected to similar dynamics. Rotational and translational relaxation times are so analogous and we can affirm that rotational and translational temperatures are equal:

$$T_{rotational} = T_{translational} \tag{0.9}$$

The low energy levels associated to rotational excitation generate electromagnetic emission that normally lay in the microwave region.

Vibrational modes are related to higher energies. Assuming the approximation of the simple harmonic oscillator, the vibrational energy can be expressed as

$$E_{vib} = \left(\mu + \frac{1}{2}\right)\hbar\omega = \left(\mu + \frac{1}{2}\right)\hbar\left(\frac{k}{m_{eff}}\right)^{1/2} \tag{0.10}$$

where μ is the vibrational quantum number $(\mu = 0,1,..n)$ and ω is the oscillation angular frequency related to the force constant of the bond, k, and the effective mass of the molecule m_{eff}. We refer to associated transition frequency as ν^{vib}.

The total energy associated to a ro-vibrational transition is thus

$$E_{tot} = E_{rot} + E_{vib} = \left(\frac{J(J+1)h^2}{8\pi^2 I}\right) + \left(\mu + \frac{1}{2}\right)\ \hbar\omega \tag{2.11}$$

The corresponding transition frequency ν depends both from the rotational and vibrational quantum numbers.

An example scheme of the allowed roto-vibrational transitions for the two allowed vibrational states (μ = 0, 1) and six possible rotational states $(J = 1,2,3,4,5)$ is reported in Figure 2.2 .

Transitions between vibrational levels may or not involve rotational transitions. If the rotational quantum number decreases $\Delta J = -1$ the so called *"P-branch"* transitions (or negative branch transitions) are formed.

If the rotational quantum number increases $\Delta J = +1$ the *"R-branch"* transitions (or positive branch transitions) are generated. Finally the *"Q-branch"* transitions are formed if the rotational quantum number remains unchanged $\Delta J == 0$. From the selection rules formulation derives that the Q-branch is not always allowed. For Nitrogen molecules is not.

The name *"branch"* derives from the series of close spectral lines that vibro-rotational transitions generate (see Figure 2.3).

The quantum mechanics theory provides us a simple formulation for the branches transition frequencies.

The ones for the P-branch are

$$\nu_P^{vib}(J) = \nu^{vib} - 2BJ \tag{0.11}$$

where B is the rotational constant equal to

$$B = \frac{h}{8\pi^2 cI} \tag{0.12}$$

and c is the light velocity.

In obtaining equation (2.12) it has been assumed that the inertial constant of the excited vibrational state B_v differs slightly from the ground vibrational state constant B.

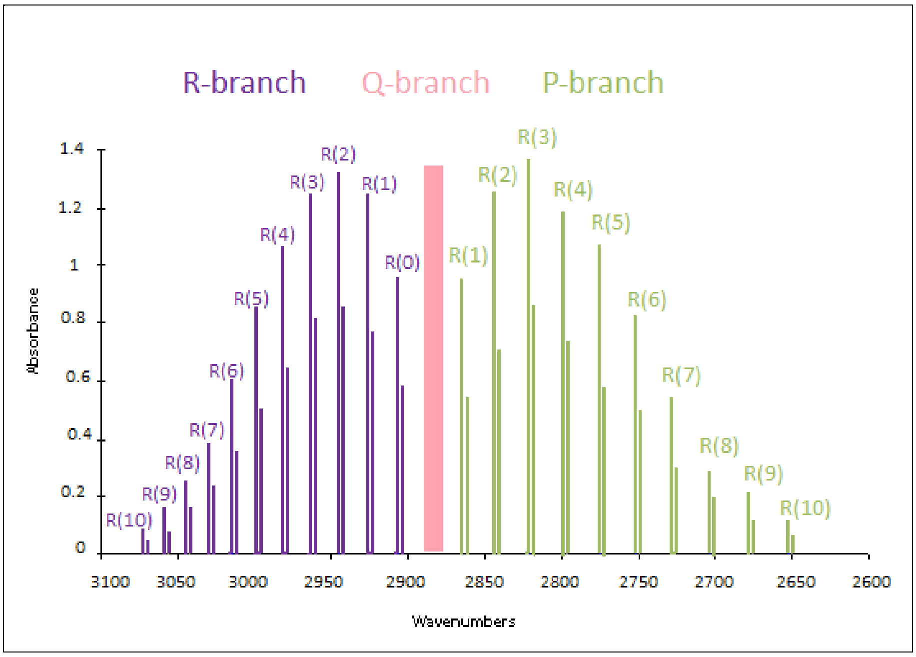

Figure 3.2 : Scheme of the spectra of R, Q and P molecular branches.

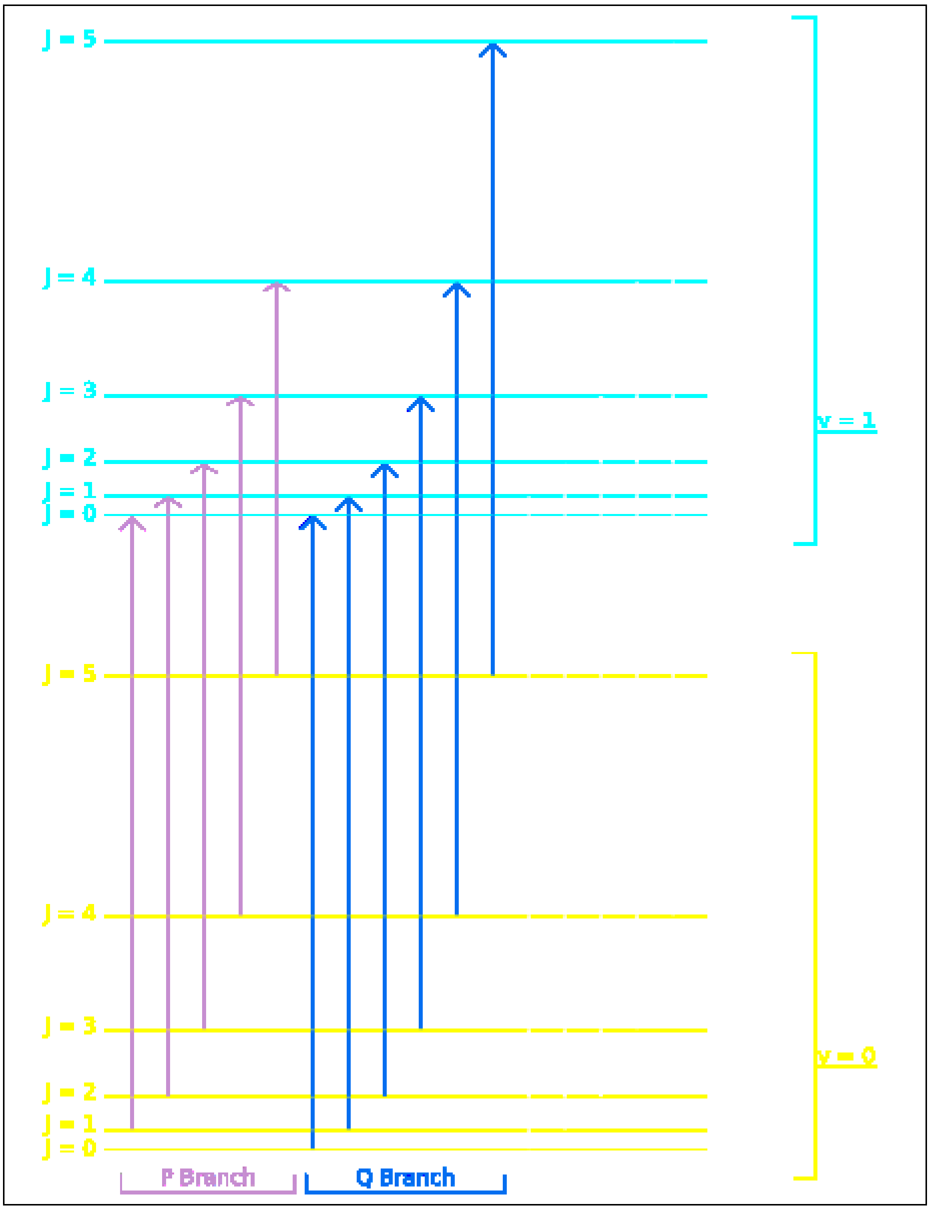

Figure 4.3 Scheme of the vibration-rotation energy levels for vibrational quantum number: 0-1 and rotational quantum number:0-5

For the Q-branch the transition frequencies are

$$\nu_Q^{vib}(J) = \nu^{vib} \tag{2.14}$$

In the case of the R-branch we obtain

$$\nu_R^{vib}(J) = \nu^{vib} + 2B\ (J+1) \tag{0.13}$$

From equations (2.12), (2.14) and (2.15) is possible to note that holds the relation

$$\nu_P(J) < \nu_Q(J) < \nu_R(J) \tag{0.14}$$

Vibro-rotational spectra generate lays in the far-infrared and in the Infrared regions. If we consider now electronic excitation connected to higher energy states, the treatment developed till now must be reviewed. The assumption of an inertial constant B that is equal for all the excited energy levels is no more valid because changes in the electronic arrangement determines variations in the moment of inertia of the molecule. We can introduce a new inertial constant B' proper of the excited state.

The rotational energy levels of the initial (J) and final (J') states are respectively

$$\begin{cases} E(J) = hcBJ(J+1) \\ \\ E(J') = hcBJ'(J'+1) \end{cases} \tag{0.15}$$

Recalling equations (2.12), (2.14), (2.15), the wavenumber $\hat{\nu}_i^{vib} = c\nu_i^{vib} \quad i = P, Q, R$ relative to a vibrational transition for the three branches cases is:

$\rightarrow$ P-branch $(\Delta j = -1) \rightarrow$ $\nu_P^{vib}(J) = \nu^{vib} - (B'+B)J + (B'-B)J^2$
$\rightarrow$ Q-branch $(\Delta j = 0) \rightarrow$ $\nu_Q^{vib}(J) = \nu^{vib} + (B'-B)J(J+1)$
$\rightarrow$ R-branch $(\Delta j = +1) \rightarrow$ $\nu_R^{vib}(J) = \nu^{vib} + (B'+B)(J+1) + (B'-B)(J+1)^2$

We recall that ν^{vib} refers to pure vibrational transitions.

First considering $B' < B$ and $(B'-B) < 0$ the bond length in the electronically excited state is greater than the one in the ground state. In this case the lines of the R-branch converge with increasing J .When $|B'-B|\,(J+1) > B'+B$, the lines start to appear at decreasing wavenumber. That is the R branch develops a so called *"band head peak"*.

When the opposite happens : $B' > B$ and $(B'-B) \geq 0$ is the case of P-branch lines wich converge into a band head peak as soon as $|\,B'-B\,|\,J > B'+B$.

Ro-vibrational spectra normally lay in the visible and ultraviolet regions. The already described atomic and molecular quantum mechanics theory, demonstrates how a hierarchy in the temperatures associated to different modes exists. We can assert that in a plasma this relation generally holds:

$$T_{EXT} \approx T_e \geq T_{vib} \geq T_{rot} \approx T_{traslation.} \tag{0.16}$$

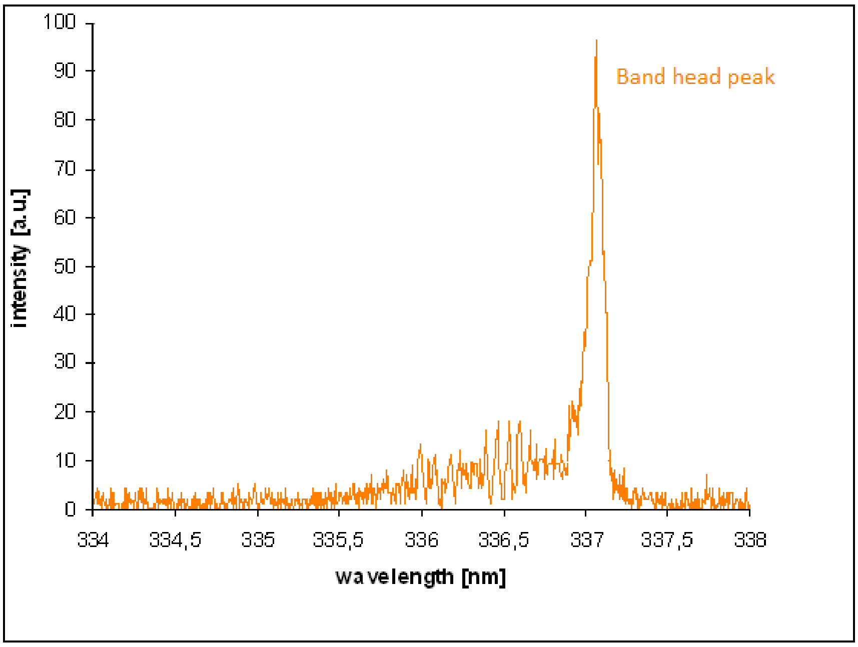

Figure 2.4 : An example of partially resolved vibrational R-branch spectra of the Second Positive System of the N_2 molecule

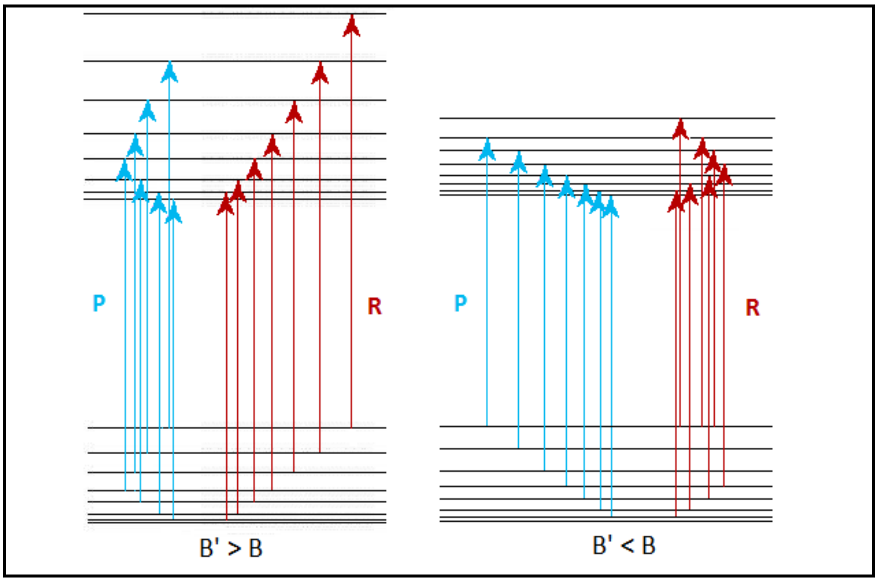

Figure 5.5 : Scheme of the spectra of R, Q and P molecular branches.

2.3 Evaluation of plasma parameters

The two principal parameters that feature a plasma are the electron temperature and the electron number density, and can be evaluated by means of the emission spectroscopy. Moreover this methodology is very useful because it is a completely non intrusive diagnostic. Hereafter the techniques used for the determination of these parameters in the plasmas subject of this work are presented.

2.3.1 Temperature evaluation

One of the most important and useful parameters of the plasma is the temperature (electron, vibrational or rotational temperature). For the evaluation is used a plot based on intensity measurements of the emitted spectra, called Boltzmann Plot.

The radiation intensity of a generic emission line I_u, is proportional to the spontaneous emission probability $A^{u\to l}$ and to the population density of the upper level of the transition n_u:

$$I_u = C_1 A^{u\to l} n_u \frac{h\,c}{\lambda_u} \tag{0.17}$$

where C_1 is a constant depending on the considered atom, h is the Plank constant, c is the vacuum speed of light and λ_u is the wavelength of the emitted photon.

If excited electrons are distributed over the energy levels with Boltzmann distribution, the following relation holds:

$$\frac{n_u}{n_0} = \frac{g_u}{g_0} e^{-\frac{E_u - E_0}{kT_e}} \tag{0.18}$$

where n is the electron density, g is the statistical weight and E is the energy level respectively for the ground state (subscript 0) and for the upper one (subscript u). At last, T_e is the electron temperature and k the Boltzmann constant.

Obtaining the excited population density n_u from equation (2.20) and putting it into the (2.19) it is possible to derive the following expression:

$$y_u = \ln\left(\frac{I_u \lambda_u}{A^{u\to l} g_u}\right) = C - \frac{E_u}{kT_e} \tag{0.19}$$

Each equation (2.21) represents a point (E_n, y_n) in a semi-logarithm plot, the so called *Boltzmann Plot*. The constant C takes into account all the constant quantities when element and ionization stage are chosen. In this way, the slope of the line fitting the data points, obtained by several emission lines of the same element and same ionization stage, is proportional to the inverse of the electron temperature.

If the points are perfectly aligned, the plasma is in partially local thermodynamic equilibrium (*pLTE*). Deviations from this equilibrium condition are represented in the Boltzmann plot by a scattering of the points.

In atomic plasma, like the Argon one used in the MHD experiments presented in this work, the Boltzmann plot allows the determination of the electron temperature by means of the lines intensity.

In air plasma, the vibro-rotational band head peaks are useful for the vibrational temperature evaluation.

The partially resolved rotational peaks are not available because of the limited resolution of the spectroscopic system used. The rotational temperature will be thus esteemed by means of an approximated method based on the partially resolved rotational spectra [29].

Also continuum emission intensity is related to the electron temperature and a Boltzmann plot can be realized in this case too (see Griem [1]).

As mentioned above, continuum emission is generated by the recombination emission and by bremsstrahlung.

Defining Z as the positive ion charge, the recombination-emission is generated when a free electron and an ion recombine to a neutral atom or an ion with charge $Z\text{-}1$. For the Argon plasma in which continuum emission has been used, only singly ionized species will be present so that $Z=1$. The *free-bound* (fb) emission coefficient $\varepsilon_{fb,\lambda}$ of this recombination emission is equal to

$$\varepsilon_{fb,\lambda} = \frac{c_1 n_e n_i}{\lambda^2 \sqrt{T_e}} \left[1 - e^{\left(-\frac{hc}{\lambda k T_e} \right)} \right] \xi_{fb}(\lambda, T_e) \qquad (0.20)$$

where $\xi_{fb}(\lambda, T_e)$ is the free-bound Bibermann factor which is a dimensionless quantity close to unity. For an Argon plasma is equal to one and the spectral emission lies in the range $\lambda > 300[nm]$. In this equation n_i is the total density of ions.

This number can be replaced by the electron number density n_e under the assumption that all ions are singly ionized and thus the plasma is quasi neutral. This assumption is also made for the rest of this study.

The constant c_1 is equal to:

$$c_1 = \frac{16\pi e^2}{3c^2 m_e \sqrt{6\pi n_e k(4\pi\varepsilon_0)}} \quad [Jm^4 k^{1/2} s^{-1} sr^{-1}] \tag{0.21}$$

Bremsstrahlung originates from a change of the momentum of electrons caused by an interaction of electrons *(e)* with neutral atoms *(a)* or ions *(i)*. We first consider the *e-i* interaction. The process of bremsstrahlung by the interaction of electrons with ions is represented by

$$e^- + A^+ \rightarrow e^- + A^+ + h\upsilon \tag{0.22}$$

During this Coulomb interaction, the energy of the electron is reduced and is transferred to the photon. The emission coefficient for the Coulomb interaction is represented by

$$\varepsilon_{fb,\lambda}^{ei}(\lambda, T_e) = \frac{c_1 n_e^2}{\lambda^2 \sqrt{T_e}} e^{\left(-\frac{hc}{\lambda k T_e}\right)} \xi_{fb}(\lambda, T_e) \tag{0.23}$$

In his equation $\xi_{fb}(\lambda, T_e)$ is the free-free Bibermann factor, and the value of c_1 is equal to that of the free bound Bibermann factor.

The other component of the bremsstrahlung radiation is generated by the interaction of electrons and atoms and is represented by

$$e^- + A \rightarrow e^- + A + h\upsilon \tag{0.24}$$

The emission coefficient of the electron-atom (*ea*) interaction is given by

$$\varepsilon_{fb,\lambda}^{ea}(\lambda, T_e) = \frac{c_2 n_e T_e^{3/2} n_a Q(T_{e)}}{\lambda^2} \left[1 + \left(1 + \frac{hc}{\lambda k T_e}\right)\right]^{\left(-\frac{hc}{\lambda k T_e}\right)} \tag{0.25}$$

The parameter Q in equation (2.27) represents the cross section of momentum transfer from electrons to neutral atoms.

For Argon, it can be approximated by

$$Q(\widehat{T}_e) = \sqrt{\frac{40}{3\pi(1 + 19.73\widehat{T}_e)^2} - 0.3 + 3.25\ \widehat{T}_e^3} \cdot 10^{-20} \quad [m^{-2}] \tag{0.26}$$

where the electron temperature $\widehat{T}_e$ is given in $[eV]$. Equation (2.28) only holds under the assumption that an integration of Q over the electron velocity can be replaced by taking the value of Q at the average electron velocity.

The coefficient c_2 is given by

$$c_2 = \frac{32e^2}{12\pi\varepsilon_0 c^2}\left(\frac{k}{2\pi m_e}\right)^{3/2} = 1.026\cdot 10^{-34} \quad [jm^2K^{3/2}s^{-1}sr^{-1}] \tag{0.27}$$

The measured emission coefficient is determined by the sum of the various components

$$\varepsilon_{total,\lambda} = \varepsilon_{fb,\lambda} + \varepsilon_{ff,\lambda}^{ei} + \varepsilon_{ff,\lambda}^{ea} \tag{0.28}$$

The total emission coefficient depends on the electron temperature and on the electron number density.

Considering a plasma characterized by a certain electron number density, from the ratio between continuum intensities of different spectral wavelengths, the term relative to n_e disappears and a Boltzmann plot can be realized to obtain the electron temperature.

A Boltzmann plot can also be realized from the ratio of line to continuum intensities, but working with integrals line profiles instead of pure intensities [9]. Also in this case the only unknown is the electron temperature.

Some limitations on the use of the Boltzmann plot derive essentially from the assumption of *pLTE* for upper levels (that can be a strong assumption in some plasmas) and from uncertainties on the values of the spontaneous emission probability coefficients.

2.3.2 Electron number density evaluation

Another important parameter is the electron temperature, that can be esteemed by several spectroscopic methods.

The first presented here is the ratio of two emission lines of the same element but proper to different systems (for example neutral and singly ionized). If the plasma is in local thermodynamic equilibrium (*LTE*), the neutral and singly ionized particle density, n_0 and n_+ respectively, are related together by the Saha equation:

$$\frac{n_e n_+}{n_0} = \frac{2U_+}{U_0}\left(\frac{m_e kT_e}{2\pi h^2}\right)^{3/2} e^{-\frac{\chi_i - \Delta\chi_i}{kT_e}} \tag{0.29}$$

where χ_i is the ionization potential and $\Delta\chi_i$ is the lowering value of χ_i due to Coulombian interactions. Writing the relation (2.31) for a neutral and singly ionized line and combining their ratio with equation (2.20)

The following relation for the electron number density is obtained:

$$n_e = \frac{A_{+k} g_{+k} \lambda_n}{A_n g_n \lambda_{+k}} \frac{2I_n}{I_{+k}} \left(\frac{m_e k T_e}{2\pi h^2} \right)^{3/2} e^{-\frac{E_{+k} - E_{n+\chi_i - \Delta\chi_i}}{kT_e}} \tag{0.30}$$

Finally, the neutral density n_0, and then the ionization degree of the plasma, can be evaluated by means of the Saha equation (2.31).

The validity of this method depends on the validity of the condition of *pLTE* for the levels of the considered transitions. It is well known from the theory of collisional-radiative processes that the upper levels of an atom reach a thermal distribution with the continuum of free electrons more easily than the lower levels. Thus, it is possible to define the levels of an atom as being in *pLTE* from level p if equation (2.32) applies to it and all higher-lying levels.

Many authors studied this problem. Griem [9], for example, studied how the emission of radiation affects the distribution with respect to excited states in hydrogen (or hydrogen-like ions) plasma. He found the following relation:

$$n_e = 7 \cdot 10^{18} \frac{z^7}{p^{17/2}} \left(\frac{kT_e}{z^2 E_H} \right)^{1/2} \quad [cm^{-3}] \tag{0.31}$$

where E_H is the hydrogen ionization energy and p is the effective principal quantum number defined as:

$$p = Z \sqrt{\frac{E_H}{E_{ion} - E_p}} \tag{0.32}$$

For atoms or ions that are not hydrogen-like, as the Ar II system is, the applicability of these criteria is a critical point. Experiments on Ar II, in fact, show that the criterion reported in equation (2.34) is too restrictive and thus this method is not used in this work.

Another way to calculate the electron density is based on the continuum emission. If the electron temperature is already measured by means of some of the aforementioned methods, the electron number density can be evaluated measuring the continuum emission coefficient and using equations (2.22), (2.25), (2.27) and (2.30).

A more reliable method, that doesn't implies any thermodynamic equilibrium assumptions, is based on the line broadening theories.

A measured spectral line is actually not a proper line, but a certain broadening and an associated profile is present.

The three major broadening mechanisms are:

- → natural broadening
- → Doppler broadening
- → pressure broadening

The natural broadening is due to the uncertainty principle that relates the lifetime of an excited state (due to the spontaneous radiative decay) with the uncertainty of its energy. This broadening effect results in an un-shifted Lorentzian profile. This kind of mechanism is always neglected in spectroscopic measurements because of its very low significance.

Doppler broadening is related to the thermal energy owned by the emitters. The atoms in a gas which are emitting radiation have a distribution of velocities. Each photon emitted will be “red” or “blue” shifted by the Doppler effect depending on the velocity of the atom relative to the observer. The higher will be the temperature of the gas, the wider will be the distribution of velocities.

Since the spectral line is a combination of all of the emitted radiation, the higher the temperature of the gas, the broader will be the spectral line emitted from that gas. This broadening effect is described by a Gaussian profile and there is no associated shift. This kind of broadening mechanism is dependent only on the wavelength of the line, the mass of the emitting particle and the temperature, and can therefore be a very useful method for measuring the temperature of an emitting gas.

The Full Width at Half Maximum (FWHM) $\Delta\lambda_D$ of the Doppler profile is given by:

$$\Delta\lambda_D = \sqrt{\frac{8kT\ln 2}{mc^2}}\lambda_0 \qquad (2.35)$$

where λ_0 is the considered wavelength, m is the atomic weight in atomic mass units (amu) and c is the vacuum speed of light.

Pressure broadening is due to collisions between emitters with neighboring particles. Pressure mechanisms are related to several reasons. In the weakly ionized Argon plasmas studied in this work, the predominant one is the Stark pressure effect.

The Stark broadening, which is produced by means of the interaction of the emitter with an electric field, causes a shift in energy which is linear in the field strength.

This mechanism is thus proportional to the Coulombian interactions between particles and so proportional to the electron number density. While the Doppler broadening mechanism is readily understood, the development of an adequate Stark broadening theory it is a quite difficult task.

The Lorentzian shape of this profile depends on the density of charged particles surrounding the emitters. Only with the recent development in computers science, a set of tables that is including both electrons and ion dynamics effects, leading to a more correct estimation of the electron number density [40], has been calculated.

For hydrogen lines the FWHM imputable to Stark effect is

$$\Delta\lambda_S = 2.5 \cdot 10^{-10} \alpha \, n_e^{2/3} \tag{2.36}$$

where α is a tabulated parameter that depends on the particular emission line and is slightly dependent on the temperature.

Another broadening mechanism not mentioned till now is the one related to the instrumentation. Each instrument inescapably introduces a dispersion due to the limited resolution owned by the instrument itself. This broadening is characterized by a Gaussian profile.

The whole line profile is so the convolution of Gaussian and Lorentzian profiles and it is generally called Voigt profile (see Figure 2.6).

The temperatures of the plasmas studied in this work generate Doppler profiles negligible compared with instrumental and Stark broadening. Obtaining experimentally the line profile and performing a de-convolution, it is thus possible to separate the Gaussian part (due to the instrumentation resolution) and the Lorentzian one useful for electron density evaluation.

In order to accomplish a reliable estimation of the electron density, Stark broadening must be at least one order of magnitude greater than instrumental broadening. For Argon lines this condition is not fulfilled, being instrumental broadening predominant. Moreover a precise treatment of Stark effect in non hydrogen-like plasmas has not yet completely been developed.

Light atoms present higher Stark broadening, thus hydrogen is the best element under this point of view. Furthermore accurate Stark broadening parameters exist for hydrogen because of its simple structure.

In this work electron number density measurements have been performed using the line broadening of the hydrogen always present as impurity.

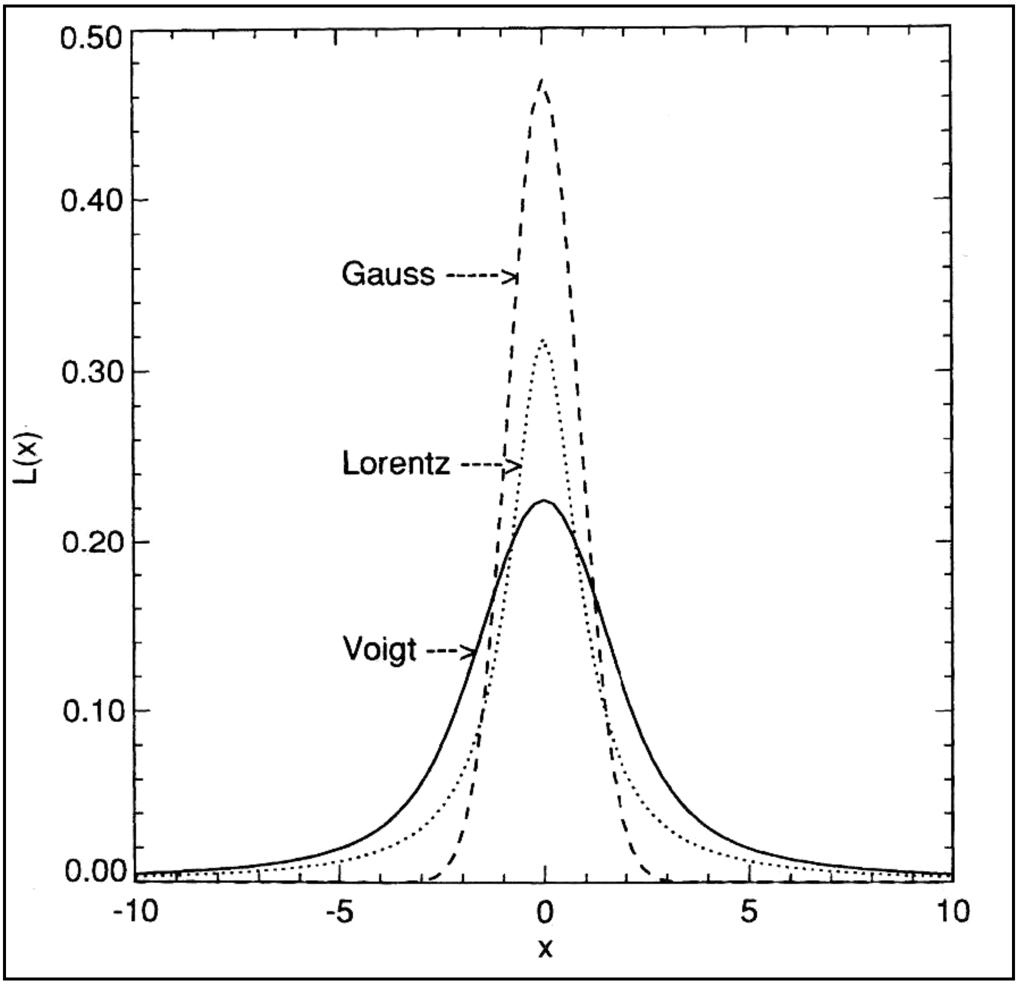

Figure 2.6 Normalized Gauss (Doppler) and Lorentz (Stark) profiles of equal FWHM. In continuous line there is the Voigt profile, convolution of these two profiles [1]

CHAPTER 3

ELECTROSTATIC PROBES

3.1 Theory of an electrostatic probe

Around 1920 Irvin Langmuir developed one of the earliest methods to obtain spatially resolved measurements of plasma properties. This technique involves the use of an electrostatic probe, named “Langmuir probe” after its inventor. It consists of a small electrode, frequently just a partially exposed insulated wire, which is inserted into a plasma. A variable DC power supply feeds the probe and is usually arranged so that the potential of the probe with respect to the plasma can be varied continuously over a range of both negative and positive values.

The current collected by the probe is determined as a function of the biasing voltage, yielding a current-voltage (I-V) characteristic, whose shape provides information concerning plasma properties. The experimental procedure to obtain such a characteristic is relatively straightforward, but the present understanding of the probes behaviour is restricted to particular plasma conditions. The reliability of an electrostatic probe as a diagnostic device for other than these special conditions is dubious and is still under investigation. An exhaustive review on the theory and the use of electrostatic probes can be found in Chen (1965), de Leeuw (1963), Schott (1968) and Cherrington (1982).

Electrostatic probes are used also for the determination of the Hall field that is generated during the MHD experiments in the low density working plasma. We will see that this field is pretty important in order to understand the physics and the performances of the MHD experiments.

When a floating conductive object (i.e. each metallic body) is immersed into a plasma, electron and ion fluxes will moves toward it charging its surface at some potential depending on the local plasma potential. The electrostatic probes that we have adopted are completely float, thus one extremity of the probe is in direct contact with the plasma, the other side is “flying". For the MHD experiments, in order to measure the potential reached by the probe, the floating terminal is connected to a scope and so linked to the ground by means of the 1[MΩ] internal resistance of the scope.

3.2 Langmuir probe device

The Langmuir probe device is aimed to determine plasma parameters in the plasma conditions specified in the following. The measured quantities are typically the electron density n_e, ion density n_i, electron temperature T_e, electron energy distribution function *EEDF*, ion temperature T_i and plasma potential ϕ_p. These quantities can be obtained from the analysis of the characteristic *I-V* plot of the probe inserted into the plasma by varying the potential difference between the plasma and the probe.

The basic underlying theory for low pressure plasmas (p ≤ 0.1 Torr) is outlined in the following. A complete treatment is given in the References [30], [34], [37] and [39] . A basic arrangement of the Langmuir probe set up is shown in Figure 3.1. The current as a function of probe voltage is referred to as the I-V characteristic and it is this characteristic which is analysed to determine the various plasma parameters. The probe dimensions are chosen to cause minimum disturbance to the plasma (typically of the order of 10 mm length and 0.15 mm diameter) and provide a localised measurement of all the key parameters with very good spatial resolution.

The Langmuir Probe characteristic is the curve obtained by plotting the probe current versus the probe voltage. The probe current is the result of the contribution of the motion of ions and electrons. Langmuir and his co-workers developed the theory of the probe and showed that the plasma parameters can be obtained through measurement by means of the probe itself.

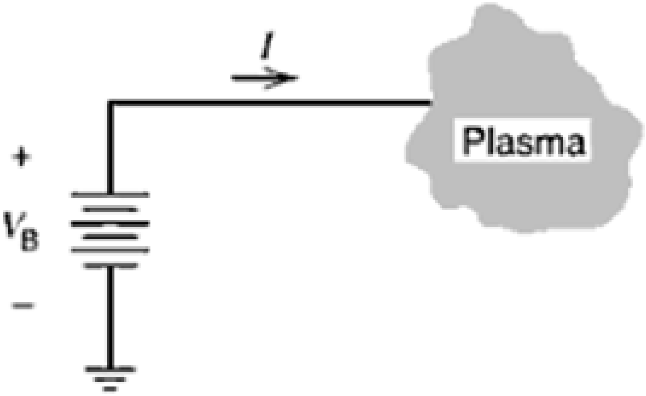

Figure 3.1 Langmuir probe setup

3.3 LP trace evaluation

A typical *I-V* characteristic for the probe measurement is shown in Figure 3.2. Here the current I_{probe} is defined as positive for flows from the probe to the plasma, and is thus equivalent to a net electron current from the plasma towards the probe. The probe voltage V_{probe} refers to the voltage applied to the probe relative to an arbitrary reference, often the anode or cathode or the plasma container.

The ion saturation region occurs for very negative probe biases and corresponds to a nearly constant probe current $I_{i,sat}$ for increasing values of the negative probe voltage. In this case around the probe there are a positive ion collection region, which is a positive sheath above the probe and from which the electrons are repelled, and an unperturbed region within the plasma with charge neutrality and into which $n_e = n_i$.

The net current collected by the probe is zero when the probe voltage is equal to the floating potential. For this the V_f is the easiest parameter to determine, a simple scan of the characteristic will yield it.

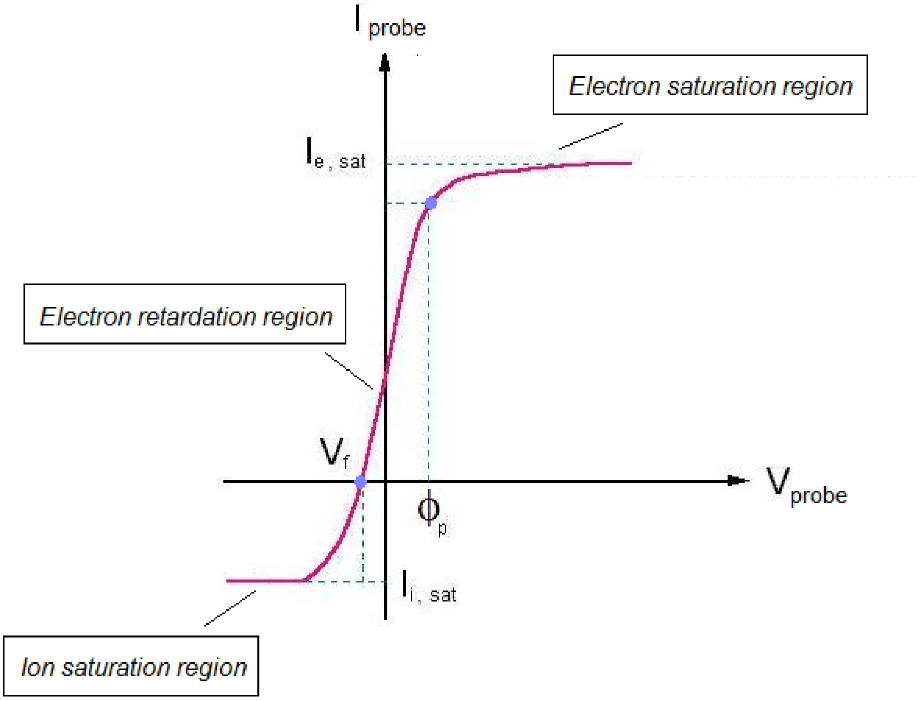

Figure 3.2 Typical current-voltage characteristic obtained with a Langmuir probe.

Most of the electrons leaving the plasma are repelled by the probe at this condition realizes equals ions and electron fluxes. For increasing V_{probe} the probe current starts to increase until the electron saturation current $I_{e,sat}$. Then the probe current remains approximately constant for further values of V_{probe}. The region corresponding to these values of V_{probe} is named electron saturation region. Here a negative sheath around the probe forms and positive ions are repelled away. For values of V_{probe} that realize current probe values in between $I_{i,sat}$ and $I_{e,sat}$ the electron retardation region is established (see Figure 2). This region is governed by the electron energy distribution function. In this lecture it is assumed that the electrons are in thermal equilibrium and hence have a Maxwellian energy distribution.

The intermediate transition region contains the electron energy information since the increasing positive probe voltage repels electrons of progressively higher energies and hence samples the distribution of electron energies. The transition region is a composite of both electron and ion current and for proper analysis ion current and electron current must be de-coupled. This is usually accomplished by fitting a function to the ion current deep in the saturation region and extrapolating it back through the transition zone. This ion current function is then subtracted from the raw V_{probe} vs I_{probe} data to produce the electron current characteristic. The analysis of the characteristic then follows utilising several well known theories of interpretation.

The plasma potential ϕ_p is the voltage inside the plasma. It is always positive with respect to the most positive body with which it is in contact. In many cases, the plasma potential provides a good indication of the energy of positive ions incident on surfaces of interest. . The plasma potential is the probe voltage corresponding to the intersection of the fitted electron saturation and transition lines.

The potential difference V_S between the plasma potential and the probe potential represents the voltage across the sheath probe edge and the unperturbed plasma.

$$V_S = \phi_p - V_{probe} \tag{3.1}$$

The ion saturation current is given by:

$$I_{i,sat} = e\ n_e A_{probe} (Z_i kT_e / M)^{1/2} \tag{3.2}$$

Considering that the ion saturation current $I_{i,sat}$ is a known measured value, the electron temperature is found by fitting a line to the transition region, be evaluated as the slope of the straight line fitting the data in a semi-log graph $\ln(I_{probe}-I_{i,sat})-V_{probe}$. And is equal to the negative inverse of the slope of this line. (in units of [eV]).

$$I_{probe} = I_{i,sat}\left(\frac{e(V_{probe} - V_f}{kT_e} - 1\right) \tag{3.3}$$

The equation can be written in the following form:

$$I_{probe} = I_{i,sat}\left(\frac{e(V_{probe} - V_f}{kT_e} - 1\right) \tag{3.4}$$

An alternative method for determining the temperature for positive values of V_s is given by the following relation:

$$\frac{kT}{e} = I_{i,sat}\left[\frac{\mathrm{d}\,V_{probe}}{\mathrm{d}\,I_{probe}}\right]_{I_{probe}=0} \tag{3.5}$$

The electron density is simply the number of electrons per unit volume within the plasma. - Ion Density The ion density is the number density of the ions per unit volume within the plasma. Ions can be negative or positive. For an electropositive discharge, all ions formed in the plasma have a positive charge and the ion and electron densities in the bulk of the plasma are equal. For an electronegative discharge, the ions may be either positive or negative, in which case the sum of electron and negative ion densities must equal the positive ion density.

Once the ion saturation current and the electron temperature is known, the electron density can be evaluated by mean the following relation:

$$n_e = \frac{e\ A_{probe} v_0}{I_{i,sat}} \tag{3.6}$$

where $v_0{}^2 = Z_i k T_e / M$ is the Bohm velocity.

The Electron Energy Distribution Function is determined by the Druyvesteyn method which uses the second derivative of electron current with respect to voltage as calculated from the electron current characteristic.

$$f_{EEDF}(V_{probe}) = \frac{-4}{A_{probe}e^2}\left(\frac{m_e(\Phi_p - V_{probe})}{2e}\right)\frac{d^2 I_{e,sat}(V_{probe})}{dV_{probe}^2} \tag{3.7}$$

3.4 Double and triple probes

The double probe is an electrode biased relative to a second electrode, rather than to the vessel. The theory is similar to that of a single probe, except that the current is limited to the ion saturation current for both positive and negative voltages. One advantage of the double probe is that neither electrode is ever very far above floating, so the theoretical uncertainties at large electron currents are avoided. If it is desired to sample more of the exponential electron portion of the characteristic, an asymmetric double probe may be used, with one electrode larger than the other. The characteristic in this case is still a hyperbolic tangent, but shifted vertically. Another advantage is that there is no reference to the vessel, so it is to some extent immune to the disturbances in a radio frequency plasma. On the other hand, it shares the limitations of a single probe concerning complicated electronics and poor time resolution. In addition, the second electrode not only complicates the system, but it makes it susceptible to disturbance by gradients in the plasma.

Here we have a typically shape of a double probe. For the determination of plasma parameters can be performed using the same procedure use for single Langmuir probe case.

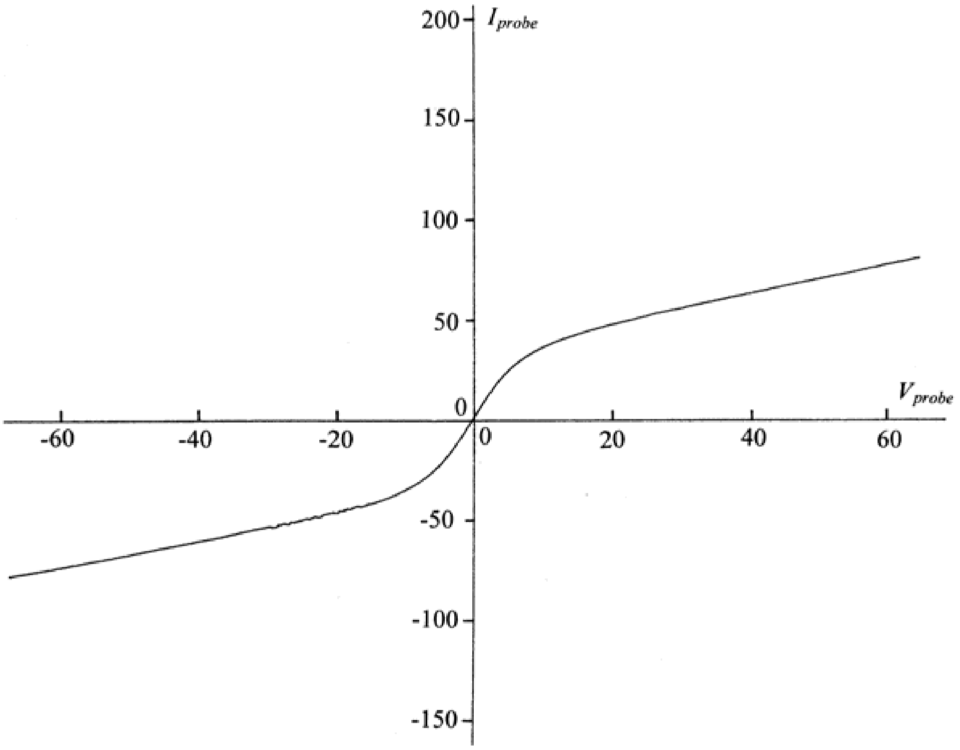

Figure 3.3 Double probe I-V characteristics

An elegant electrode configuration is the triple probe, consisting of two electrodes biased with a fixed voltage and a third which is floating. The bias voltage is chosen to be a few times the electron temperature so that the negative electrode draws the ion saturation current, which, like the floating potential, is directly measured. A common rule of thumb for this voltage bias is 3 times the expected electron temperature in [eV].

Triple probes have the advantage of simple biasing electronics (no sweeping required), simple data analysis, excellent time resolution, and insensitivity to potential fluctuations (whether imposed by an radio frequency source or inherent fluctuations). Like double probes, they are sensitive to gradients in plasma parameters.

Arrangements with four (called tetra probe) or five (penta probe) have sometimes been used, but the advantage over triple probes has never been entirely convincing. It should be noted that the spacing between probes must be larger than the Debye length of the plasma to prevent an overlapping Debye sheath.

PART II

Experiments on MHD interaction

CHAPTER 4

FUNDAMENTALS OF MHD

4.1 A brief history of Magnetohydrodynamics

The laws of magnetism and fluid flow are hardly a twentieth-century innovation, yet MHD become a fully fledged subject only in the late 1930s and early 1940s. The reason, probably, is that there was little incentive for nineteenth-century physicists such as Faraday (he tried to measure the voltage across the Thames induced by its motion throughout the earth's magnetic field), the subject languished until the turn of the century. Things started to change, however, when astrophysicists realize just how ubiquitous magnetic field and plasmas are throughout the universe. This culminate in 1942 with the discovery of the Alfvèn wave, a phenomenon which is peculiar to MHD (a magnetic field line can transmit transverse inertial waves, just like a plucked string).

Hypersonic flight is nowadays receiving big improvements both in aeronautical and astronautically fields.

The Mach 10 fight of the concept unmanned aircraft X43-A performed in November 2004, is the demonstration of the possibility to realize a hypersonic atmospheric vehicle. On parallel plane, the development of a Single Stage To Orbit (SSTO) vehicle is actually one of the main pre-requisite for the commercial exploitation of the space fight.

When aircrafts flies at high altitudes and high speeds, a gas-dynamic shock in front of the vehicle occurs. This causes a compression of the gas and a strong heating of it. The temperature reaches values up to $10000^{\circ}[K]$ or even larger than this value (especially for re-entry vehicle into the atmosphere).

Close to the fuselage surface the temperature is sufficient to cause ionization of the gas and a weakly ionized plasma is formed. The presence of free charged particles suggested the use of electromagnetic forces able to modify the fluid-dynamics around the aircraft 174 Introduction to MHD applications in the hypersonic fight

This purpose may be realized by means of the Magnetohydrodynamic interaction (MHD). Applying strong magnetic fields (of the order of the Tesla), the generation of body forces on the gas particles surrounding the plane is indeed possible

In the last years several studies on the interaction of hypersonic flows with plasmas and with the MHD process have been realized . These studies mainly dealt with the control of the fluid dynamic phenomenon in the region between the shock front and the surface of the vehicle, and acquisition of knowledge about hypersonic shock layers.

In re-entry vehicles, MHD interaction could decrease thermal fluxes toward the fuselage walls and this may result in a thermal protection by means of an active magnetic shield [41, 42]. Moreover the aerodynamic drag and the vehicle trim will be modified.

Generally, in hypersonic aircrafts, fight control without the meaning of moving parts and the active control of shock waves inside air-breathing engines for a better combustion could be realized.

In the Russian AJAX project MHD techniques are utilized to by-pass kinetic energy of the working fluid inside the engine, from the supersonic diffuser to the nozzle. By doing this, the flow velocity in the combustion chamber is reduced to acceptable values, even for high Mach numbers.

The knowledge of the physics of the MHD-hypersonic flow interaction is essential for the application of this technology to the hypersonic fight.

So far, experimental investigations on the MHD interaction at high velocities have been performed in hypersonic wind tunnels by means of few research groups.

Bityurin et al. realized experiments on a blunt body with air as working fluid [43, 44]. Borghi et al. performed experiments in Argon studying the MHD fluid-dynamics modification over a wedge [5].

In this work we present a series of MHD experiments realized on an axial symmetric test body immersed in an argon Mach six plasma flow.

In the first part a complete aero-thermodynamic and electrical characterization of the plasma flow is performed comparing experimental and numerical results.

In the second part imaging, pressure and electrical results on the MHD interaction measurements are reported.

Finally a numerical investigation is realized in order compare MHD results coming from measurements and simulations, in order to validate the numerical code developed by means of the Bologna University team.

4.2 From EHD to MHD

From Electrodynamics is pass to Magnetohydrodynamics, the difference lies in the fluidity of the conductor. The MHD is the interaction between moving conducting fluids and magnetic field.

The mutual interaction of a magnetic field B and a velocity fluid u, arises partially as a result of the laws of Faraday, Ampère and because of the Lorentz (Laplace) force experienced by a current-carrying body.

The governing equations of MHD consist simply of Newton's laws of motion and the pre-Maxwell form of the laws of electrodynamics. For this introduce some notation: μ the permeability of the free space, σ and ρ denote the electrical conductivity and density of the conducting medium, respectively, and l the characteristic length scale. After this list the three important parameters in MHD are:

Magnetic Reynolds number

$$R_m = \mu \sigma u l \tag{4.1}$$

Alfvèn velocity:

$$v_a = \frac{B}{\sqrt{\rho\mu}} \tag{4.2}$$

Magnetic damping time:

$$\tau = \left[\frac{\sigma \ B^2}{\rho}\right]^{-1} \tag{4.3}$$

The first of these parameters may be considered as a dimensionless measure of the conductivity, while the second and third quantities have the dimensions of speed and time, respectively, as their names suggest.

Now we have already hinted that magnetic field behave very differently depending on the conductivity of the medium. In fact, it turns up to be R_m, rather than σ, which is important. Where R_m is large, the magnetic field lines act rather like elastic bands frozen into the conducting medium. This has two consequences. First, the magnetic flux passing through any closed material loop (a loop always composed of the same material particles) tends to be conserved during the motion of the fluid. Second, as we shall disturbance of the medium tends to result in near-elastic oscillations, with the magnetic field providing the restoring force for the vibration. In a fluid, this results in Alfvèn waves, which turn out to have a frequency of $\omega \approx v_a / l$ .Where R_m is small, on the other hand, u has little influence on B, the induced field being negligible by comparison with the imposed field. The magnetic field then behaves quite differently. We shall see that it is dissipative in nature, rather than elastic, damping mechanical motion by converting kinetic energy into heat via Joule dissipation. The relevant time scale is now the damping time τ, rather than l / v_a.

4.3 The governing equations of MHD

The whole MHD phenomenon has been analyzed utilizing a two dimensional, low R_m model. The advection of the magnetic field is so relatively unimportant and it will tend to relax towards a purely diffusive state, determinate by the boundary conditions rather than the flow motion. The fluid-dynamic equations are given by the continuity equation for mass, momentum and energy and by the state equations of gas as follows:

$$\begin{aligned} &\frac{\partial \rho}{\partial t} + \nabla \cdot (\rho\, \mathbf{u}) = 0 \\ &\frac{\partial \rho\, \mathbf{u}}{\partial t} + \nabla \cdot (\rho\, \mathbf{u}\mathbf{u} + \mathrm{p}\mathbf{I} - \tau) = \mathbf{J} \times \mathbf{B} \\ &\frac{\partial \rho e_i}{\partial t} + \nabla \cdot [(\rho e_i + \mathrm{p})\mathbf{u}] - \nabla \cdot\cdot (\tau \cdot \mathbf{u}) + \nabla \cdot F_T = \mathbf{J} \cdot \mathbf{E} \end{aligned} \tag{4.4}$$

The physical model of the electrodynamics has been obtained assuming the condition R_m <<1. Under this assumption, some useful approximations can be applied [45].

Most notably, when an externally generated magnetic flux density B_0 is applied to the plasma flow (i.e. a magnetic flux density produced by electric current), the magnetic flux density $\boldsymbol{B_j}$ due to the current density in the plasma can be neglected.

Thus, the total magnetic flux density **B** may be considered equal to the externally applied field $\mathbf{B_0}$. Furthermore, assuming that the applied magnetic flux density does not vary in time or it varies slowly, one can neglect the time derivative term in the Faraday Lenz's law:

$$\nabla \cdot \mathbf{E} = 0 \tag{4.5}$$

Another convenient approximation can be utilized, assuming the characteristic time for the macroscopic variations much greater than the inverse of the plasma frequency:

$$t_c >> \frac{1}{\omega_p} \tag{4.6}$$

When eq. (4.4) hold on the displacement current density, given by the time derivative of the electric displacement field **D,** may be neglected compared to the conduction current density. The Ampere Maxwell law can then be rewritten as follows:

$$\nabla \cdot \mathbf{H} = \mathbf{J} \tag{4.7}$$

According the divergence operator to equation (4.5) the curl free electric field **E** may be expressed as the gradient of a scalar potential Φ:

$$\mathbf{E} = -\nabla\Phi \tag{4.8}$$

Applying then the divergence operator to equation (4.6) the following equation can be written as well:

$$\nabla \cdot \mathbf{J} = 0 \tag{4.9}$$

The electrodynamic model is completed by the generalized Ohm's law, which is here reported neglecting the ion Hall parameter and the electron pressure gradient (bothconsidered of a second order importance):

$$\mathbf{J} = \sigma(\mathbf{E} + \mathbf{u} \times \mathbf{B}) - \beta_e \frac{\mathbf{J} \times \mathbf{B}}{B} \tag{4.10}$$

where $\beta_e = \mu_e B$

Assuming a reference system where the gas velocity **u** and the magnetic flux density **B** lie on the r-z plane and the electromotive force **uxB** is directed along the φ- axis, eq. (4.10) can be written as follows:

$$\mathbf{J} = \bar{\sigma}(\mathbf{E} + \mathbf{u} \times \mathbf{B}) \tag{4.11}$$

where the conductivity is expressed by means of a tensor

$$\bar{\sigma} = \frac{\sigma}{1+\beta_e^2} \begin{bmatrix} 1+\beta_e^2 & \beta_z\beta_r & \beta_r \\ \beta_z + \beta_r & 1+\beta_r^2 & -\beta_r^2 \\ -\beta_r & \beta_z & 1 \end{bmatrix} \tag{4.12}$$

the two components of β are describe as:

$$\begin{aligned} \beta_z &= B_z \frac{\beta_e}{B} = \mu_e B_z \\ \beta_r &= B_r \frac{\beta_e}{B} = \mu_e B_r \end{aligned} \tag{4.13}$$

For the solution of the magnetohydrodynamic problem, a two dimensional model has been developed.

In order to get an insight of the electrodynamics in the proposed geometry, an annular flow may be considered the gas flows in the *z* direction with velocity **u**, an electric field **B** in *r* direction and $E_\varphi = 0$.

As the magnetic flux has to be conserved , **B** decreases with the radius:

$$B_r(r) = B_{r_0}\frac{r_0}{r} \tag{4.14}$$

The eq. (4.14) allows us now to the determination of the three components of the current:

$$\begin{aligned} J_z &= \frac{\sigma}{1+\beta_e^2}\left(E_z + \beta_e uB\right) \\ J_r &= \beta E_r \\ J_\varphi &= \frac{\sigma}{1+\beta_e^2}\left(-\beta_e E_z + uB\right) \end{aligned} \tag{4.15}$$

Assuming that the insulating wall of the cannel does not allows the current density to flow in the *r* direction (as in our experiment when we have the presence of the insulating nylon shied) the condition:

$$E_r = 0 \tag{4.16}$$

holds.

As a consequence, the scalar electric potential is constant along the *r* direction and is only function of the *z* variable.

In order to maximize the azimuthally current density J_φ, one should set the total current flowing in the z direction equal to zero:

$$I_z = \int_{r_0}^{r_1} J_z r dr \approx \sigma \int_{r_0}^{r_1} \frac{\left(E_z + \beta_e uB\right) r}{\beta_e^2} dr = 0 \Rightarrow E_z = -\frac{2\mu_e u\left(B_0 r_0\right)^2}{r_0^2 + r_1^2} \tag{4.17}$$

From the obtain expression of the electric field in the Hall direction, the azimuthally component of current density can be evaluated as:

$$j_\varphi \approx \frac{2\sigma\ uB_0 r_0 r}{r_0^2 + r_1^2} \tag{4.18}$$

And shows how the axial symmetric geometry, as azimuthally component of the current density is ideally not affected by an high Hall parameter when the current flow in the *z* direction is not allowed.

The two dimensional proposed model has been so characterized by a calculation domain positioned in the *r-z* plane.

In the reference system fixed with the body, the gaseous medium flows with hypersonic velocity **u** lying on the *r-z* plane. The magnetic flux density **B**, that generates the MHD interaction, lies on the *r-z* plane too. Thus the electromotive force **u**x**B** is directed along the '-axis .

As seen before, the current density **J** has an azimuthally component along the φ-axis and an Hall one on the *r-z* plane.

A cell-centred finite volume formulation has been adopted for the spatial discretization of the fluid dynamics.

Fluxes are evaluated by means of a centred scheme, corrected by an Oesher scheme. A second order accuracy is obtained by a combination of upwind and cantered discretization of the gradient.

Time integration is performed utilizing an explicit scheme, based on a fourth order Runge-Kutta method.

Electrodynamics may be considered to vary as a sequence of steady state solutions driven by the evolution in time of the fluid dynamics. This is because, in the whole of the assumptions described above, the electrodynamics has a negligible characteristic time compared to the fluid dynamics.

Electrodynamic quantities are accordingly assumed to adapt themselves instantaneously to the time variation of the flow field.

The steady state electrodynamic problem defined by eq. (4.16) is solved by means of a finite element approach.

On the discredited domain a piecewise approximation ϕ^* of a scalar potential ϕ can be introduced by means of the shape function $\{N\}$:

$$\phi^*(x, y) = \{N\}^T \{\phi\} \tag{4.19}$$

where $\{\phi\}$ is a vector containing the nodal value of the unknown electric scalar potential

An expression for the approximate electric field and current density may be written as:

$$\begin{aligned} \mathbf{E}^* &= -[\nabla N]\{\phi\} \\ \mathbf{J}^* &= -\overline{\sigma}([\nabla N]\{\phi\} + \mathbf{u} \times \mathbf{B}) \end{aligned} \tag{4.20}$$

Applying the divergence theorem to the vector $N\mathbf{J}^*$, can written the following equation

$$\int_{\Omega} N\nabla \cdot \mathbf{J}^* d\Omega + \int_{\Omega} \nabla N \cdot \mathbf{J}^* d\Omega = \int_{\partial\Omega} N\nabla \cdot \mathbf{J} n^* d\Omega \tag{4.21}$$

Setting to zero the weighted residual of eq. (4.19):

$$\int_{\Omega} N\nabla \cdot \mathbf{J}^{*} d\Omega = 0 \tag{4.22}$$

the final FEM formulation for the electrodynamic problem can be written as:

$$-\int_{\Omega} N\nabla \cdot \overline{\sigma}(\mathbf{u} \times \mathbf{B}) d\Omega - \int_{\partial\Omega} N \cdot \mathrm{J}n^{*} d(\partial\Omega) = \int_{\Omega} N\nabla \cdot \overline{\sigma}[\nabla N]\{\phi^{*}\} d\Omega \tag{4.23}$$

The solution of the linear system obtained from eq. (4.23) yields the nodal values of the electric scalar potential once the conductivity tensor, the flow velocity and the magnetic flux density are given.

The coupling between the fluid and the electrodynamics is accomplished quite straightforwardly.

As previously stated, the time dependent behaviour of the model is governed by the fluid dynamics. At the generic nth time step, the fluid dynamic solver evaluates the source terms in the continuity equation for momentum and energy utilizing the values of **E** and **J** calculated at the previous time step. The steady state electrodynamic model then utilizes the value of **u** at the nth step to compute **E** and **J**.

These quantities will be utilized as input for the (n +1)th time step of the fluid dynamic solver.

CHAPTER 5

NON – INTRUSIVE NOZZLE CHARACTERIZATION

5.1 Hypersonic Wind Tunnel Facility

The MHD hypersonic tests have been all performed inside the Alta High- Enthalpy Arc-heated hypersonic wind Tunnel (Alta SpA Pisa). The HEAT facility that is able to produce an air ionization flow at Mach 9 and in Argon at Mach 15 in a low to medium Reynolds number range (10^4-10^6). The characterization of the hypersonic plasma produced by HEAT is of fundamental importance for the numerical rebuilding of the experiments and for the interpretation of the experimental results.

In this section we will deal with the description of the wind-tunnel facility and its aero-thermodynamic characterization realized by the Alta team. The electrical characterization of the plasma jet will be largely discussed in the next two sections.

The core of the facility is the arc-heater chamber. A scheme of the fundamental components of this section is reported in Figure 5.1.

In the wind-tunnel heating chamber there are two electrodes: a cylindrical tungsten cathode and an annular copper anode, separated by a boron nitride constrictor. The gas is heated up by means of an arc discharge powered by a 260[kW] DC power supply, delivering arc currents up to 630[A]. The running times can hold up from 20 at 300[ms]. A total specific enthalpy of up to 6 [MJ/kg] in air with stagnation pressures of up to 9[bar] can be obtained.

The heater allows the installation of a pressure transducer for total pressure measurement, whereas total enthalpy is measured indirectly by means of a temperature probe placed in front of the nozzle exit area.

HEAT is a pulsed, blowdown, arc-heated tunnel, which can operate with air, argon, helium and CO_2 for a typical test time of 50-300 ms. The gas is loaded into two tanks and is injected into the heater at the beginning of the run by means of two fast opening solenoid valves SMC T307-317.

The nozzle was manufactured in Alta's workshop. The divergent part, in glass reinforced nylon, was machined in two separated halves successively glued together. The convergent and throat are a single part in brass.

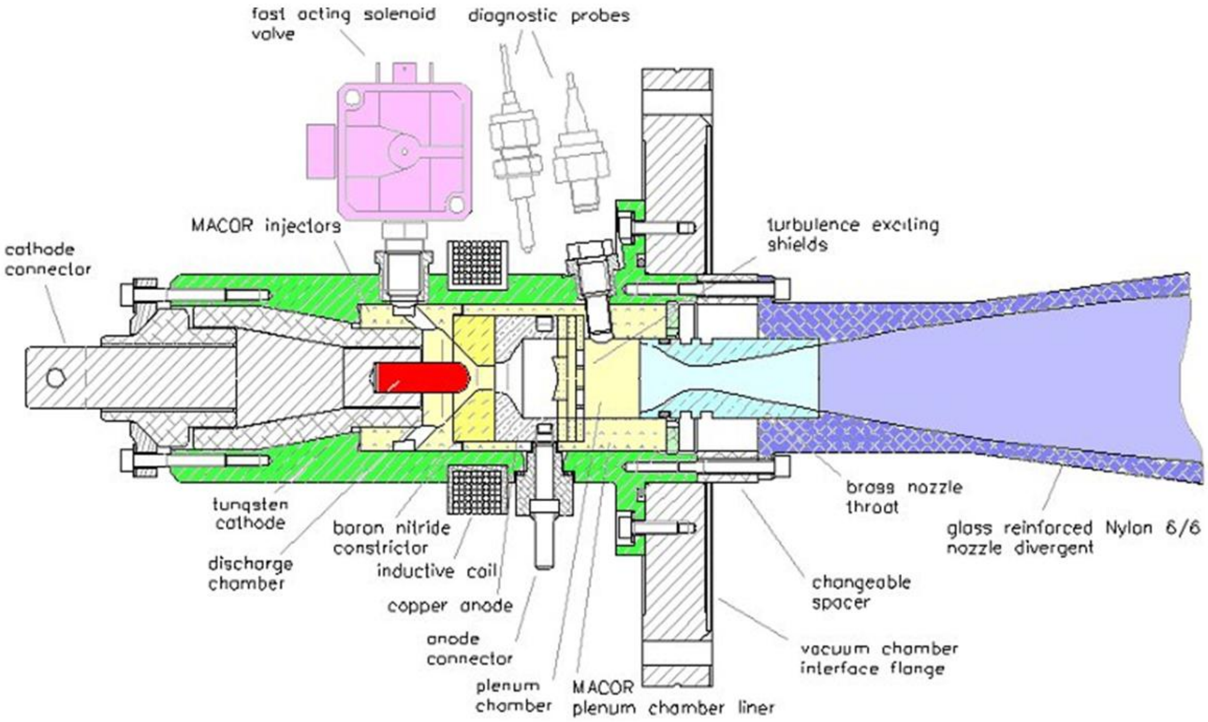

Figure 5.1 Arc-heater scheme

At the exit of the settling chamber, was mounted a conical nozzle with a throat diameter of 12[mm]. On the side of the nozzle “mouth”, the diameter section arrived at 140 [mm].

The wind tunnel (gas heater and nozzle) is installed on a vacuum test section of 600[mm] length. In the test section, there are optical accesses from all sides. This section is connected to a vacuum chamber with a volume of 4.1[m^3]. Nozzle and vacuum chamber are shown in Figure 5.2 and Figure 5.3.

Before each run, the chamber is evacuated by means of four rotary pumps to reach an ultimate pressure of 10[Pa]. The test gases used in this experiment are air and Argon. The nozzle Mach number for air was 9 and for Argon 15.

A series of preliminary tests allowed the identification of the best conditions for the arc discharge. The arc voltage was between 55 and 65[V] for all the test conditions. Three typical test conditions with a heating-chamber pressure ranging between 0.5 and 0.7[bar]are considered. Pressure fluctuations are observed at pressures below 0.5[bar]. This is due to the turbulence created in the heating chamber.

The stagnation pressure and temperature are given by the pressure measured in the heating chamber.

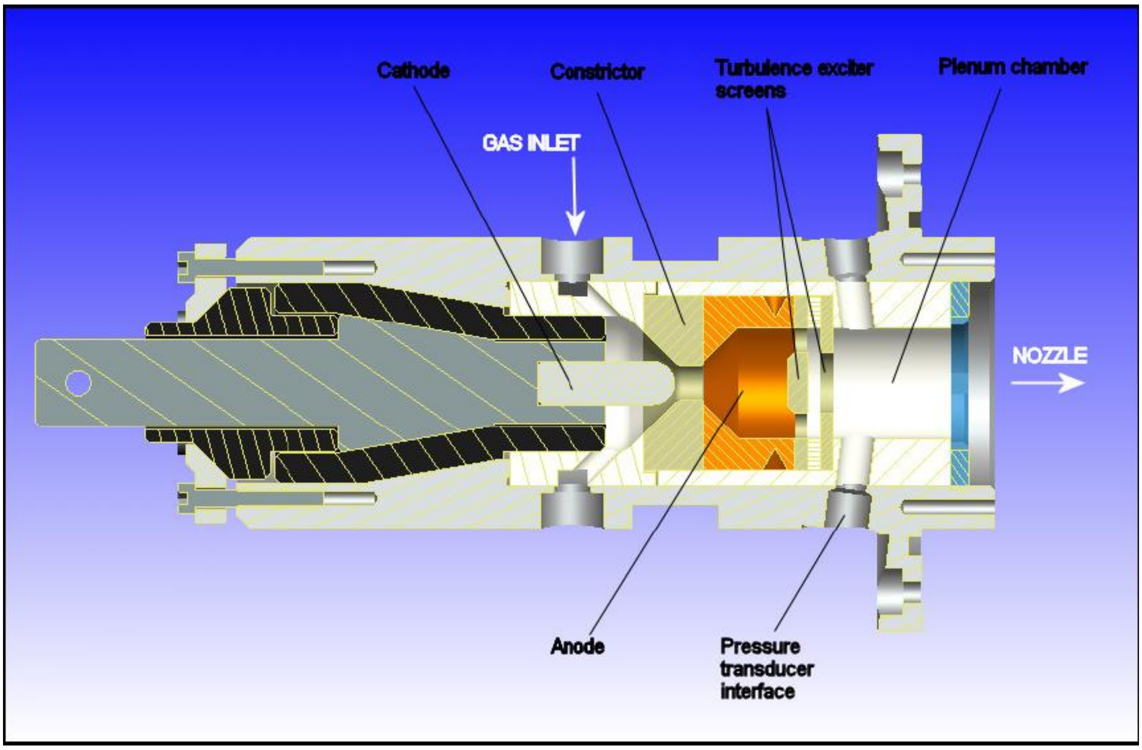

Figure 5.2 Arc-heater cross section

Figure 5.3 HEAT vacuum chamber

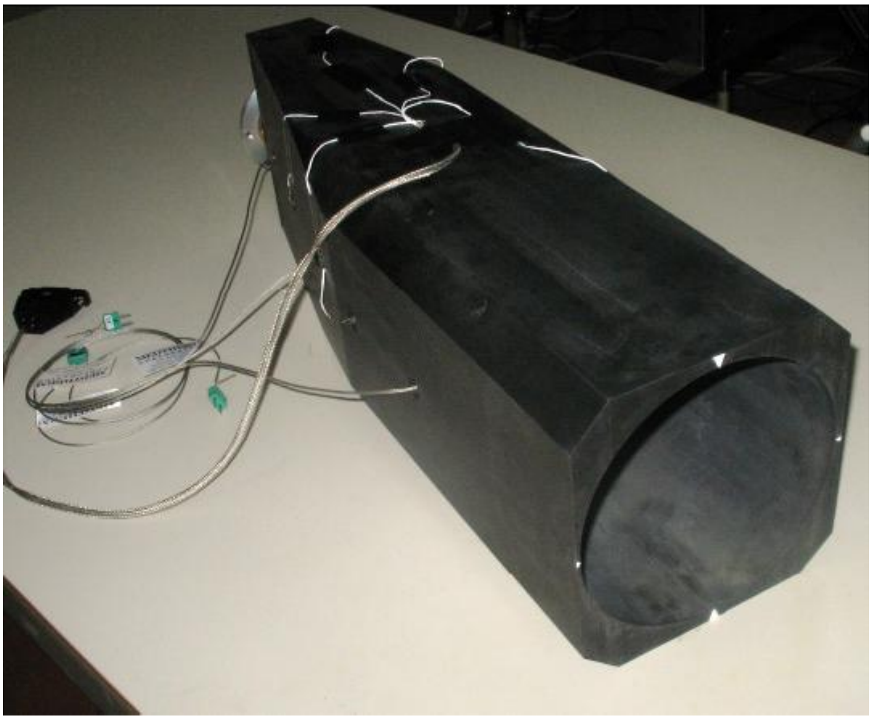

Figure 5.4 Nozzle mounted at the exit of the heating chamber

According to the specification, the new nozzle was required to produce a uniform flow with a Mach number comprised between 8 and 10 and a core diameter of at least 80 mm, for nominal stagnation conditions of 4.5 MJ/kg and 3 bar in air. In addition, other requirements were imposed by the facility itself: in fact, in order to perform sufficiently accurate and repeatable measurements, a minimum usable test time of 90 milliseconds was needed. Because the main limit on the test time is the pressure raise in the vacuum chamber, this implies a lower limit on the nozzle exit pressure.

Another constraint concerns the overall nozzle length: to make optical measurements possible the exit section must be in correspondence of the central window of the test section. To have an overview of how these constraints condition the design parameters a preliminary study was carried out.

The simple computational procedure has been implemented. The method assumes as independent variables the Mach number, the stagnation conditions and the test time and considers the gas as calorically perfect. In addition to the geometrical exit diameter D_{geom}, two further diameters have been defined, the diameter of the core flow D_{core} and the effective diameter D_{eff}, that corresponds to the area that conserves the mass flow when the exit velocity is supposed to be uniform and equal to the core velocity.

$$D_{core} = D_{geom} - 2\delta \tag{5.1}$$

$$D_{eff} = D_{geom} - 2\delta^{*} \tag{5.2}$$

where δ and δ* are respectively the boundary layer thickness and the displacement thickness and they are both evaluated by means of the empirical relations available in literature modified to improve the agreement with experimental data obtained for Alta's other existing nozzles.

It is worthy to observe that isentropic area relation holds only for effective area. Running the procedure for three different values of the Mach number, the results of Table 1 are obtained.

Mach number [-]	Throat diameter [mm]	Core diameter [mm]	Exit diameter [mm]	Nozzle length [mm]
8	9.77	108	144.4	640.6
9	6.64	95.5	146.5	665.5
10	4.68	96.4	171.6	793.8

Table 1 Results of the preliminary nozzle sizing

It's seen that a Mach 10 nozzle was not particularly suitable because its excessive length and small throat diameter, that could be a challenging task for manufacturing. For this reason 9 has been chosen as design Mach number for the new nozzle.

The inviscid contour of the nozzle has been generated by means of a two-steps iterative procedure. In the first step a perfect gas with constant specific heat ratio γ is considered and the profile is calculated using the classical method of characteristics (see Figure 5.5).

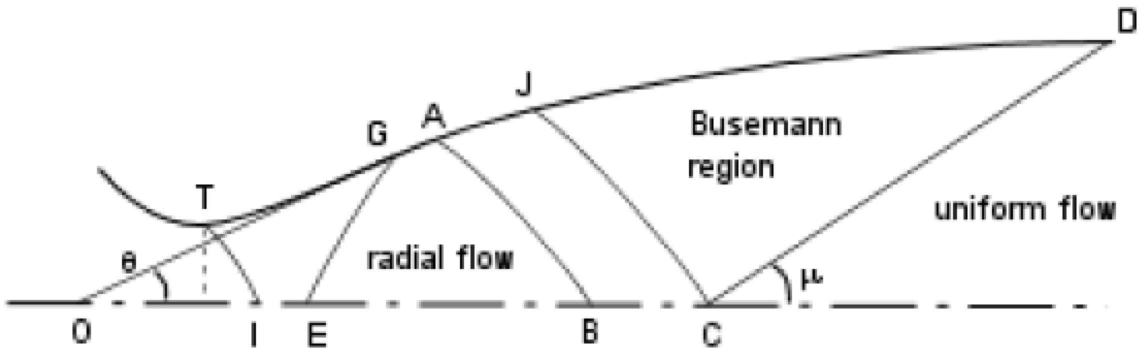

Figure 5.5 Nozzle mounted at the exit of the heating chamber

The calculation starts from the throat characteristic where the flow is known by a transonic solution, the bulk of expansion occurs through a zone of radial flow EBAG and the transition to uniform flow is accomplished within the so called Busemann region JCD. In order to avoid discontinuities in the first two derivatives of Mach number profile, two additional zones with polynomial distribution of Mach number on the axis are added before and after radial expansion

In the second step, the one-dimensional flow through the nozzle is calculated numerically with the code NENOZ-2, a 2_{nd} order precision finite-difference solver for quasi 1-D, isentropic and stationary flows, that can take into account for both vibrational and chemical non-equilibrium. A reduced Kang-Dunn model is used for chemical kinetics (only neutral species are considered).

If the exit Mach number, predicted by NENOZ-2, differs from the nominal one for more than a quantity ε, a new MOC calculation is carried out with a modified value for γ. The procedure is repeated until convergence is reached.

In Figure 5.6 the comparison between the Mach number profile calculated with NENOZ-2 and the one predicted by CIRA simulations is shown for the definitive inviscid profile.

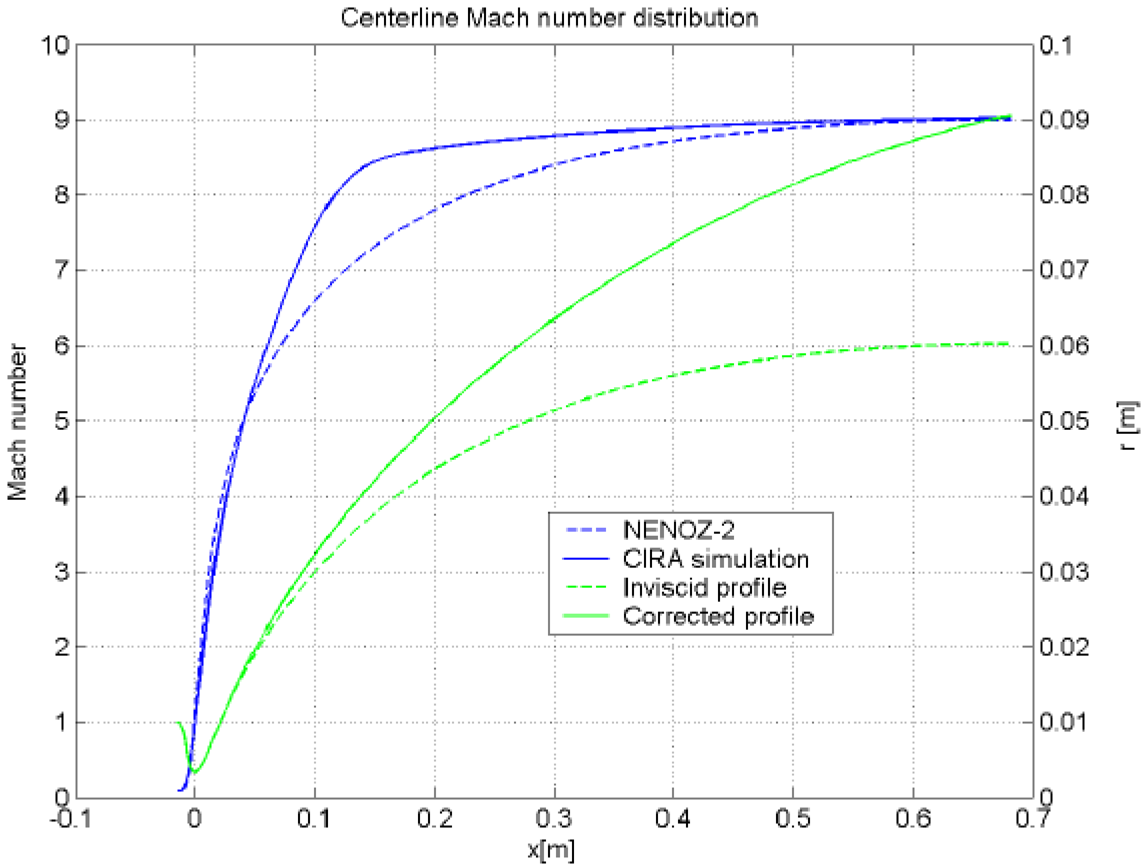

Figure 5.6 Centerline Mach number distribution

For the aero-thermodynamic characterization of the produced flow, the following set of instruments was used:

- two absolute Kulite XCS-062 sensors in the tunnel settling chamber (one with a 250[psi] FSO and one 100[psi])
- a supersonic pitot probe equipped with a Kulite XCS-062-5A miniaturized pressure sensor for high frequency Mach number retrieval
- a hemispheric stagnation point temperature probe equipped with a MEDTHERM coaxial thermocouple for the stagnation enthalpy and total enthalpy retrieval through the Sutton-Graves relations

The total enthalpy was evaluated from the arc-discharge power and compared with the values obtained from the stagnation temperature measured in the test section. The total-enthalpy error was +/- [5% -10%].

The plasma jet has been fluid-dynamic characterized by the Alta team. The results are showed as follow.

The characterization activity allowed to the determination of the core-flow dimensions, the axial-symmetry degree of the flow, the fluctuations of the Mach number, and the temperature and repeatability of the test conditions.

In the Figure 5.7, a typical radial profile of the Mach number is shown. The core flow Mach number is 15.7 ± 0.4.

This chapter describes the results of an experimental investigation on the effect of the MHD interaction in the plasma of the shock layer above a test body immersed into a hypersonic Argon flow. An extensive activity was carried out in order to quantitatively characterize the weakly ionized free stream, for pressures in the range between 0.5 and 1.5 bar.

Two different models, with embedded high field permanent magnets are going to be used: a sharp cone (used in the presented work) and a truncated-cone blunt body. The models are equipped with surface pressure and temperature measurement devices and electrostatic probes. Two geometrically identical, non magnetic models were used to compare results with and without MHD interaction. This paper will describe the experimental setup, the characterization activity, and the test campaign results.

A short critical analysis on the obtained results will be also present including comparison with the past experiments conducted in Alta by the same team.

This work was performed within the “Advanced Aerothermodynamics Configurations for Space Transport” (CAST) project dedicated to the development of an advanced simulation tool for ascent and re-entry simulation within the Italian aerothermodynamics community, with the creation of a dedicated experimental data base.

The target of CAST is the development, verification and validation of a CFD code able to accurately simulate the complex phenomenology occurring in a real gas flowing at hypersonic velocity and with a high stagnation enthalpy.

Effects like dissociation, ionization, chemical and vibrational non-equilibrium, radiative heat exchange, etc. need all to be taken into account in order to correctly predict the mechanical and thermal loads acting on the surface of a launcher or a space vehicle entering the atmosphere. The activities concerning CAST can be grouped in three main categories: physical modelling, numerical implementation of the models and experimental validation. In order to perform an effective validation of the code, several test cases concerning different aspects of aerothermodynamics have been identified and included in the test schedule: shock wave-boundary layer interaction (SWBLI), magnetohydrodynamics (MHD) interaction, base flow behind a rocket, etc.

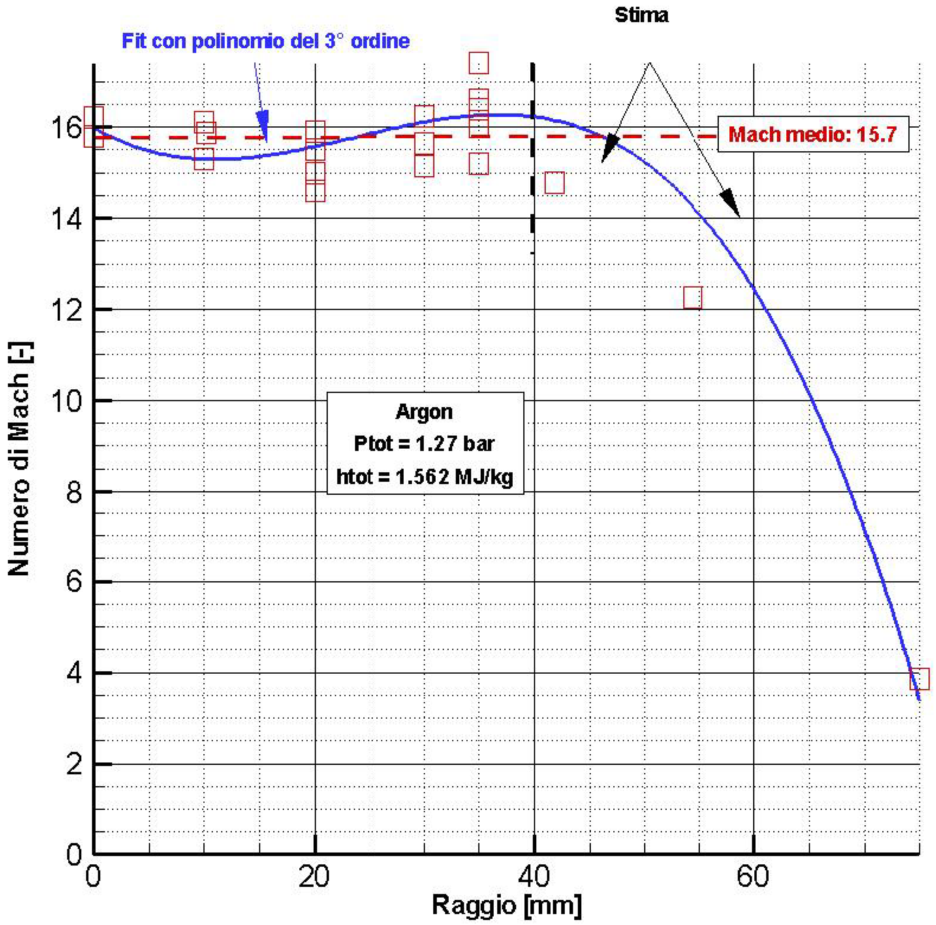

Figure 5.7 Mach number distribution at the nozzle exit section

5.2 Flow Characterization

The fluid-dynamic measures of the plasma jet gave us information about velocity, pressure and temperature of the Mach 9 and 15 flow.

For a more complete comprehension of the features of the plasma, an electrical characterization have been realized in order to infer important plasma parameters as the electron temperature and electron number density.

Two different plasma diagnostics have been applied to characterize the system.

In the arc heater plenum chamber, optical emission spectroscopy has been utilized to obtain both electron excitation temperature and electron density for Argon and vibrational temperature for Air.

In the Argon flow, excitation temperature, which has been measured by means of the Boltzmann plots of continuum and spectral lines, can be considered a good estimation of electron temperature. Electron number density has been evaluated from H_α and H_β Stark broadening and from continuum.

In a similar manner, for in Air fluxes the vibrational temperature can be evaluated by means the Boltzmann plot of the Second Positive System of the N2 molecule.

At the nozzle exit, pressure and temperature are quite low, and the plasma develops a strong non equilibrium behaviour. Most notably, the electron distribution function develops a strong non-maxwellian behaviour. Thus, the measurements obtained by means of emission spectroscopy are hardly interpretable and necessitate a plasma kinetic modelling.

Consequently, microwave absorption diagnostic technique, as it shows a very weak dependence to electron energy distribution, has been adopted to measure the electron number density at the exit of the nozzle.

5.2.1 Spectroscopic Diagnostic

Emission spectroscopy is probably one of the most common diagnostics used for plasma characterization because of its complete non-intrusiveness and the possibility to evaluate several plasma parameters like chemical composition, electron number density and electron, vibrational and rotational temperatures. Drawbacks of this technique are mostly due to the difficulties that can arise into the interpretation of spectra and in thermodynamic equilibrium assumptions which may be hardly accomplished in some kind of plasmas.

One of the most useful tools for temperature evaluation is the so called Boltzmann plot. This plot is based on intensity measurements of the emitted spectra.

The radiation intensity of a generic discrete emission line I_u is in fact proportional to the spontaneous emission probability $A^{u\rightarrow l}$ and to the population density of the upper level of the transition n_u. If the particle densities are distributed over the energy levels with Boltzmann distribution, then the following relation holds:

$$y_u = \ln\left(\frac{I_u \lambda_u}{A^{u\rightarrow l} g_u}\right) = C - \frac{E_u}{kT_e} \tag{5.3}$$

where g_u and E_u are respectively the statistical weight and the energy of the upper level, λ_u is the wavelength of the emitted photon, k the Boltzmann constant and T_e is the electron temperature.

Each equation of (5.3) represents a point (E_u,y_u) in a semi-logarithm plot, the so called Boltzmann plot. The constant C takes into account constant quantities when element and ionization stage are chosen. In this way, the slope of the line fitting the data points, obtained plotting several emission lines of the same element and same ionization stage, is proportional to the inverse of the electron temperature. If the points are perfectly aligned, the plasma is in partially local thermodynamic equilibrium (pLTE). Deviations from this equilibrium condition are reflected in the Boltzmann plot by a scattering of the points.

Also continuum emission intensity, due to recombination and Bremsstrahlung, is related to the electron temperature and a Boltzmann plot can be realized in this case too ([1], [9]).

A Boltzmann plot can be also obtained from the ratio of line to continuum intensities, but working with integrals line profiles instead of pure intensities. Also in this case the only unknown is the electron temperature.

Some limitations on the use of the Boltzmann plot derive essentially from the assumption of pLTE for upper levels (that can be a strong assumption in some plasmas) and uncertainties in the values of the spontaneous emission probability coefficients.

The light has been collected by means of a collimating lens positioned over a region of plasma formation (Figure 5.6). The lens has a focal ratio equal to f4, with a focal length in the order of 40[mm].

The signal, trough out a 600[μm] fiber optic, has been delivered to the entrance of the spectrograph.

The spectrograph was a Jobin-Yvon HR-460 monochromator, with a focal length of 460[mm] and a focal ratio of f 5.3.

The monochromator's exit was coupled with a fast shutter PCO CCD camera, with a SVGA resolution and a pixel size of 6x6[μm]. The peak quantum efficiency of this camera is in the order of 55% at 380[nm]. The grating used was a JY holographic with 1200[lines=mm], in order to collect a wider spectral window. The entrance slit was settled at an intermediate position of 0.1[mm]: this allows to obtain the best union between resolution and intensity of the spectral peaks.

The spectrograph was then calibrated both with a Mercury-Argon and a Deuterium-Halogen lamps.

The monochromator, the CCD camera and all the spectral collected data, have been controlled by means of a LabVIEW program.

The signal detected was not so intense so the CCD camera has been set at the maximum exposure time (10[ms]) and several spectra have been acquired and averaged at each condition, in order to gain a better signal to noise ratio.

All the electrical and fluid-dynamic measurements have been checked and stored by means of a DL-1740 and DL-1640 Yokogawa scopes with respectively 500 and 200MS/s sample rate.

Both lenses delivered the light to the spectrograph by means of the optic fibre. For the lens inside the vacuum chamber, a vacuum chamber optic fade-through has been necessary.

The whole scheme of the diagnostic setup is sketched in Figure 5.8.

In all the conditions an holographic 1200[lines/mm] grating has been used, apart in the case of H_α and H_β emission lines in which the higher possible resolution was necessary and a 2400[lines/mm] grating was utilized.

For all the plasma conditions several spectra have been captured in order to obtain statistically significant samples (Figure 5.9).

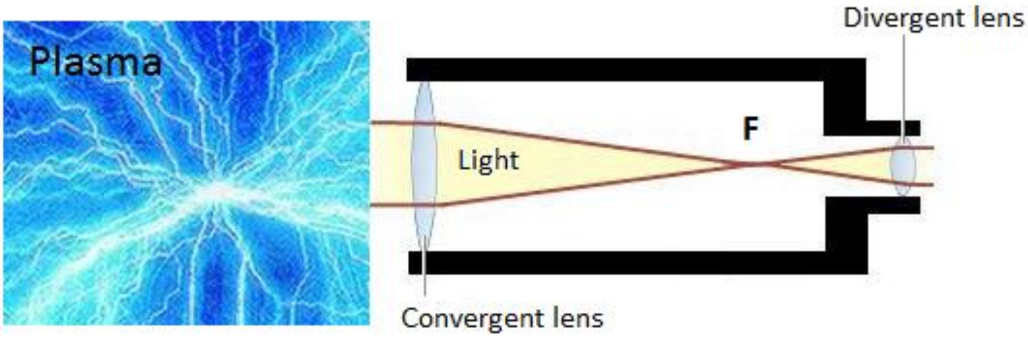

Figure 5.8 The collimating lens

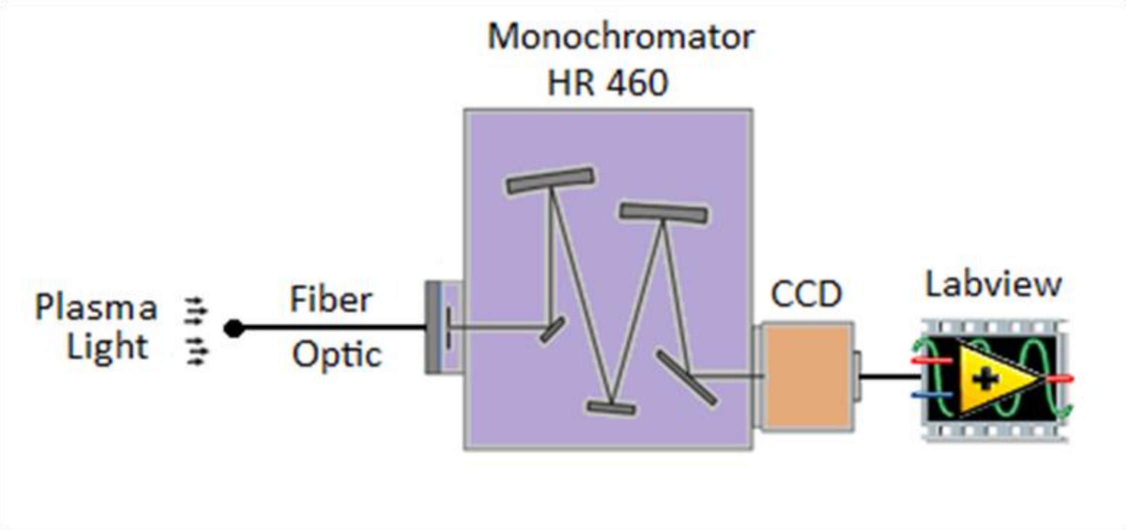

Figure 5.9 Monochromator setup

5.2.2 Microwave Diagnostic

The absorption of microwave by means of the plasma jet has been detected putting two 15[dB] horn antennas, designed for an optimal working frequency between 12 and 18[GHz], inside the vacuum vessel at the two sides of the plasma flow at about 50[mm] to the nozzle exit (Figure 5.4).

The aperture of the antenna is 76x80[mm] with a length of 160[mm].

The distance from one antenna to the other has set to 100[mm] that was the lower possible distance considering a plasma flow diameter in the order of 80[mm].

One antenna was used as source of microwave and was connected to a Gigatronics 1018-009 microwave generator, able to produce a non-modulated microwave signal from 50[MHz] to 18.5[GHz] with a power exit of 10[dBm].

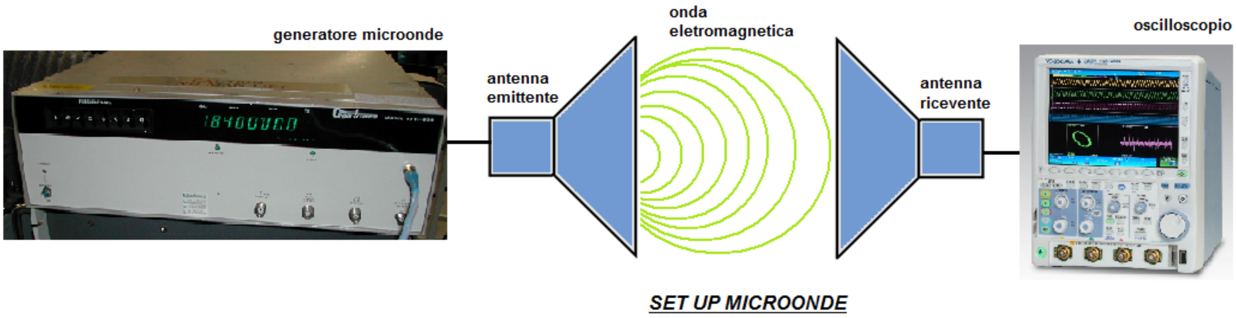

Figure 5.6 Setup microwave

The other antenna, used as a receiver, has been connected to an HP8472A crystal detector, with a pass band between 10[MHz] and 18.5[GHz]. The crystal detector signal was carried out by a BNC cable and red by a digital oscilloscope, in order to time resolve the signal. The time response of this detector is in the order of tens of nanosecond, several order of magnitude higher than the sampling frequency of the oscilloscope. In order to enhance the signal to noise ratio, at all the microwave conditions the processed transmission factor was the average of seven different signals, recorded at the same arc heater condition.

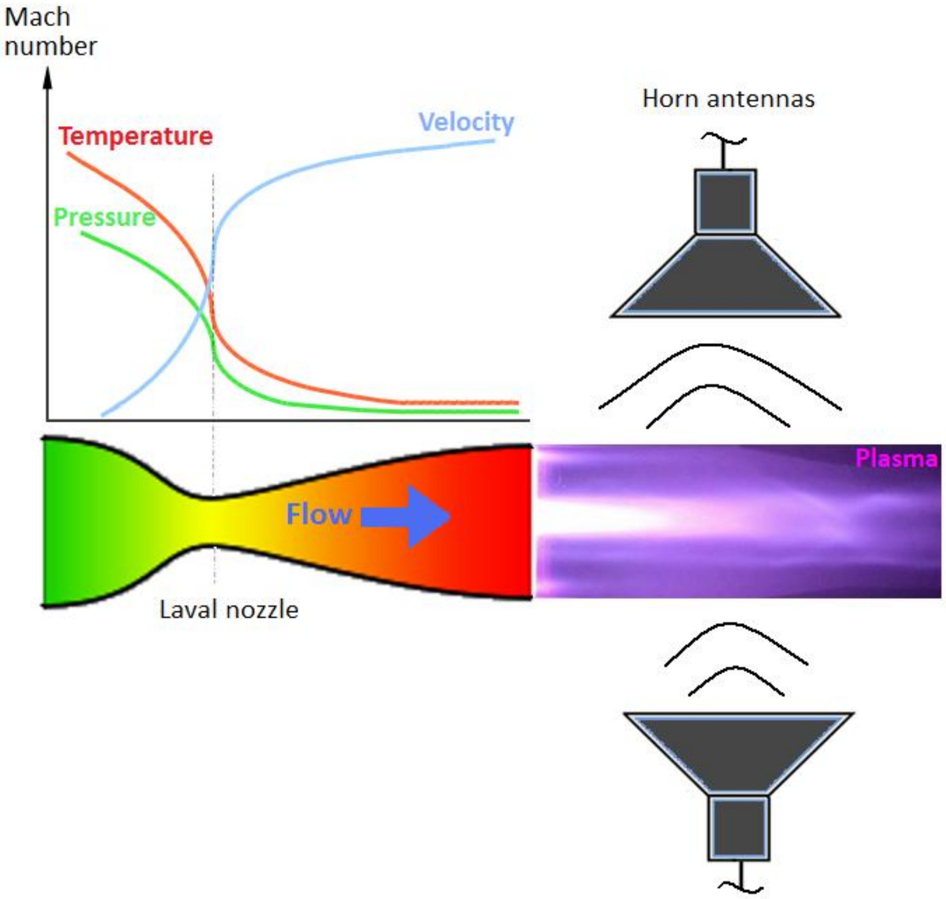

Figure5.11 Naval nozzle and the ipersonic flow

5.3 Interpretation of the results

The main targets of this campaign was:

- the determination of the non-equilibrium degree by the comparison of electron density measured before and after the expansion;
- the collection of some preliminary data to be used in the subsequent MHD test campaign.

Inside the plenum chamber electron density and electron temperature have been evaluated by means of spectroscopic measurements (the only one that are allowed).

In the free stream and microwave absorption have been used in order to estimate the electron density.

5.3.1 Argon - Mach 15

An estimation of the electron temperature is given from the analysis of the emission spectra. It was measured by discrete emission of Ar I and Ar II lines and by the continuum radiation [45]. Ar I lines seems not to be useful for any analysis, because they showed to be self-absorbed.

A typical spectra captured in the plenum chamber is showed in Figure 5.12.

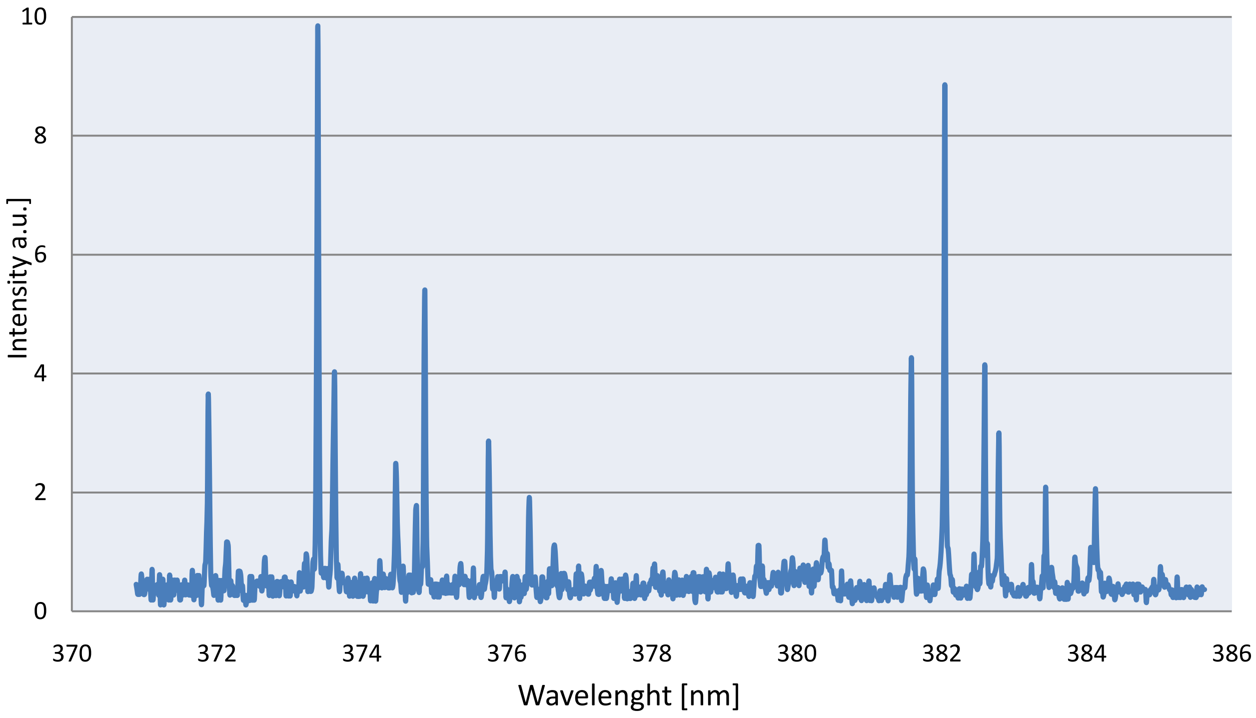

Figure 5.12 Spectra of Ar II lines

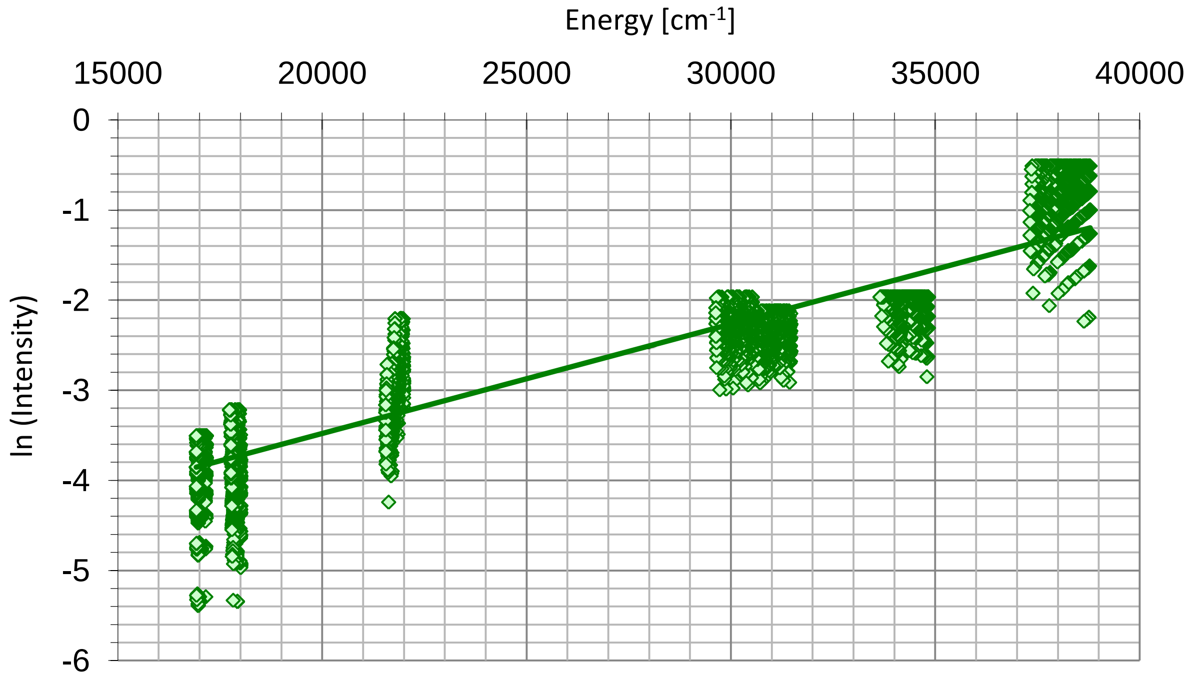

Figure 5.13 Boltzmann plot from Ar II: 360[nm]-850[nm]

Boltzmann plots from continuum Ar spectra are quite well aligned Figure 5.13, pointing out that the plasma should not be far from a pLTE (Partial-Local-Thermodynamic-Equilibrium) condition

Temperature measured by continuum is not far from the one measured by Ar II.

The values lied between 0.6 and 0.8 [eV], being the temperature higher for lower plenum chamber pressure. Also the electron number density has been evaluated by means of several methods.

One is the Stark broadening of hydrogen (always present as impurity) lines. In Figure 5.14 is showed an H_β line profile. Of the various line-broadening mechanisms those due to the Doppler effect and Stark effect have attained practical importance for plasma diagnostic. While the mechanism of Doppler broadening was readily understood, the development of an adequate Stark-broadening theory proved to be quite difficult. The shape of this profile depends on the density of charged particles surrounding the emitters: only with the recent development in computers science, it was possible to calculate a set of tables that is including both electrons and ion dynamic effects, leading to a more correct estimation of the electron number density .

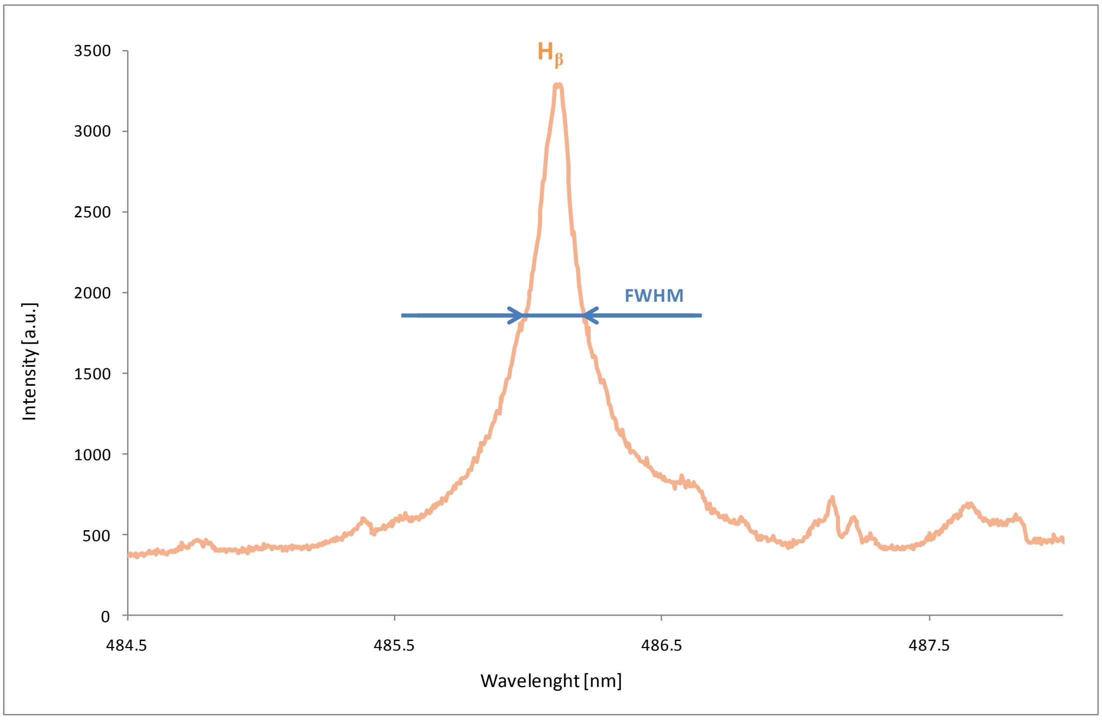

Figure 5.14 H_β line profile.

The line profiles has been de-convolved to subtract the Gaussian broadening due to the instrument and to the Doppler effect. In the working condition inside the plenum chamber, the lorentzian part of the line profile due to Stark effect is higher than the broadening due to the other mechanisms by more than an order of magnitude, allowing a precise processing of then measurements results. Various data tables are available in literature for the interpretation of hydrogen lines.

Table 2 shows some values of electron density measured in the plenum chamber at different pressure levels. It can be noted how the electron density in the present campaign is not monotonically increasing with p_{tot}: a maximum is found for total pressure around 0.8 bar. This could be explained observing that, pressure increasing has two conflicting effects: the larger density tends to raise the electron density, but on the other hand it also favours recombination. At lower pressure the first contribution is predominant, the opposite happens at high pressure.

In the end the electron number density has also been evaluated utilizing the Saha equation. The good agreement obtained validate the temperature and number density measurements.

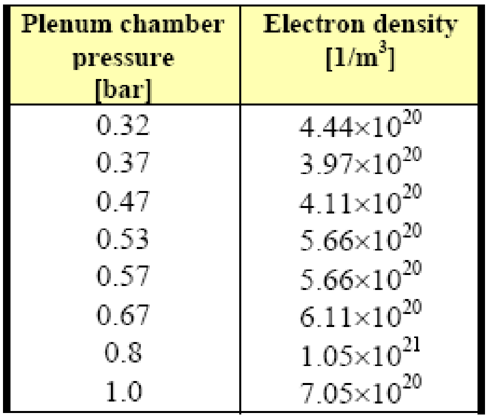

Plenum chamber pressure [bar]	Electron density [1/m^3]
0.32	4.44×10^{20}
0.37	3.97×10^{20}
0.47	4.11×10^{20}
0.53	5.66×10^{20}
0.57	5.66×10^{20}
0.67	6.11×10^{20}
0.8	1.05×10^{21}
1.0	7.05×10^{20}

Table 2 Electronic density in the plenum chamber

At the exit of the nozzle the electron number density has been evaluated by means microwave absorption. Performing these measurements in the present setup revealed to be a very challenging task because of very low density at the exit. It was observed that, for total pressure higher than 1 bar there is no significant microwave absorption by the plasma jet, at about 0.8 bar (where the electron density in the plenum reaches a maximum). In Figure 5.15 a typical variation of the electron density in function of time is reported. A stable value of electron density is not reached. This can be ascribed to arc instabilities inside the plenum chamber.

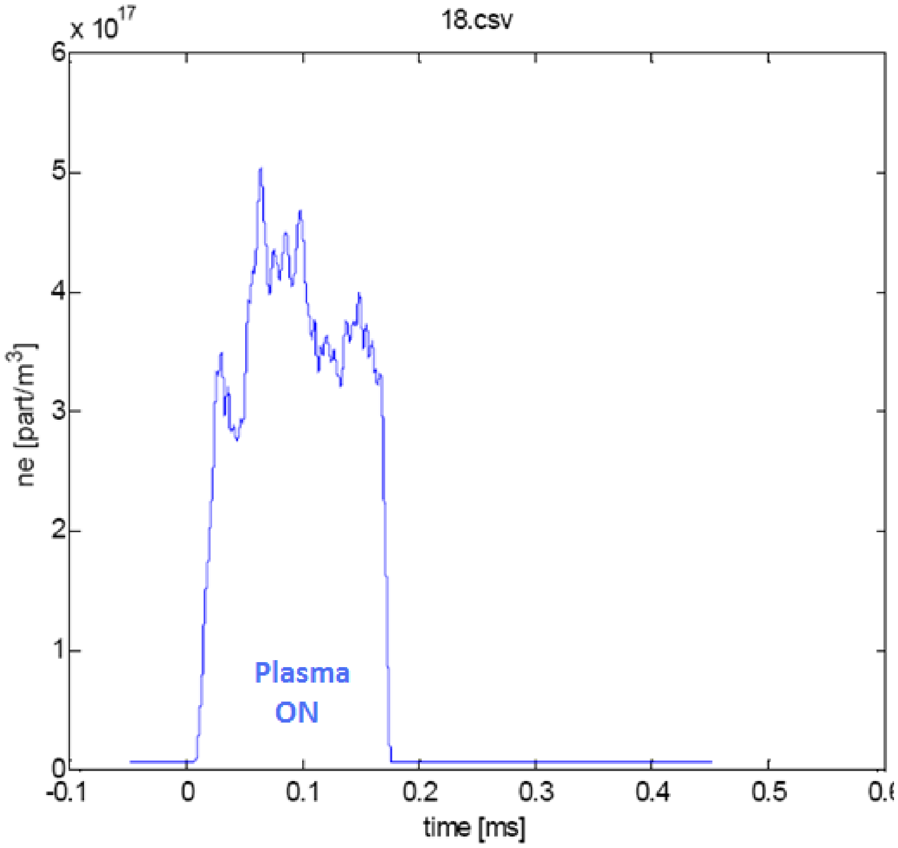

Figure 5.15 Instantaneous electron density at the nozzle exit during one run for p_{tot}=0.47bar.

For total pressure values lower than 0.8mbar, electron densities around 2-5·10^{17} m^{-3} were found, corresponding to about 67% of ionization level in the plenum chamber. It can be concluded that, like in the past, the ionization degree is practically frozen, even if to a lesser extent than in the Mach 6 case.

5.3.2 Air - Mach 9

In order to well characterize the flow before, after and during the expansion through the nozzle, the following experimental tests were carried out:

- measurements of pressure and heat flux on the nozzle internal wall;
- measurements of pressure inside plenum chamber;
- mapping of the pitot pressure at the nozzle exit;
- spectroscopic characterization of the plenum chamber.

As mentioned before, five Kulite pressure transducers and three coaxial thermocouples have been used respectively to monitor pressure and heat flux at five longitudinal stations along the nozzle wall. Both measurements presented some criticalities, in particular:

- because of the low pressure values expected, especially at the most downstream positions, a dedicated calibration of the sensors needed to be carried out in the range between 10 and 100 Pa. The calibration, done using a variable capacitance pressure transducer Setra 760 as reference, revealed a significant deviation from the nominal sensitivities declared by the manufacturer.
- due to the short duration of a single run (about 150 ms) and the resulting little wall temperature raise (less than half Celsius degree), the post-processing of the thermocouples signals required to be carried out very carefully.

In order to increase the signal-to-noise ratio a set of signal conditioning modules has been integrated in the data acquisition system of the facility.

The nominal conditions expected for this experimental campaign were p_{tot}=3 bar and h_{tot}=4.5 MJ/kg. Because it is not possible to control precisely these parameters in HEAT, due to the unpredictable behaviour of the electric arc, the strategy was to average over a great number of runs. For this campaign more than thirty runs have been carried out.

The spectroscopic characterization of the plenum chamber conditions has been carried out by our Plasma Laboratory, Department of Electrical Engineering of University of Bologna. In particular, two parameters have been studied: electron temperature and vibrational temperature. In Figure 5.16 we have reported a spectra emission in the range 649-663 [nm] where follow the lines of Iron I and Tungsten I.

The spectra are almost completely dominated by atomic emissions of the metallic particle present in the plenum chamber because of the erosion of the electrodes.

Electron temperature was estimated studying the emissions due to de-excitation of Iron I atoms at wavelengths 650 – 665[nm] by means the Boltzmann plot. (Figure 5.17). The Iron lines are present in the flow as an impurity generated by erosion of the cathode.

With a similar procedure it is possible to obtain the vibrational temperature of the Nitrogen molecules examining the band-head peaks of the ro-vibrational emissions of the N_2 Second Positive System, but in this case the measurements were much more difficult to perform since the intensity of these emissions is very low compared to those of metallic impurities.

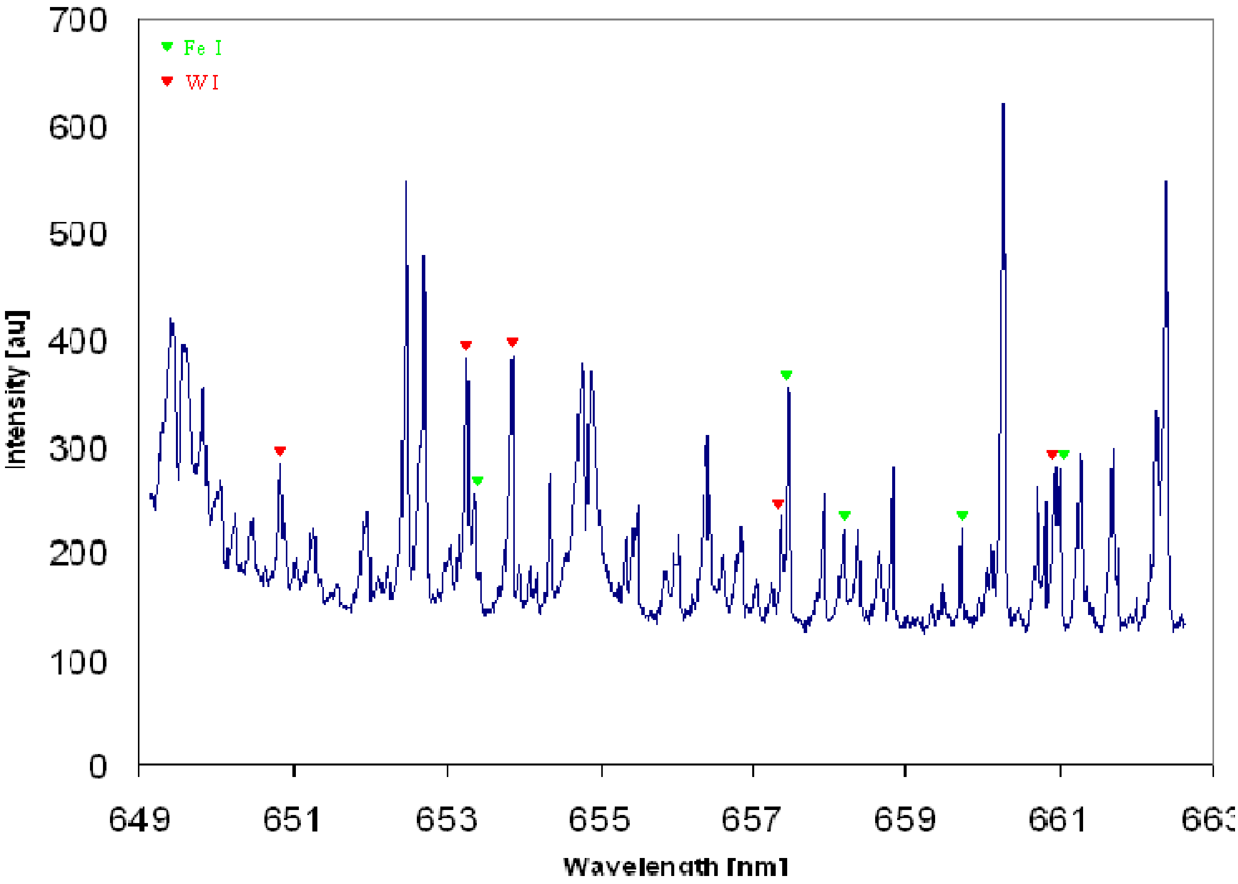

Figure 5.16 Spectra emission FeI and WI from 649[nm]-663[nm]

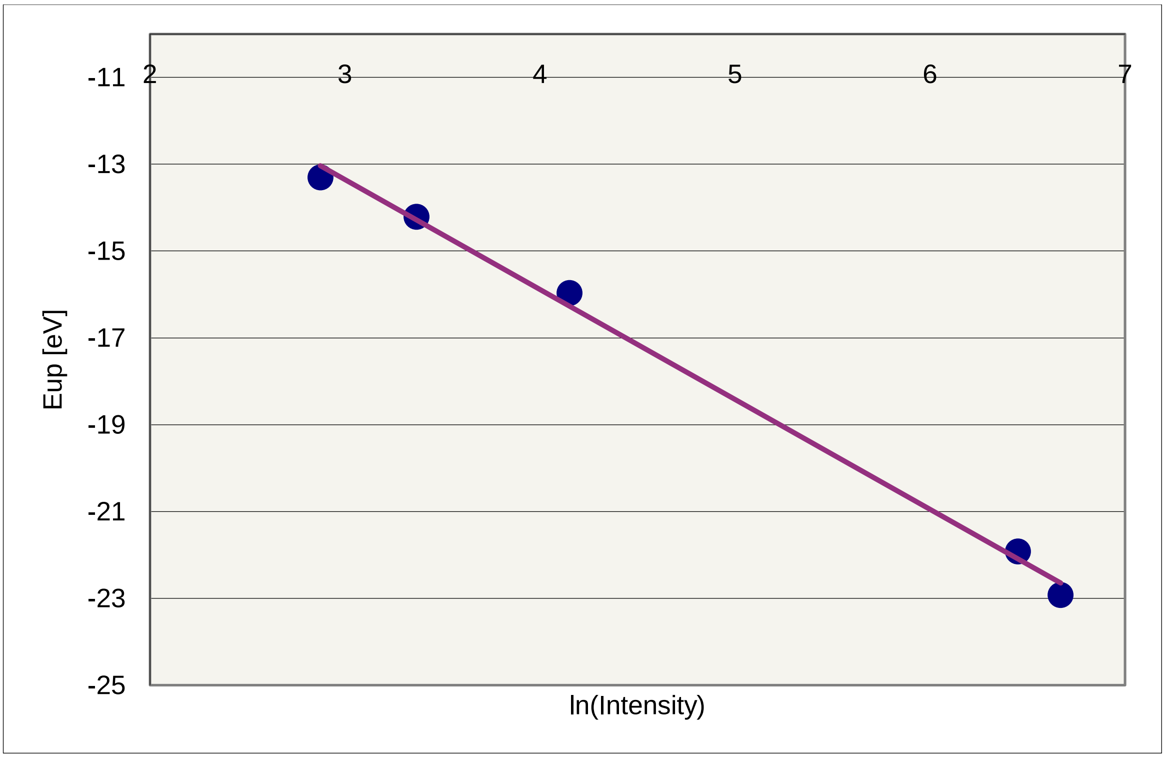

Figure 5.17 Boltzmann plot FeI

The results obtained demonstrate that, in the plenum chamber, the plasma is substantially in equilibrium since electron, vibrational and translational temperatures are in the same range (T_t=3300 K, T_v=3427 K e T_e=3660 K).

Unfortunately, in the both cases: before and after the expansion it was not possible to evaluate the electron number density.

Inside the plenum chamber no hydrogen atomic line has been found because in air hydrogen easily recombine with other molecules.

In the air plasma jet, despite in Argon flows, the electron density was too low to allow detectable microwave absorption, thus the microwave beam pass unperturbed throughout the plasma. We could only state that the electron density value was lower than $5{\cdot}10^{16}\,m^{-3}$.

Experimental results are plotted in Figure 5.18 and Figure 5.19 compared with numerical simulation performed by CIRA and Politecnico di Torino. Both simulations consider nearly nominal stagnation conditions (p_{tot}=3.17 bar and h_{tot}=4.64 MJ/kg) and a constant wall temperature of 300 K, but whereas CIRA simulation consider a fully catalytic wall, Politecnico di Torino use a noncatalytic boundary condition.

Both figures show how experimental data are in good agreement with CIRA simulation, whereas Politecnico di Torino code tends to predict a lower expansion, probably due to the different transport model used. Instead, a very poor agreement is found in the heat flux data, where CFD simulations tend to predict values well higher than the measured ones, especially in the upstream sections.

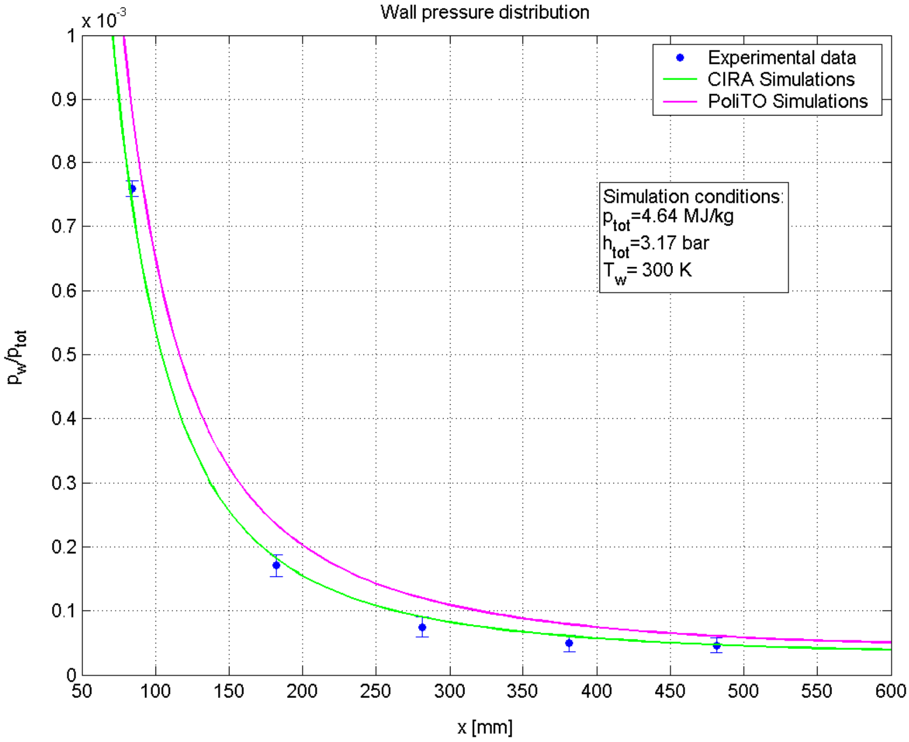

Figure 5.18 Pressure distribution on the wall

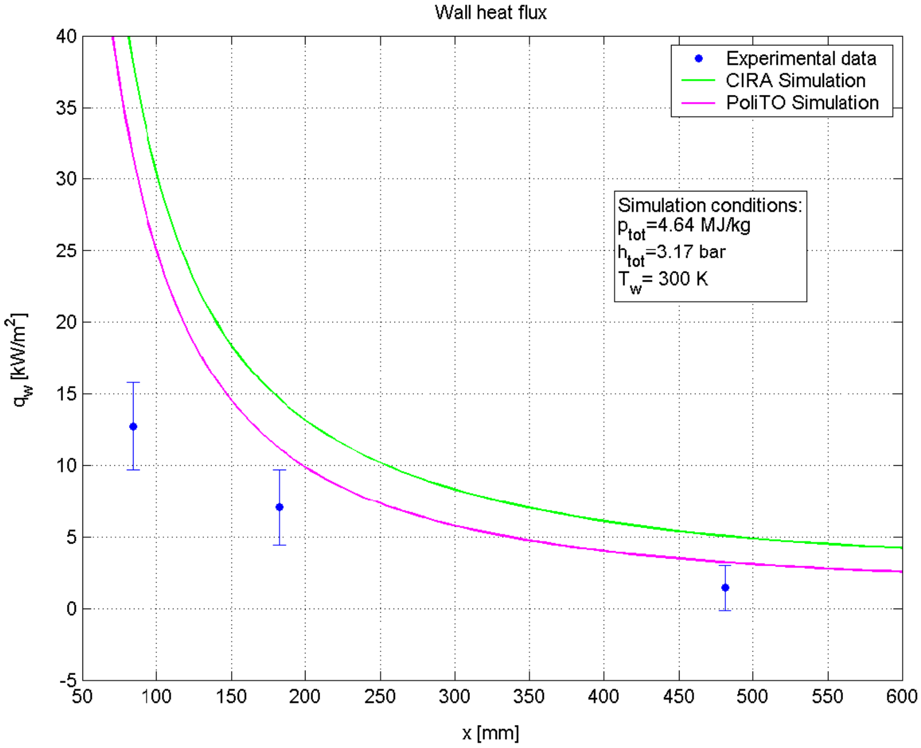

Figure 5.19 Heat flux distribution at wall

CHAPTER 6

HYPERSONIC MHD TEST BODIES

6.1 Test bodies configurations

The determination of the shape and the magnetic configuration of the test body is a crucial point. In order to simulate the re-entry of a hypersonic vehicle into the atmosphere the test body had been designed for the operation at low plasma densities.

All the fallowing experiments down here it was done in Argon gas flow. Unfortunately in the air flux, as we saw in the previous chapter, the MHD experiments was impossible to realize.

In these conditions the plasma is characterized by high values of the electron mobility and, thus, of the Hall parameter. Hence it is advisable to exploit the Hall component of the electric field (i.e. the component of the electric field parallel to the flow velocity) to sustain the current density which generates the MHD interaction.

In order to do this and to obtain a strong Lorenz force against the shock front, the Faraday current has to be as high as possible. This can be realized by means of the short circuiting of it.

The Plasma research unit of the DIE has been recently involved in an experimental investigation [10] on the MHD interaction in hypersonic regimes on a test body with an Hall electrodynamic configuration. A plane test body placed oblique against the flow and with an external magnetic field perpendicular to its surface was used. A set of electrodes parallel to the Faraday direction (the direction perpendicular to the plain containing the magnetic flux density and the flow velocity) had been placed on the test body surface to short-circuit the Faraday component of the current (Figure 6.1).

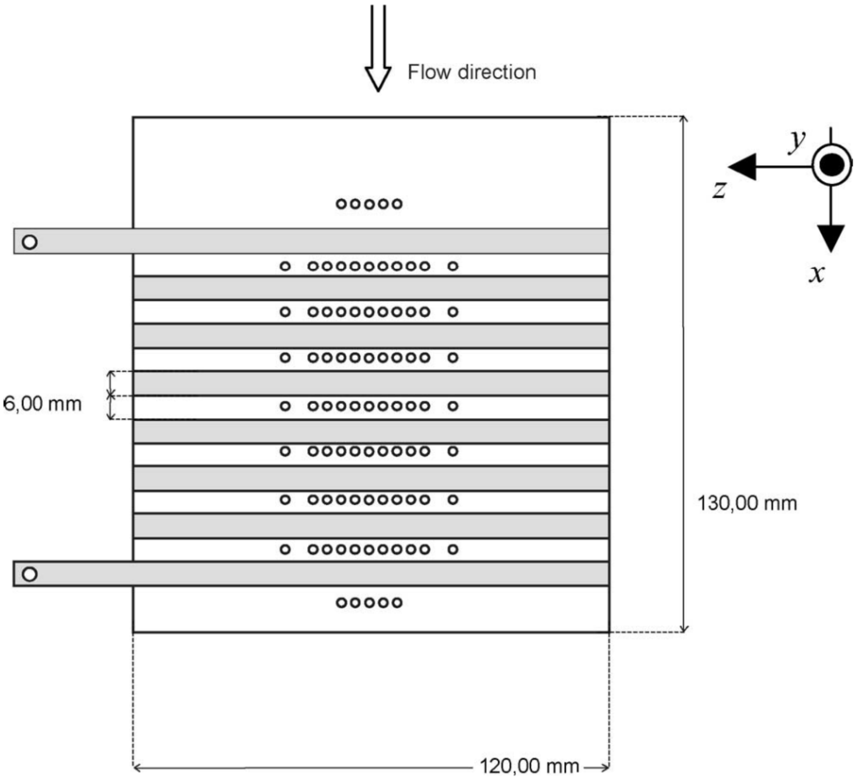

Figure 6.1 Wedge test body scheme

In this configuration the short-circuited current flowed through the plasma of the shock layer, then passed to the electrodes through the boundary layer near the walls and went again to the plasma. The measured electric potential on the test body surface revealed however that the Faraday component of the electric field was not equal to zero. Hence the short-circuiting was not realized.

The boundary layer, which is characterized by a low electrical conductivity, opposed an high electric resistance to the current owing between the test body surface and the core flow. As a consequence the short-circuiting in the Faraday direction was inhibited and the effect of the MHD interaction was reduced.

To avoid the high resistance of the plasma in the electrode region, the shorting of the Faraday current is completely realized inside the plasma by using a conical test body.

The axial symmetry of the test body allows to investigate a two dimensional geometry. The proposed design had been previously studied by means of a numerical code developed by the Bologna University team [108]. The experiments have been performed in two steps.

In the first one, a conical body with a diameter of the cone base of 60[mm] (large test body) has been utilized. During the tests the dimension of the region with a uniform hypersonic flow smaller than the dimensions of this test body has been observed.

Therefore a smaller test body with the base diameter of the cone of 40[mm] (small test body) has been constructed and tested.

Both the cones are realized with the same magnetic concept, an array of permanent magnets and ferromagnetic material (Figure 6.2). In order to keep the axial component (Hall component) of the current equal to zero, a conical electrical insulating shield of glass reinforced Nylon 6=6, with a thickness of 1[mm], is placed above the conical test body (Figure 6.3). This cover has been also useful for the limitation of the heating fluxes toward the permanent magnets that are pretty sensible to temperature increases.

Aside the magnetic cones, two non-magnetic bodies with similar geometry in compare with the magnet ones, have been realized for non-MHD tests used as “baseline" (Figure 6.4).

The use of permanent magnets was necessary because numerical simulations showed that the high magnetic field needful for the creation of the MHD interaction, if created by means of electromagnets, will lead to current densities too much high, not reproducible in our test conditions [109].

Figure 6.2 Magnetic test body

Figure 6.3 Nylon shell

Figure 6.4 Non magnetic test body

The magnets had been arranged alternating the three truncated conical permanent magnet sections with ferromagnetic ARMCO iron sections to form cone with an half-vertex angle of 22.5° and a 60[mm] base diameter. The magnetic flux density distribution has been calculated by means of a finite element magnetostatic numerical code. In Figure 6.5 the scheme of the magnetic structure with a plot of the magnetic lines is given.

In Figure 6.6 are reported the magnitude of the magnetic flux density as a function of the distance from the cone vertex along the nylon shell wall(red line), along the outer surface of the boundary layer (green line) and the shock front surface (blue line).

A comparison between magnetic field component perpendicular to the conical surface measured and calculated on the body surface (zero distance), is reported in Figure 6.7. The agreement is excellent.

All the experiments have been performed mounting the test body (the large or the small one) at one centimetre away from the exit of the nozzle with the axis of the cone in the direction of the gas flow.

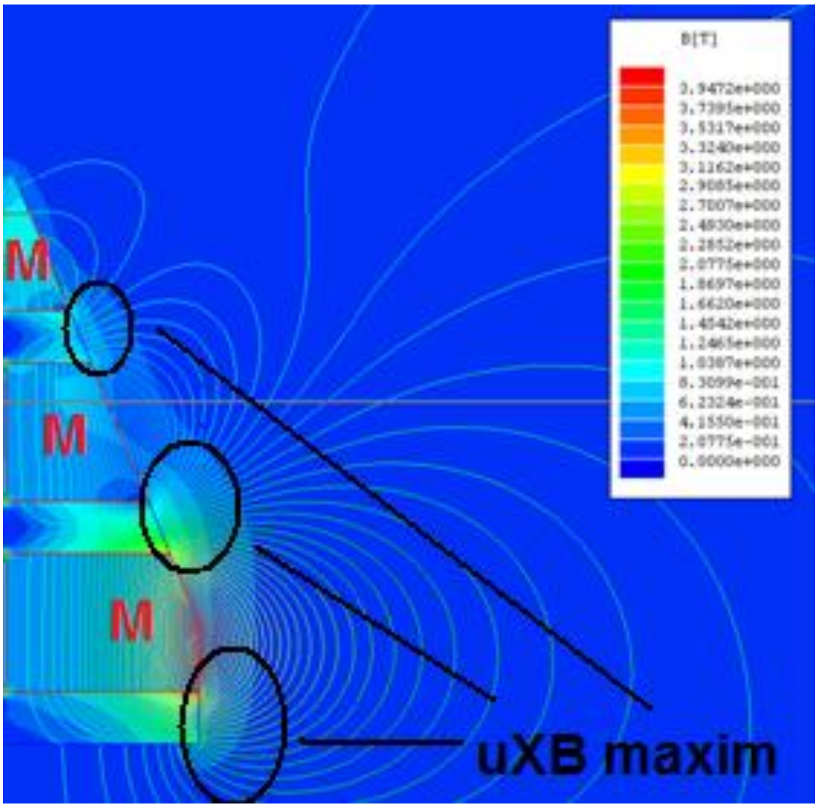

Figure 6.5 FEM analysis of the magnetic flux density around the test body

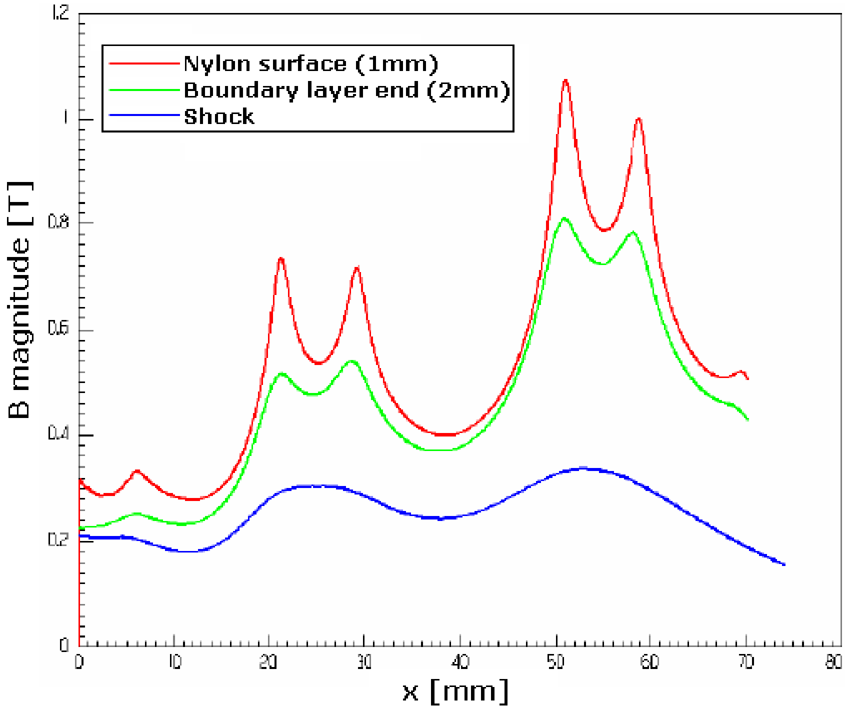

Figure 6.6 FEM Magnetic flux density magnitude

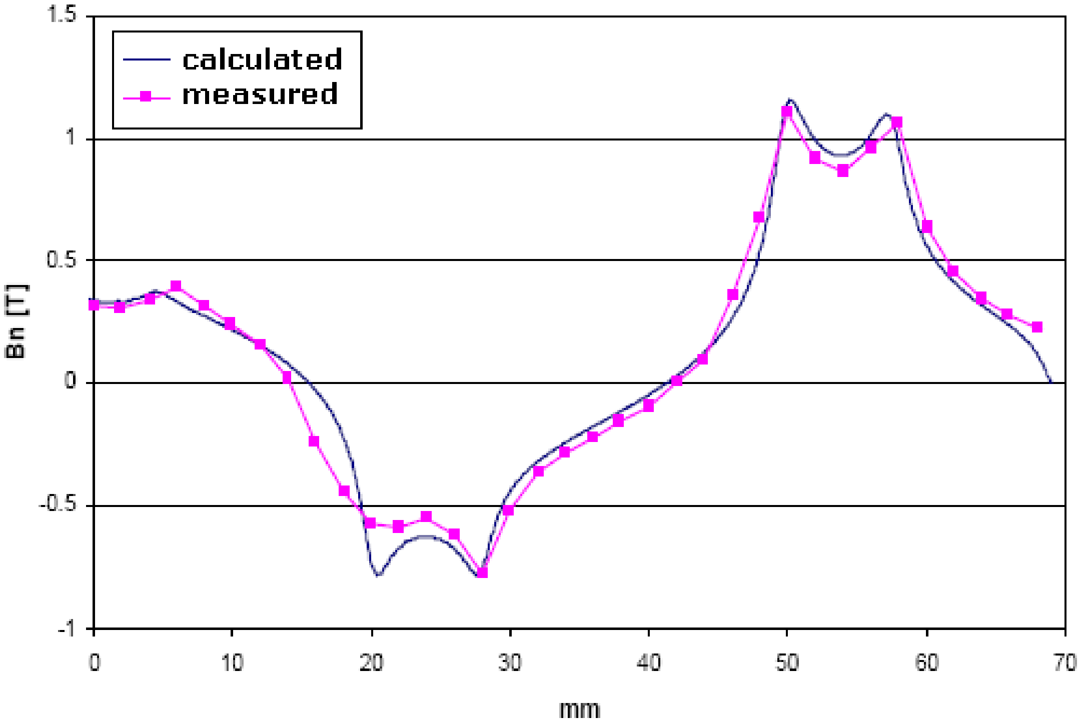

Figure 6.7 Comparison between the calculated and measured magnetic flux density along the test body wall

For both the cones, the MHD simulations predict the formation of azimuthally Faraday currents where the MHD interaction is stronger, thus where a high value of the cross product of the magnetic flux density **B** and the flow velocity **u** is expected. These regions are sketched in the left-hand side of Figure 6.8. In the right-hand side the presence of Hall currents that decrease the body force is reported.

The magnetic field needed for the MHD interaction around the blunt test body is produced by a single permanent magnet. The height, the minor and the major radius of the truncated cone are 45 mm, 96 mm and 60 mm respectively. The distribution of the magnetic flux density produced by the magnet has been calculated utilizing a FEM code and is shown in Figure 6.10. In Figure 6.11, a plot of the magnetic flux density magnitude before the small base of the truncated cone is reported. The two curves represent the B field along the radius at different distances from the base.

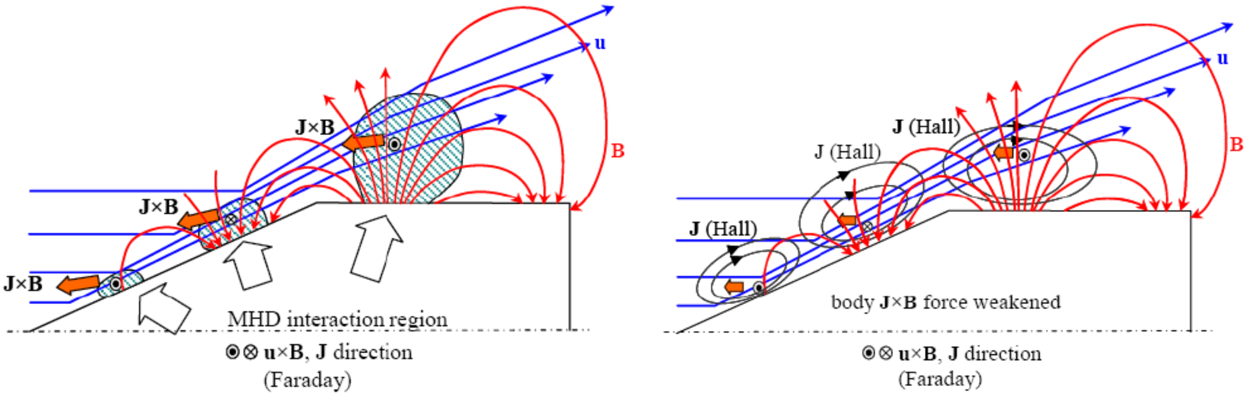

Figure 6.8 Schematic of the MHD experiment concept around

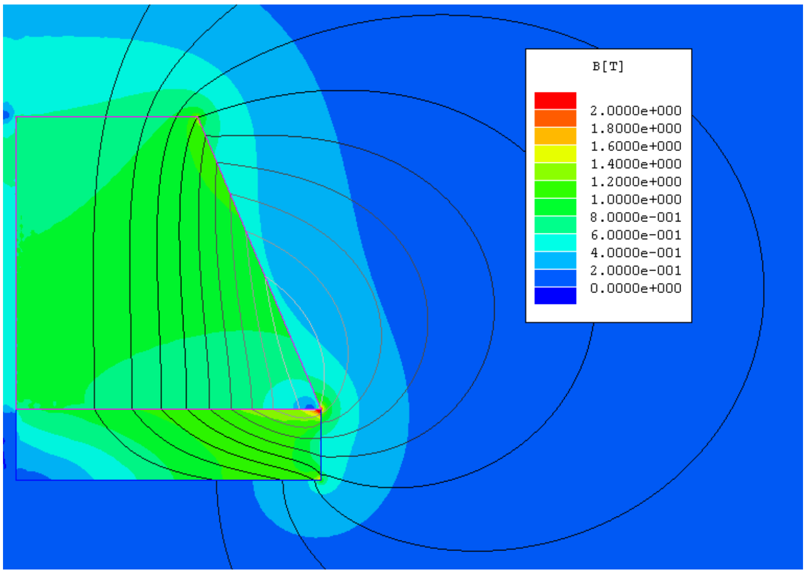

Figure 6.9 Magnetic flux density around the blunt model

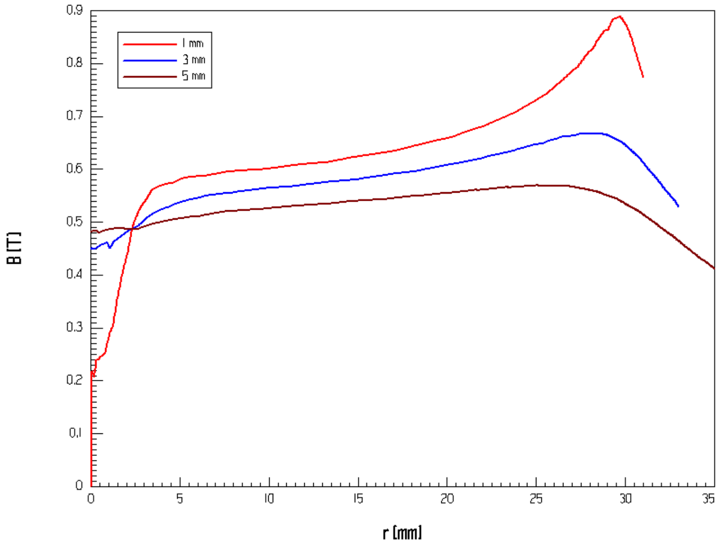

Figure 6.10 Magnetic flux density magnitude at various distances from the small base of the model

Figure 6.11 Assembled blunt test body

As in the case of the sharp test body, the magnet has been covered by a nylon 6/6 shell. The model has been equipped with a Kulite® XCS-062-5PSIA pressure sensors, located in the expansion region, in correspondence of the big base of the model. A set of electrostatic probes has been placed on the small base of the test body. A picture of the assembled test body is shown in Figure 6.12.

The electrostatic probes can be seen on the flat head of the test body. A first probe is on the axis of the model (position “1” in Figure 6.12), while other two probes are placed in along the radius of the small base (positions “2” and “3”). It should be noted that, to evaluate the effect of non uniformity in the flow, there are two “3” probes, in a diametrically opposed position.

6.2 Diagnostic setup and interpretation of the results

The presence of the MHD interaction in Argon at Mach 15 has been evaluated by means of imaging, pressure and electrical measurements.

6.2.1 Imaging setup and result

A *PCO SensiCam 1280 x1024* interline CCD color camera (Figure 6.13), with a minimum exposure time of 100[ns], has been utilized for the imaging of the MHD interacting plasma. The CCD quantum efficiency peak is nearly 53% at a wavelength of 380[nm].

The camera has been driven by means of a personal computer in order to have a complete control on the trigger.

Figure 6.12 PCO CCD camera

The pictures of the shock around the non magnetic cone and the magnetic one during a test run with a plenum chamber pressure of 0.6bar are respectively shown in Figure 6.13 and 6.14. In Figure 6.14 two brighter regions, corresponding to the zones where the MHD interaction takes place, can be recognized. The brightness of these regions can be explained, as introduced before, by the presence of an electric field u×B heating up the free electrons and causing a more intense emission. However, the pressure and thus the density of emitters is quite low, so that the MHD phenomena can be captured with some difficulties. In the experiments, when MHD interaction is present, images showed how light 'chugs' propagates longitudinally starting from the two bright rings toward the tip of the cone. A possible explanation can be found in longitudinally Hall currents that find closure paths inside the plasma. These currents are present also at Mach 6 flow conditions (Figure 6.16) but are less visible probably because the pressure inside the free stream is higher and consequently the Hall parameter is lower. Moreover the plasma flow is larger for Mach 15 run and a consistent volume of plasma exists before the shock. In this area Hall currents can easily develop a closing path.

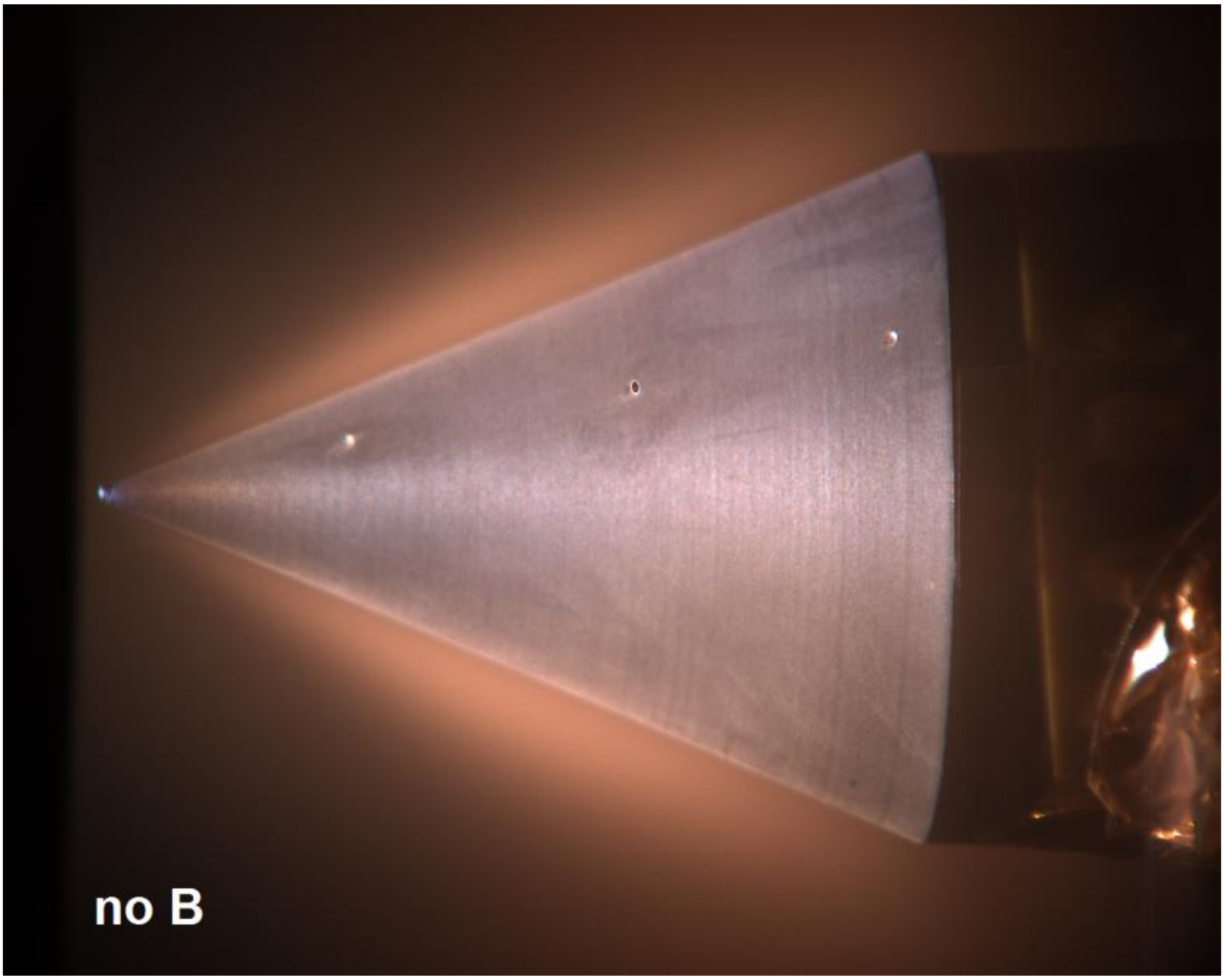

Figure 6.13 Flow around the non magnetic test body

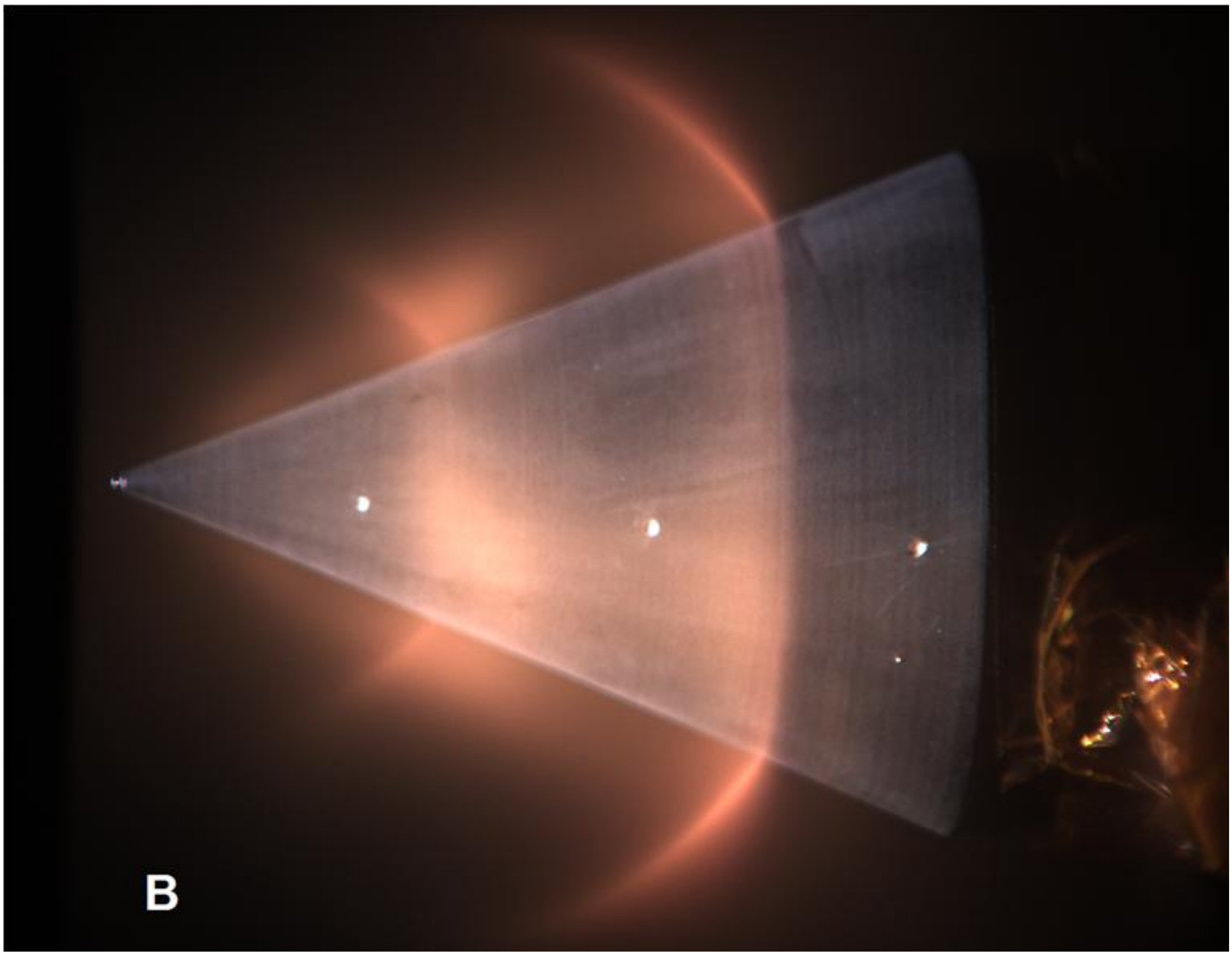

Figure 6.14 Flow around the magnetic test body

6.2.2 Pressure setup and results

In order to perform the pressure measurements, a one miniaturized Kulite fast pressure transducer (model XCS-062-5A) was mounted halfway along the lateral surface of the large test cone (Figures 6.16).

For the small test body two of these sensors have been placed, one in the middle of the lateral cone surface and the other one in the cylindrical part.

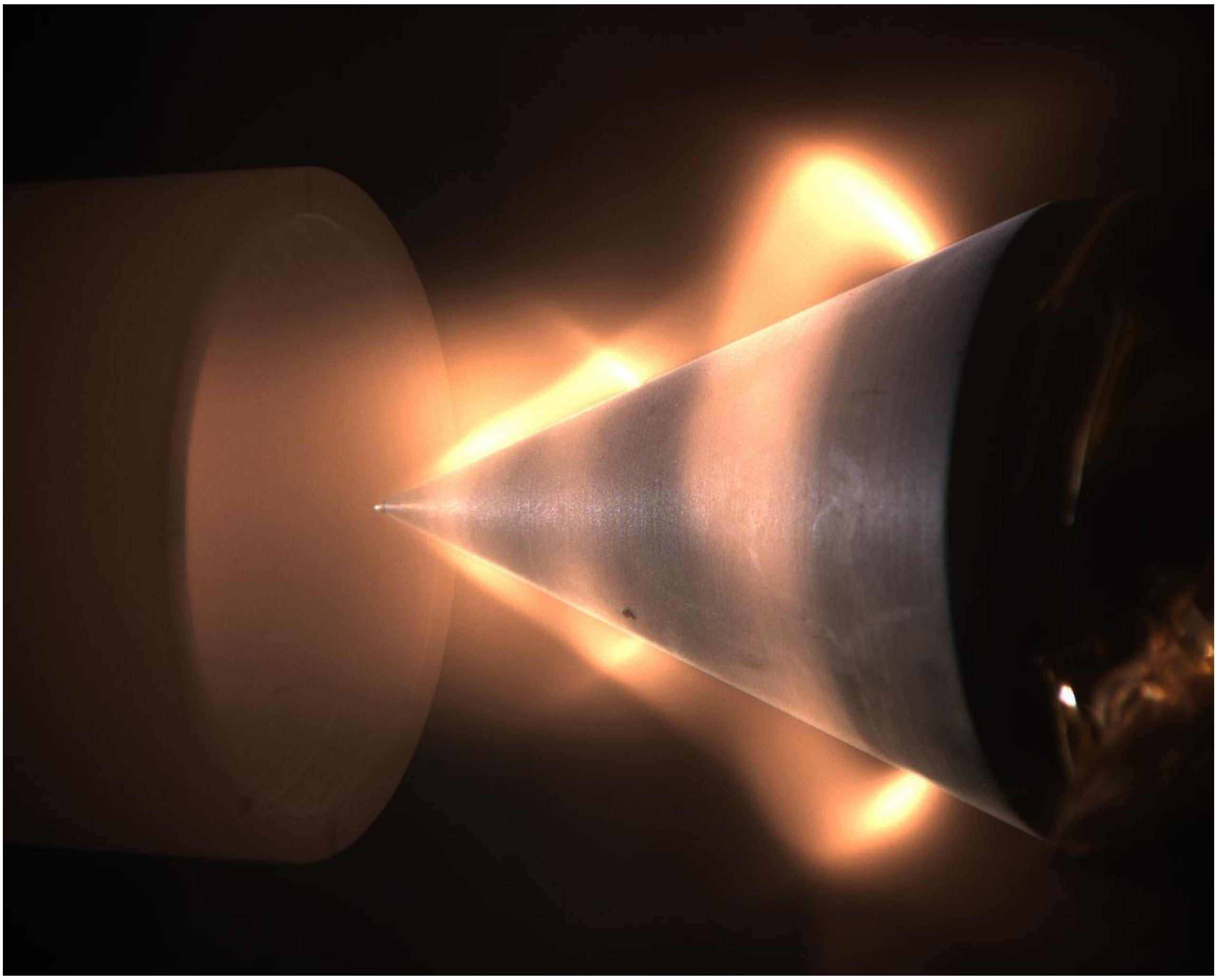

Figure 6.15 Flow around the magnetic test body at Mach 6

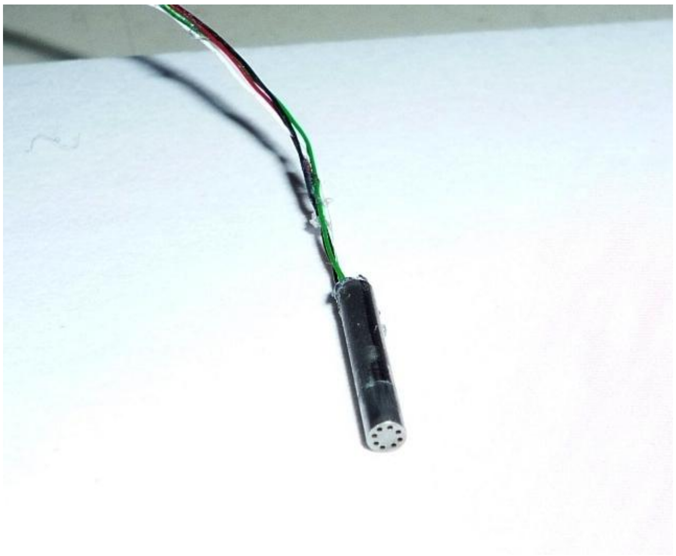

Figure 6.16 Kulite sensor and cabling

Due to the expected low level of the pressure to be measured, the signal was sent to an amplifier circuit based on the Analog Devices SSM2019 chip which allows 10, 100 and 1000 times DC gain. The signals were stored by means of a HEAT Data Acquisition (DAQ) system, which is based on the LabVIEW 7 environment and a National Instruments 6071 board.

The presence of MHD interaction demonstrated by means imaging has been furthermore evaluated using pressure transducers.

The first important task to realize is the calibration of the pressure sensor. More exactly the influence of the magnetic field, due to the presence of the permanent magnets, on pressure sensors must be checked.

This calibration had been done in the previous Mach 6 campaign and repeated in this one at Mach 15.

A series of cold runs, i.e. without arc in the heating chamber, were done with the magnetic test body and with the non-magnetic one. With cold flow, no plasma is formed and the MHD interaction is forbidden.

Measurements displayed a perfect superimposition of the two signals showing that the magnetic field has no influence in the operations of the pressure sensor.

In the Mach 6 campaign a first series of experiments have been performed when the vacuum tank was not electrically insulated. In this condition Hall currents are strongly enhanced with a consequent decrease of the Faraday currents and thus a reduction of MHD interaction performances. The plot in Figure 6.17 shows how in these conditions there are almost no differences in MHD and non-MHD runs.

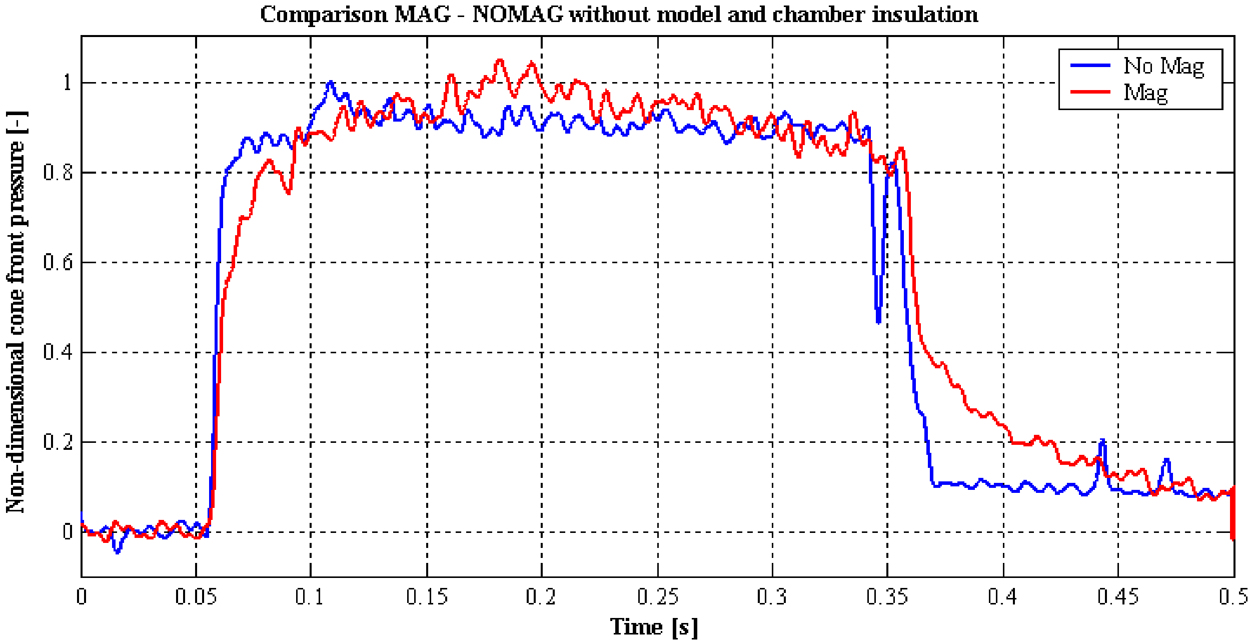

Figure 6.17 Pressure behaviors with magnetic and non-magnetic test body in a gas flow at condition 1 when the vacuum tank was not electrically insulated and the Hall field was short-circuited.

Table 6.1 Flow properties for the large cone at mach 15.

	P_tot [mbar]	H_tot [MJ/kg]	Mach [-]	p_inf [Pa]	T_inf [K]
Non magnetic Model	747	1.6	15.3	1.345	38.962
Magnetic Model	749	1.6	15.3	1.349	38.962

Table 6.2 Pressure measurements for the large cone at mach 15.

	P tip [Pa]	P back [Pa]	Cp_tip [-]	Cp_back [-]	Std P_tot [Pa]	Std p_tip [Pa]
Non magnetic	82.0	62.2	0.307	0.232	6474	42.23
Magnetic	101.0	-	0.379	-0.005	4282	51.2

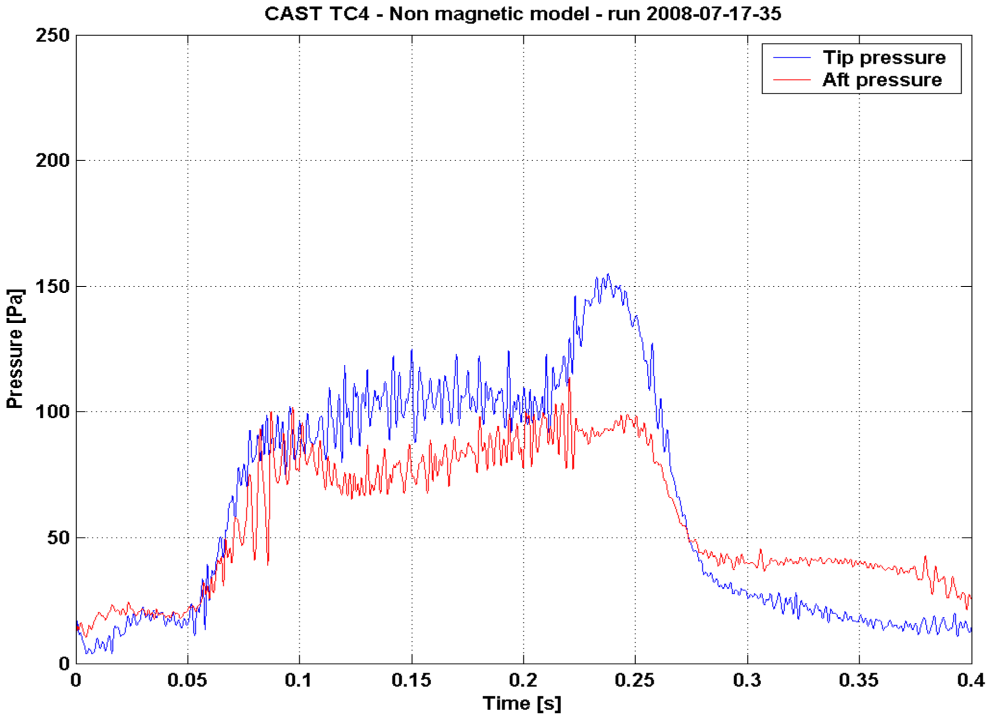

Figure 6.18 Raw pressure measurement on the non-magnetic model for one run

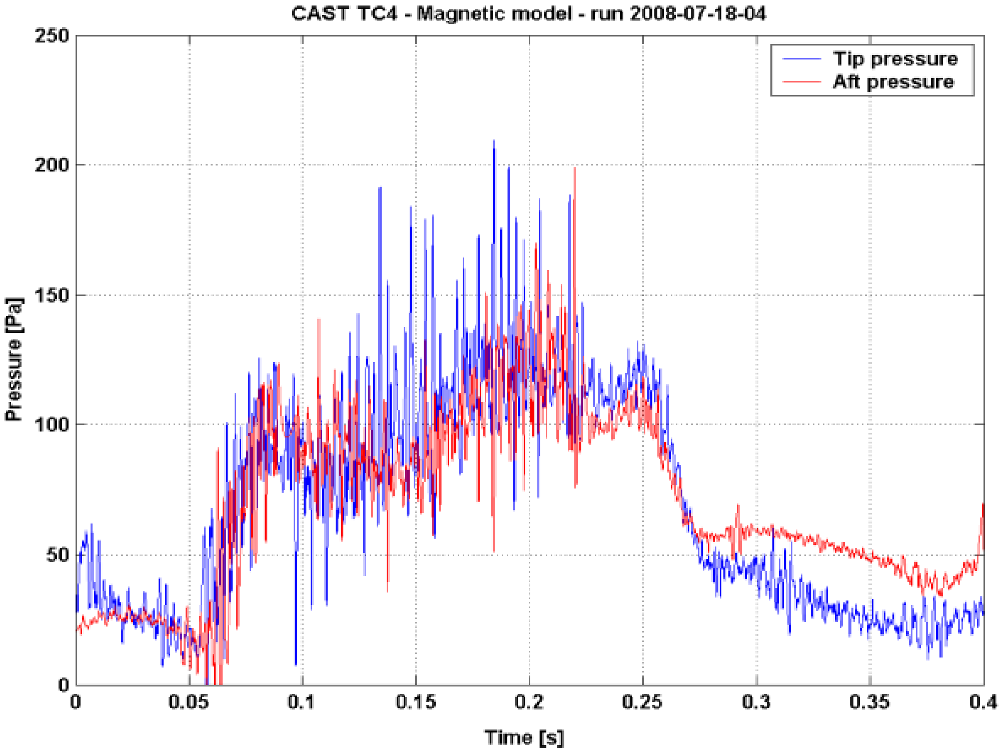

Figure 6.19 Raw pressure measurement on the magnetic model for one run

The experiments with the large cone at Mach 15 has been an attempt to extend the experience done in the previous works. The experimental activity was in the frame of The CAST project, funded by ASI. In plasma conditions a significant increase of pressure fluctuations is found for the magnetic model (Figure 6.18 and Figure 6.19). The measurements has shown a pressure increase in presence of MHD interaction. In table 6.3 and table 6.4 are reported the main flow parameters and the pressure measurements obtained for the conical test body. The aft-body sensor does not yield a clear result, while the tip sensor show a 23% pressure increase. The two column on the right in table 6 report the standard deviation for the total pressure measurements and for the tip sensor.

The pressure results for the previous Mach 6 campaign are shown in table 6.1. Particularly the summary of the test results with and without MHD interaction, pressure increases, and pressure coefficient Cp with and without MHD interaction and its increase at the three flow conditions considered in this experiment are reported. For all values given in the table, the averages between 100 and 200 ms from the flow-pulse starting time are reported.

Table 6.3 Time averages of the pressure measurements on the cone sensor at Mach 6.

Cond.	Press. No MHD [mbar]	Press. MHD [mbar]	Pressure increase [%]	Cp no MHD	Cp MHD	Cp increase [%]
1	9.01	10.34	14.78	0.344	0.390	13.44
2	10.31	11.68	13.31	0.343	0.388	13.27
3	11.77	12.97	10.16	0.343	0.366	6.88

Table 6.4 Time averages of the pressure measurements on the cylinder sensor at Mach 6.

Cond.	Press. No MHD [mbar]	Press. MHD [mbar]	Pressure increase [%]	Cp no MHD	Cp MHD	Cp increase [%]
1	1.01	1.06	5.4	0.010	0.012	10.5
2	1.26	1.34	6.5	0.014	0.017	17.6
3	1.43	1.43	~0.0	0.013	0.013	~0.0

Table 6.2 refers to the measurements done by means of the probe placed on the conical surface. An increase between 10% and nearly 15% of the pressure and an increase between 7% and 13% of pressure coefficients were observed. These confirm the results obtained in the runs with the large test body. The measurements of the pressure sensors placed on the cylindrical surface are reported in Table 4. The accuracy in this region is low due to the low values of the pressure in this location and the vicinity to the sensor minimum threshold. Nevertheless, the increases of the pressure and the pressure coefficient at conditions 1 and 2 were recorded.

These Mach 15 experiments demonstrated higher Cp increase. This behaviour can be related to the higher Mach number and the higher mobility due to the lower pressure inside the flow.

The blunt body experiment has been carried out in the frame of the CAST project, sponsored by ASI. The tests has been carried out in a Mach 15 argon flow. In tables 6.5 and 6.6 the flow properties and the pressure measurements are reported for the blunt body. In this case, a slight increase of pressure can be observed for the MHD model, giving a 13 % variation with respect to the non magnetic test body.

Table 6.5 Flow properties for the blunt body at Mach 15.

	P_tot [mbar]	H_tot [MJ/kg]	Mach [-]	p_inf [Pa]	T_inf [K]
Non magnetic Model	826	1.6	15.3	1.487	38.96
Magnetic Model	820	1.6	15.3	1.477	38.962

Table 6.6 Pressure measurements for the Blunt body at Mach 15.

	P tip [Pa]	P back [Pa]	Cp_tip [-]	Cp_back [-]	Std P_tot [Pa]	Std p_tip [Pa]
Non magnetic	23.3	28.2	0.075	0.092	3634.6	6.77
Magnetic	26.8	28.7	0.088	0.094	3572	51.2

The effects of the MHD interaction around the blunt test body at Mach 15 is shown in Figure 6.21. Also in this case, the shock appears to be considerably brighter when a magnetic field is applied (Figure 6.20).

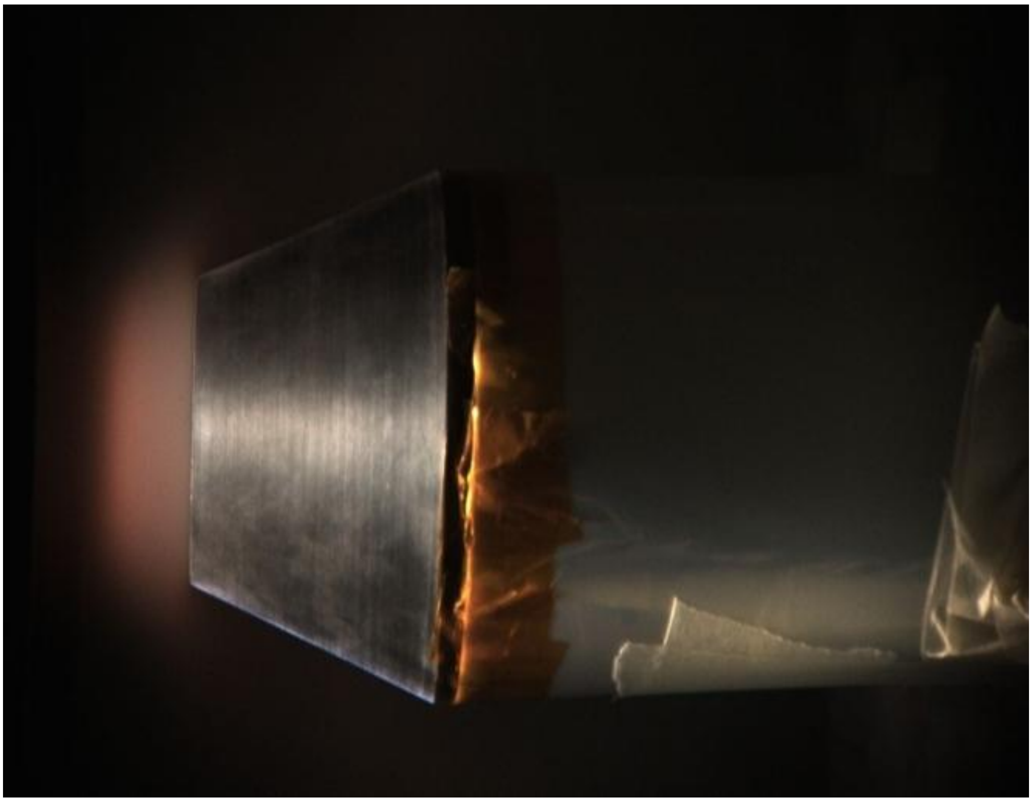

Figure 6.20 Mach 15 argon flow around the non magnetic blunt body

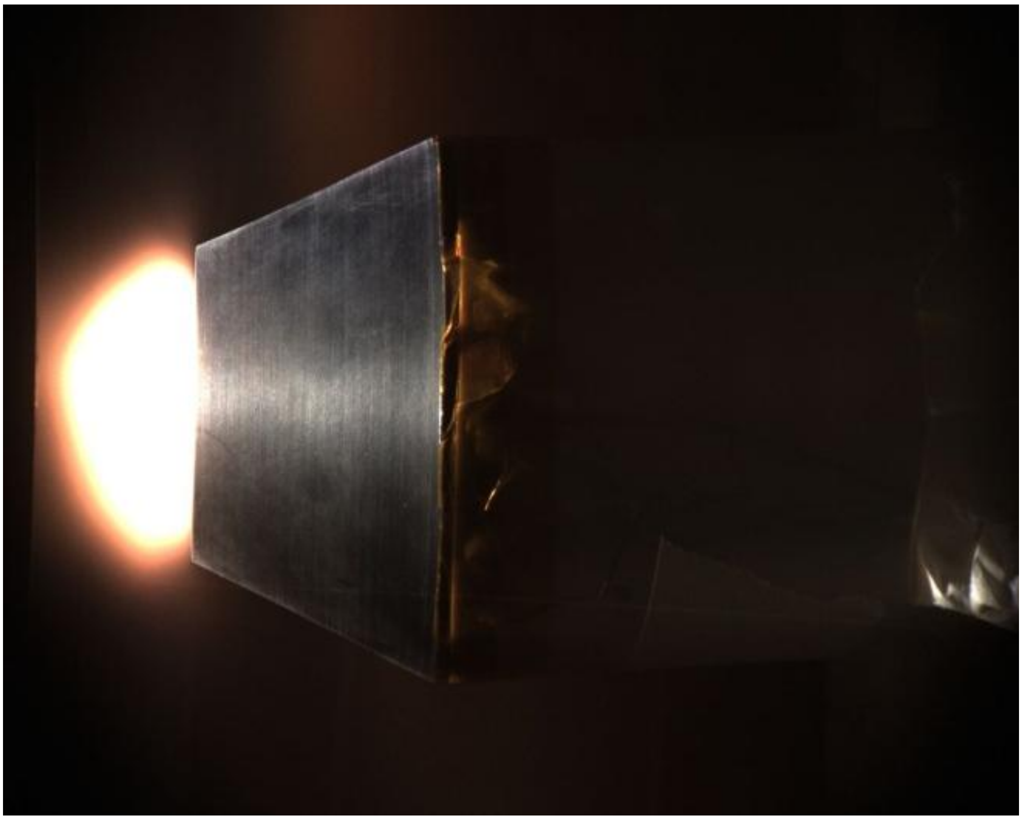

Figure 6.21 Mach 15 argon flow around the magnetic blunt body

6.2.3 Electrostatic setup and results

The presence of the Hall component of the electric field has been measured by means of a two sets of five electrical probes mounted on the shield wall as reported in Figure 6.22.

The two sets of probes have been used in order to measure the Hall potentials along two different axial direction and an evaluation of the symmetry of the flux has been allowed. The electric potential measured by the probes have been detected by means of a DL-1740 and a DL-1640 Yokogawa scopes with respectively 500 and 200MS/s sample rate.

The measurements are first run with the non magnetic cone and the data are taken as baseline signal and are subtracted from the measurements obtained with the magnetic test body.

The Hall voltages measured during the experiments at Mach 6 around the small cone at flow conditions 1, 2, and 3 and at a stagnation pressure of 0.455 mbar are shown in Figure 6.28, corresponding to the blue, green, light blue, and red lines, respectively. The dotted line indicates the Hall potential differences between the cone vertex and a position at 41 mm from the vertex and along the flow direction on the cone lateral surface. The full line corresponds to the Hall potential difference measured between the cone vertex and a probe at 17 mm from the vertex. These measurements indicate the Hall fields ranging between 400 and 500 V/m as in the case of the large test body.

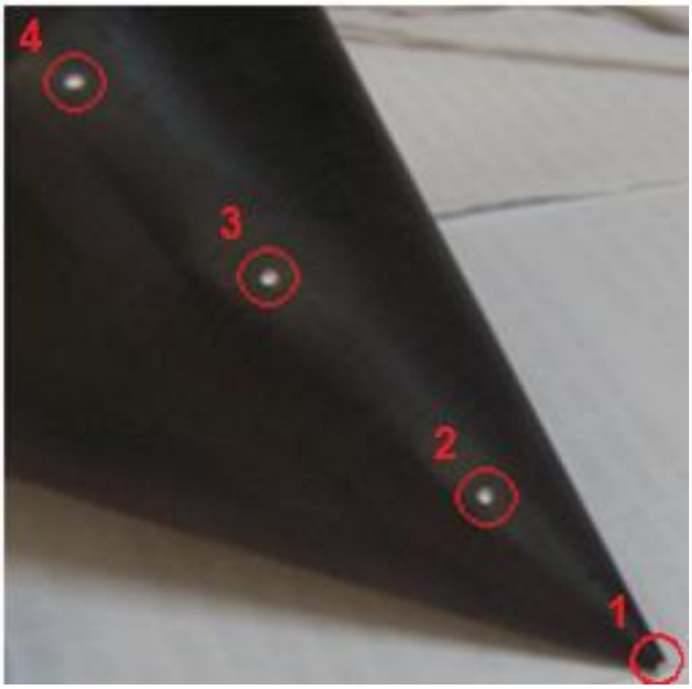

Figure 6.22 Electrostatic probes on the test body

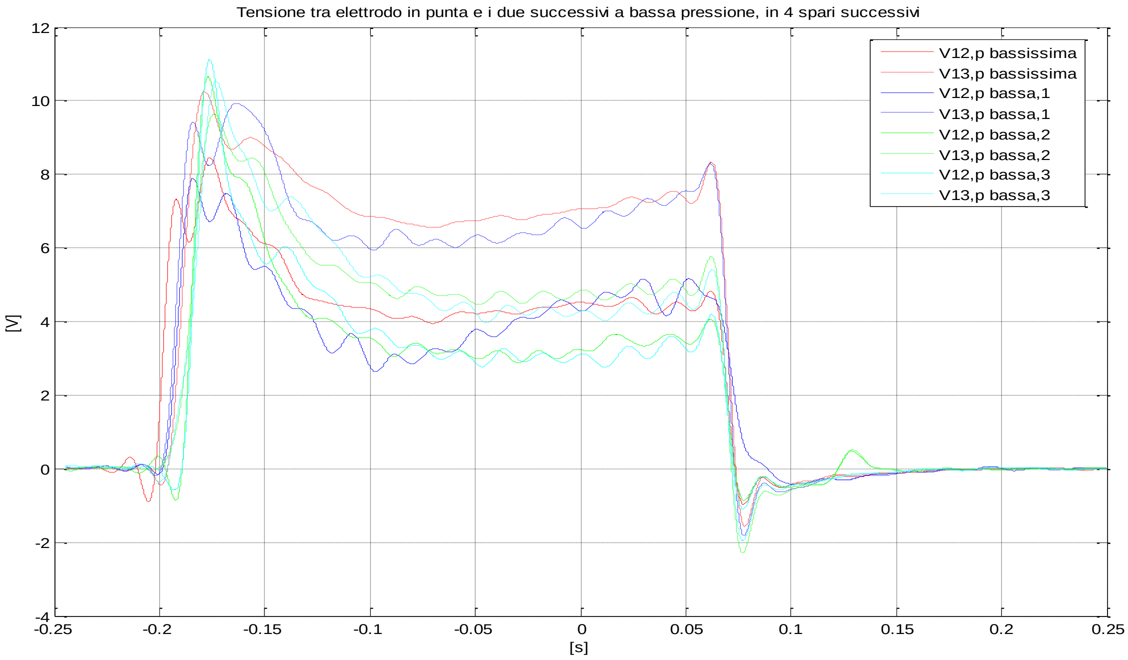

Figure 6.23 Hall voltage distribution along the test body wall (small cone at Mach 6).

In the Mach 15 campaign electrostatic probes showed different behaviours depending on the pressure condition. As reported in Figure 6.24 at low pressure, below 400mbar, a time interval where the measurement is constant cannot be clearly identified. This behaviour can be a sign that the plasma kinetics has not fully developed into a stationary phase during the experiments. Furthermore, the voltages should assume increasing values, so that $V_{21}<V_{31}<V_{41}$, as a result of the Hall electric field that is directed against the plasma flow. At low pressure we found that this trend is almost true for V_{31} and V_{41} potentials. On the contrary V_{21} was the higher value instead to be the lower one.

At higher pressure (Figure 6.25) we found a correct sequence of Hall potentials and a long plateau interval in which the measurement is constant, sign that the plasma kinetics has enough time to fully develop into a stationary state.

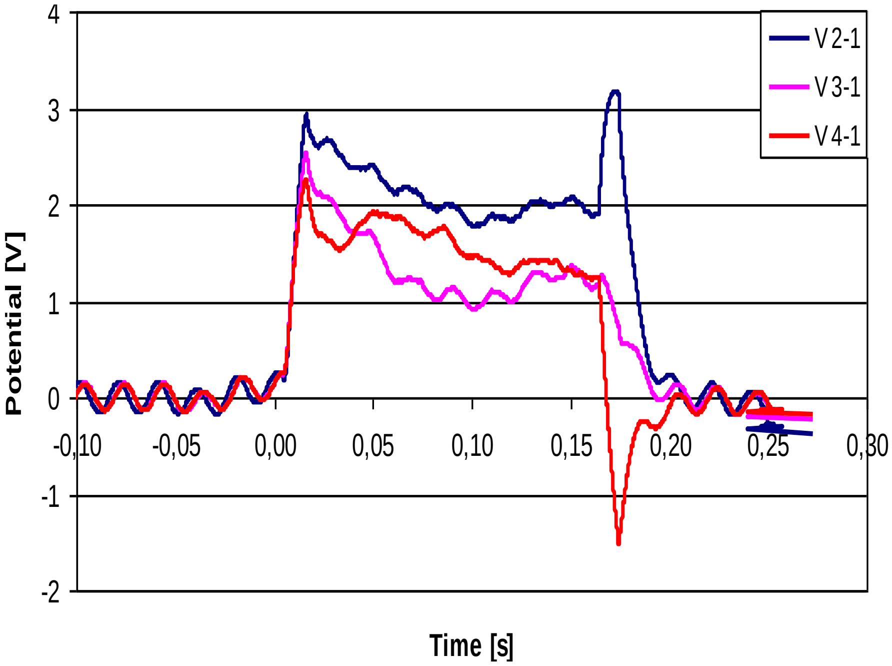

Figure 6.24. Hall voltage distribution along the test body wall (big cone at Mach 15), reservoir pressure = 400 mbar.

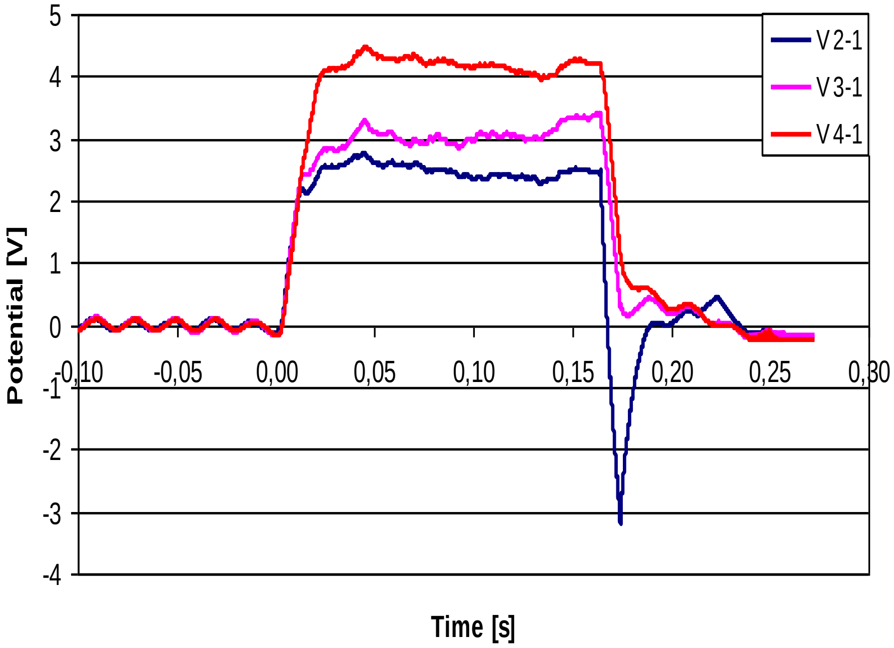

Figure 6.25 Hall voltage distribution along the test body wall (big cone at Mach 15), reservoire pressure = 750 mbar.

Hall potentials in the order of 200÷300V/m have been found. As for electron density and electron number density also this quantity is lower in compare with the Mach 6 campaign because leakage problems with the vacuum chamber and insulating problems with the test body.

The Hall field appearance has been observed on the blunt test body. In Figure 6.26, the voltage arising due to the MHD interaction on the flat base of the model exposed to the plasma flow is shown. In this case the reference probe is the one located on the axis, and the quantities V12, V13 are the voltage between the reference probe and the others as numbered in Figure 6.22. In this case, again, the voltage increases in the downstream probes (i.e. from the stagnation point to the edge of the model base).

The V13180° potential should be equal to the V13 one. Despite this, in all the runs the V13180° is higher than the V13. This result can be ascribed to an asymmetry in the plasma jet, already detected in earlier flow characterization.

A 250 V/m average Hall electric field can be evaluated. However, the Hall electric field values are observed far from the stagnation point (between electrodes 2 and 3) and assumes a value of about 400 V/m.

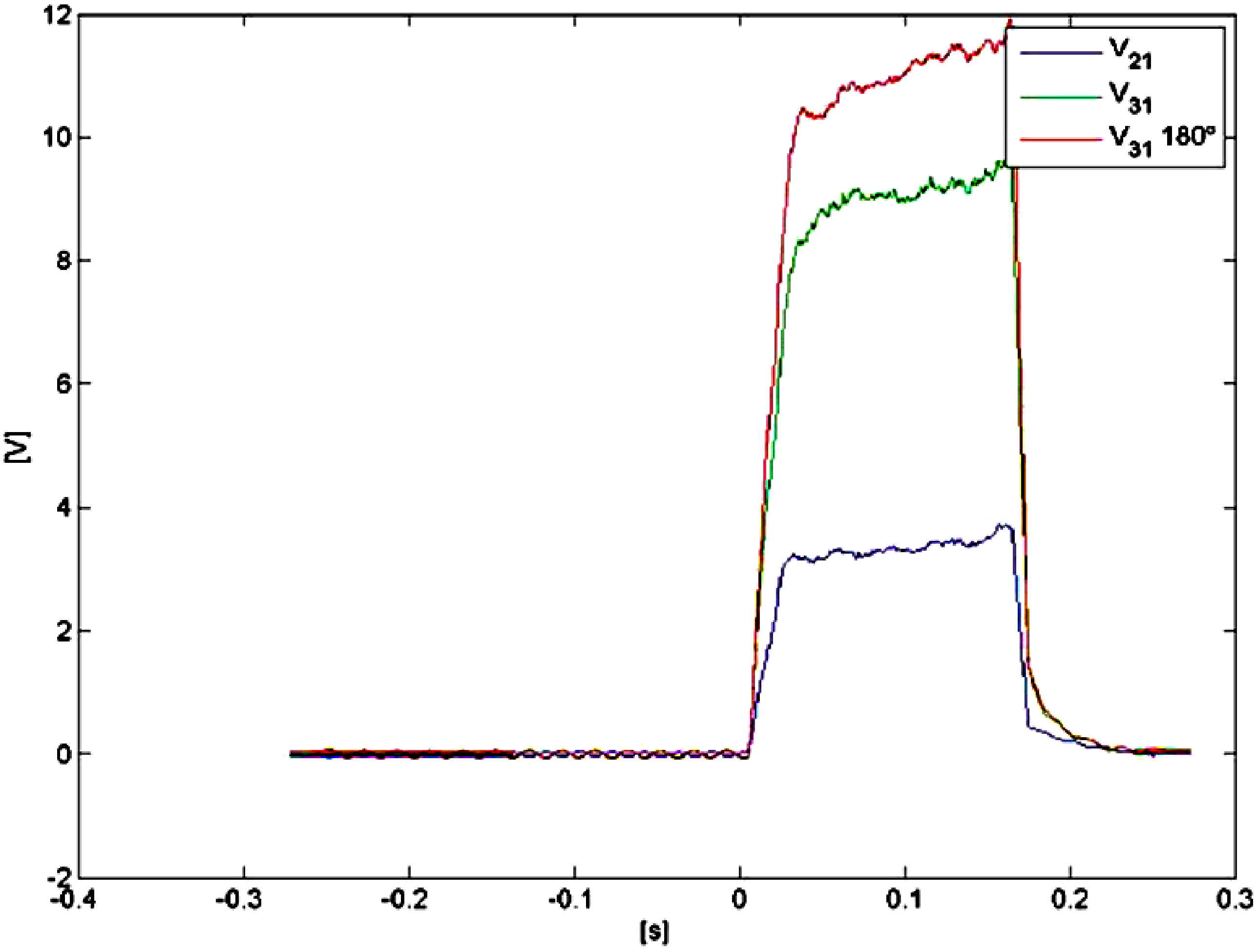

Figure 6.26 Hall voltages along the flat blunt surface exposed to the flow at Mach 15

All the diagnostics present previously was necessary for a fully characterization of the plasma involved in the MHD process and for the estimation of the effects of the electromagnetic forces on the flow surrounding the test body.

For both Mach 6 and Mach 15 experiments, it has been demonstrated that the plasma produced inside the HEAT wind tunnel is in pLTE equilibrium with a frozen ionization degree along the expansion in the nozzle. MHD tests demonstrated that bright rings are produced azimuthally around the test body in the regions where the quantity $u \times B$ is higher. Surface pressure increases around 15-20% have been measured. Hall fields in the range of $200 \div 500 V/m$ have been evaluated.

The main differences between Mach 6 and 15 experiments can be found in a worsening of the wind tunnel performances in the second campaign at Mach 15. This is reflected in a lower ionization degree, in lower Hall fields and in pressure behaviours not easy to interpret.

PART III

Langmuir Probe techniques

CHAPTER 7

A NEW DEVELOPMENT OF THE LANGMUIR PROBE APPROACH

7.1 Introduction

In plasma physics it is very important to be able to measure a variety of the plasma properties such as the electron temperature or the electron and ion density. The method of using Langmuir probes enables us to achieve the above with quite a simple process.

Like any other measurement method the Langmuir probe method has its flaws and limitations. In this experiment we tried to characterize this method in a variety of ways, tried to find its range of validity and to examine its possible extent of accuracy.

In this chapter we are trying to answer all of the above by using a set of experiments with planar and cylindrical probes and varying the conditions in which the plasma is contained. All data is obtained directly from the I-V curves measured from the probe. The collection of information was obtained in the undergraduate Plasma Laboratory, at Electrical Department.

7.2 Experimental apparatus

For the determination of the parameters it has been used a vacuum system and the working gas utilized was air and Argon. (Figure7.1)

Inside the vacuum chamber, the negative DC plasma voltage is created by two equal flat plate electrodes. Left side the cathode and at the right side the anode that is grounded, like all the metallic parts of the system.

The interspace between the electrodes is 3-4[cm], where the set of Langmuir probes are positioned in different arrangement: vertical or horizontal branches of the chamber.

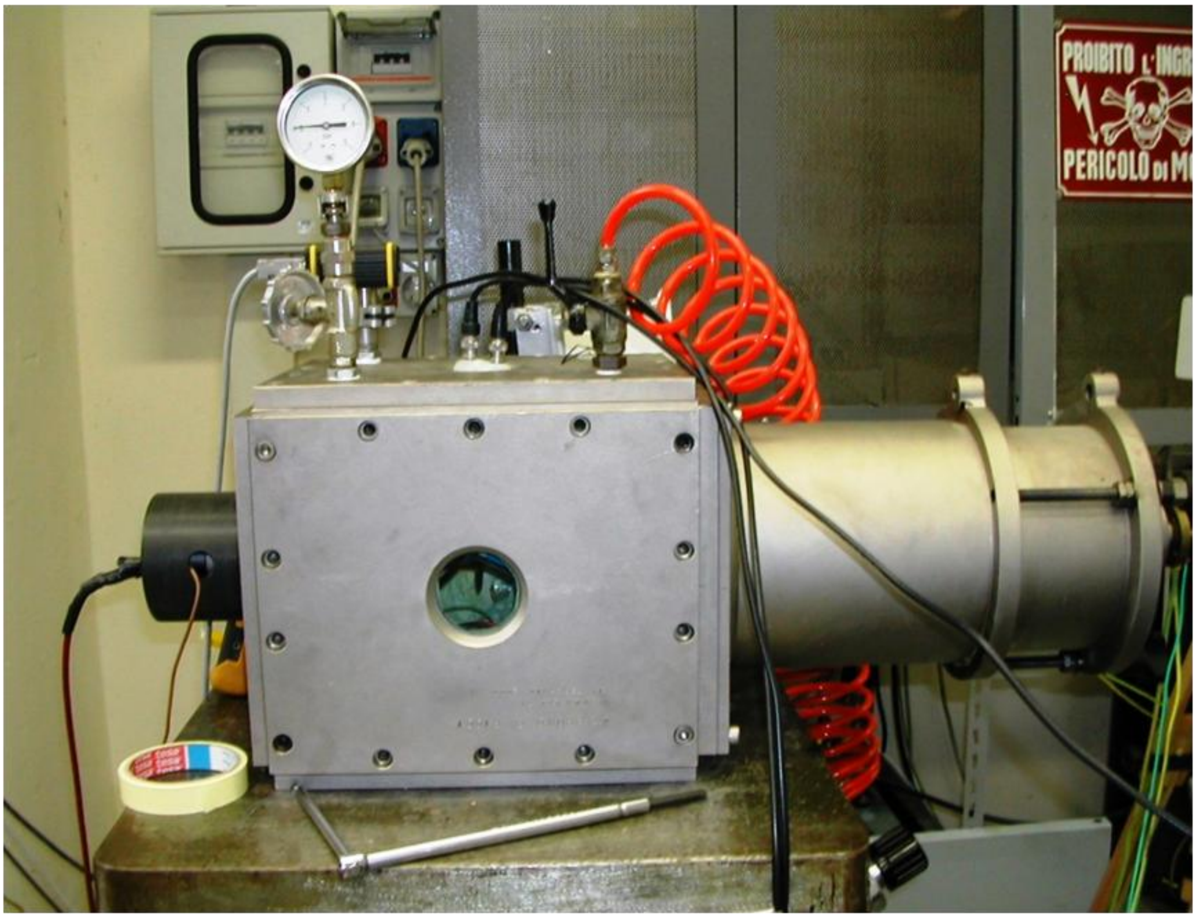

Figure 7.1 Vacuum chamber

For the realization of the vacuum it has been used a turbo pump backed by a fore pump has been used, for the pressure, a thermocouple and Baratron gauges.

In order generate the plasma, a cathode is connected to DC power supply through a 2.5kΩ Ballast resistor, to limit the current (Figure 7.2).

The signal generated by an HP Function Waveform (33120 A) is amplified by an AC Power Source (Elgar 3001) associated to a transformer (5KVA). The alternative current resulted is filtered and levelled through the Graetz bridge. Now the DC current obtained passes across 4 resistor in series ($R_1=R_2=R_3=R_4=220\Omega$; 5W), for the limitation of plasma current. And finally, here we have the high voltage. For security, in parallel of the resistances there is a discharge capacitor ($C=240\mu F$).

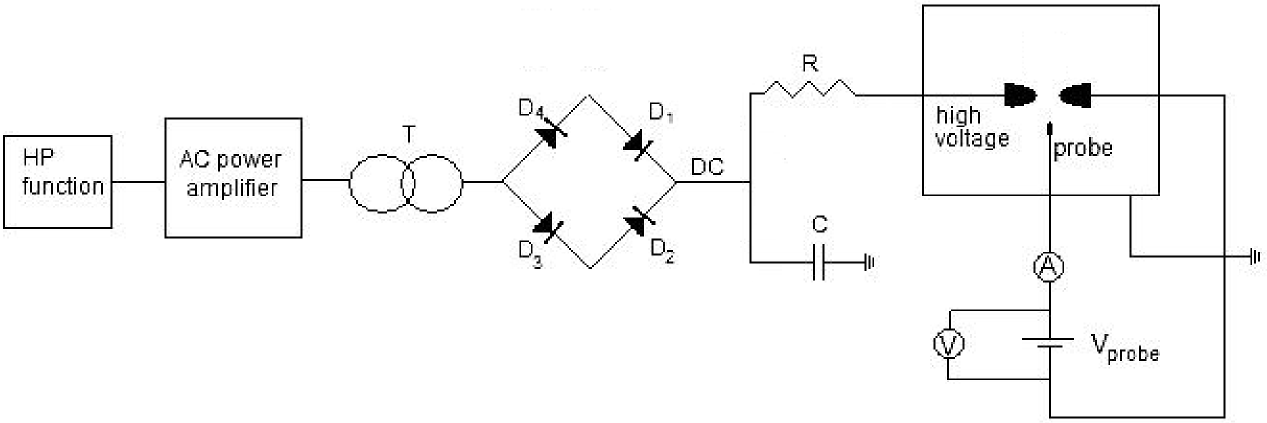

Figure 7.2 Setup of plasma generation

7.3 Planar and cylindrical probe

The Langmuir probe it was realized by copper and aluminium with different geometrical configuration (Figure 7.3).

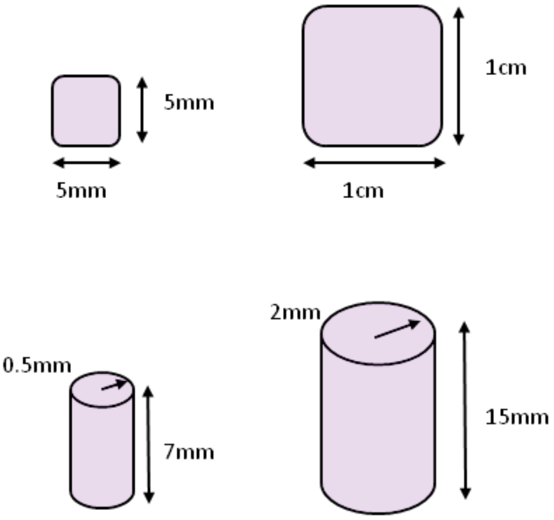

Figure 7.3 Different Langmuir probe configuration

Figure 7.4 Langmuir probe parallel (left)/perpendicular(right) configuration with/on field lines

To vary the applied voltage to the probe, it has been used an sinusoidal signal generator ± 80[V] plus an continuum one ± 40[V].

The voltage between the probe and ground is the real probe voltage and the probe current is detected by using a resistor (R=0.2 ÷ 100MΩ) plugged in series to the probe's circuit. The both signals are connected to a amplifier 8B50/51 voltage input modules. The amplifier is especially useful for the ion saturation current, cause de value is around [μA]. All dates are recorded through a Yokogawa oscilloscope 1640.

In Figure 7.5 there is the voltage probe setup

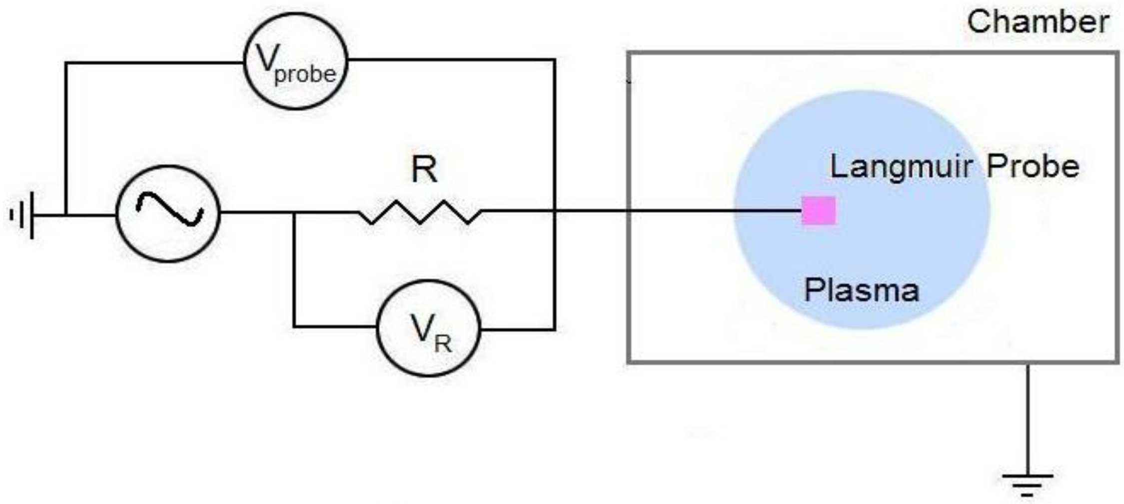

Figure 7.5 Voltage probe setup

7.4 Processing the raw data

For understand better, this is an example of a Langmuir probe analysis and the issues related to it. The data was acquired by measuring the current drawn by a Langmuir probe as the voltage applied is varied.

Figure 7.6 presents a first look at the actual IV trace. This is probe current plotted as a function of probe bias. This plot can tell us a lot about the plasma. The floating potential, V_f, occurs where $I_{probe} = 0$. In this case, appears to give $V_f \approx 40$ V. The ion saturation current, $I_{i,sat}$, is seen at biases well below V_f. The roll-off at large positive values of V_{probe} corresponds to the electron saturation current, $I_{e,sat}$. The location of this roll-off, or knee, is the plasma potential, Φ_p (in this case, our $\Phi_p \approx 80$ V). As with the floating potential, some estimate of this value may be made from the plot, but a more accurate method will be used to determine the final value.

If our x is actually $x = V_{probes} - V_f$, then the slope of this line is related to the electron temperature. The method is to plot the term $\ln|I_{probe} - I_{i,sat}|$ and then fit a line to it. The slope of this best fit is inversely proportional to the electron temperature.

It is necessary to subtract the value of the ion saturation current from I_{probe} in order to continue with the analysis. A closer look at figure 3 provides $I_{i,sat} = |-5.85 \times 10^{-6}|$ [A]. Since the $I_{i,sat}$ value is negative, subtracting it from I_{probe} will result in almost all of the values of $I_{probe} - I_{i,sat}$ being positive, because the natural logarithm of the current in the next few steps and the natural log is not defined for negative numbers.

Anyway if a few negative values left in the trace after subtracting the $I_{i,sat}$ value that is acceptable. Those values will not play a role in the temperature calculation that follows.

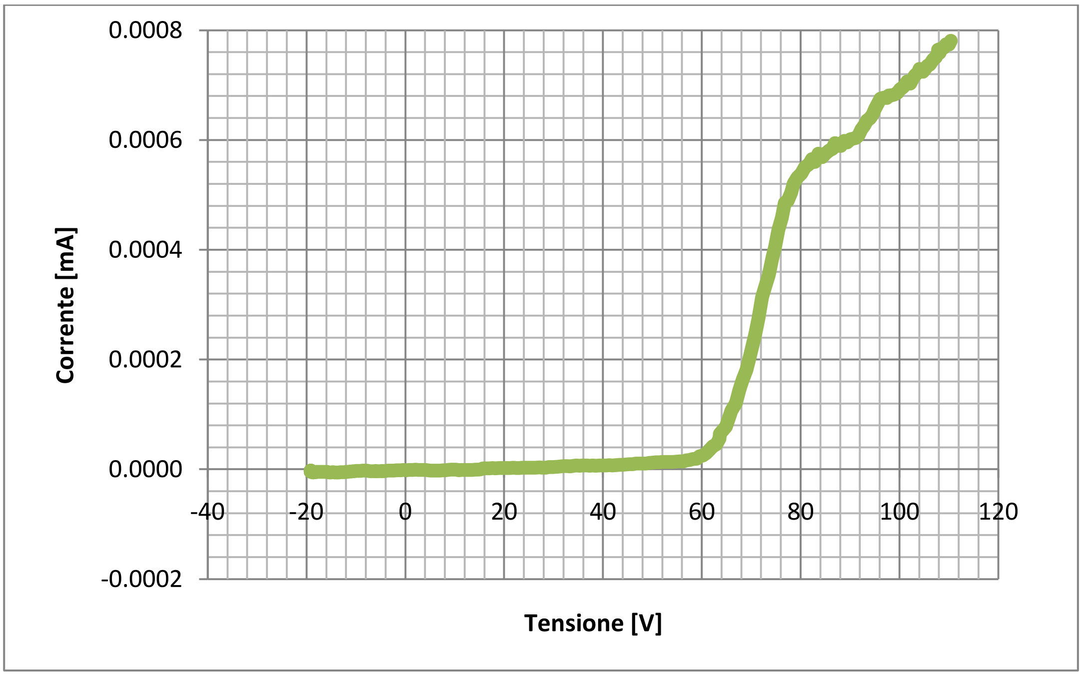

Figure 7.6 The LP characteristic obtain

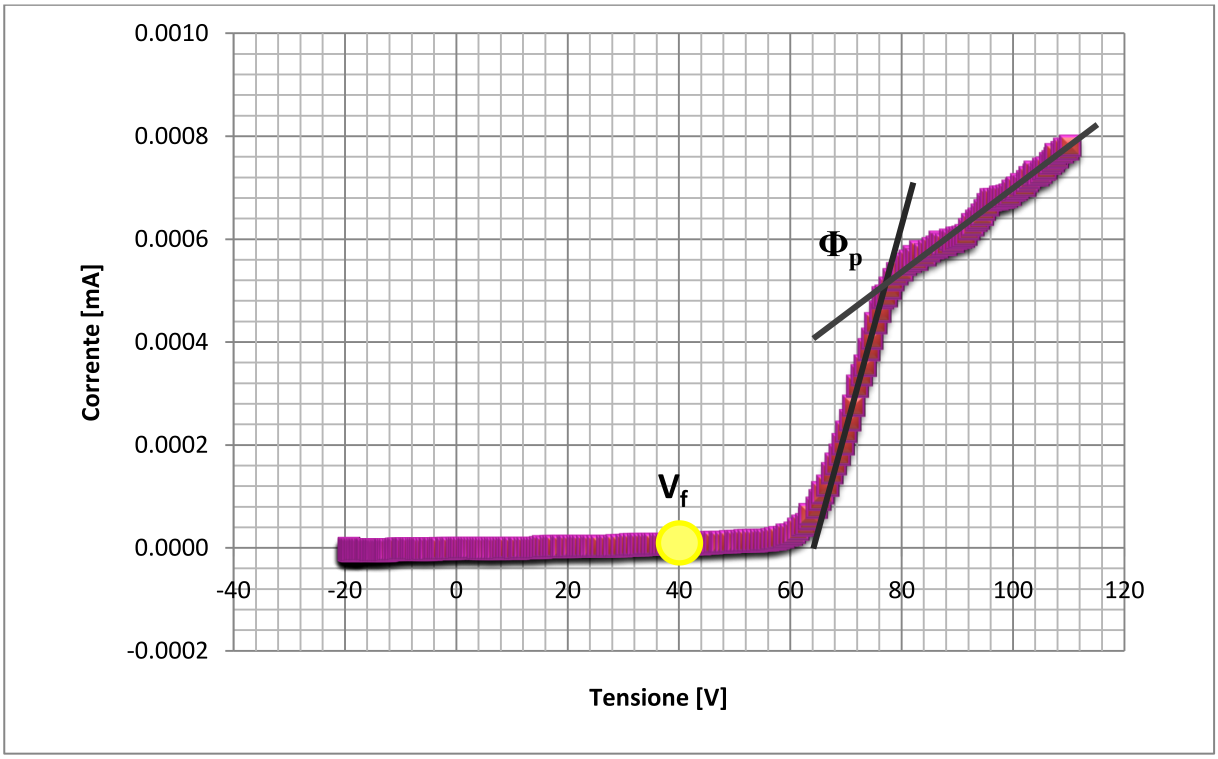

Figure 7.7 LP Characteristic with the Floating and plasma potential

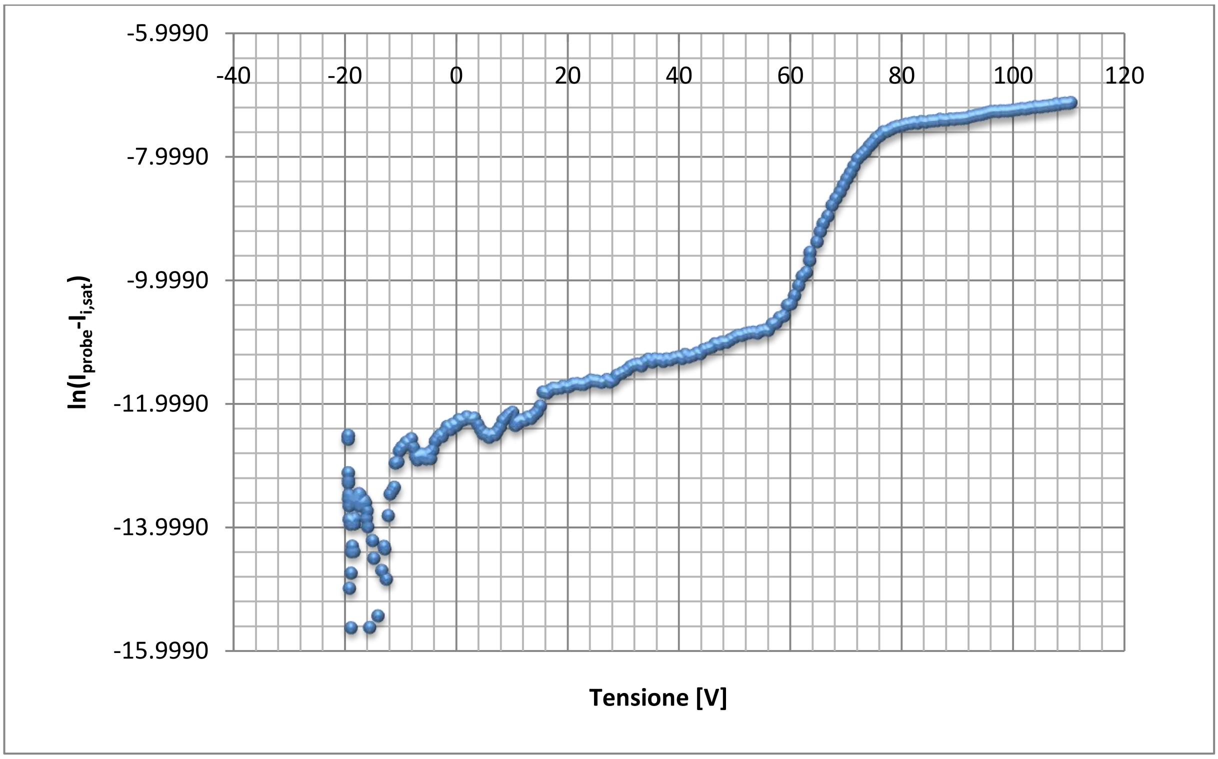

Figure 7.8 ln ($I_{probe} - I_{i,sat}$) VS V_{probe}

7.4.1 Determining electron temperature

Figure 7.8 represents the logarithmic plotting of the electron current. Now the electron current is the probe current minus the ion saturation current: $I_{probe} - I_{i,sat}$ (because we have removed the ion contribution to the total current by subtracting $I_{i,sat}$. The plot decays very rapidly for values of $V_{probe} < V_f$, this is because $\ln(0) = -\infty$. The part of this trace that we are interested in occurs above the floating potential and this is the region presented in the next plot.

Figure 7.9 is a zoomed in version of Figure 7.8 that also includes linear fits to the electron saturation current and inverse temperature. The temperature fit is performed over the range $58 < V_{probe} < 73$ V, which can be seen as the exponentially rising region in figure 6. It is important to choose a bias range over which to perform this fit that represents the temperature dependent increase in probe current. By over-plotting your data with the linear fit it is possible to quickly demonstrate whether the correct temperature region has been identified. According to this temperature fit, the inverse temperature is approximately 0.197, which leads to $T_e = 5.06$ eV.

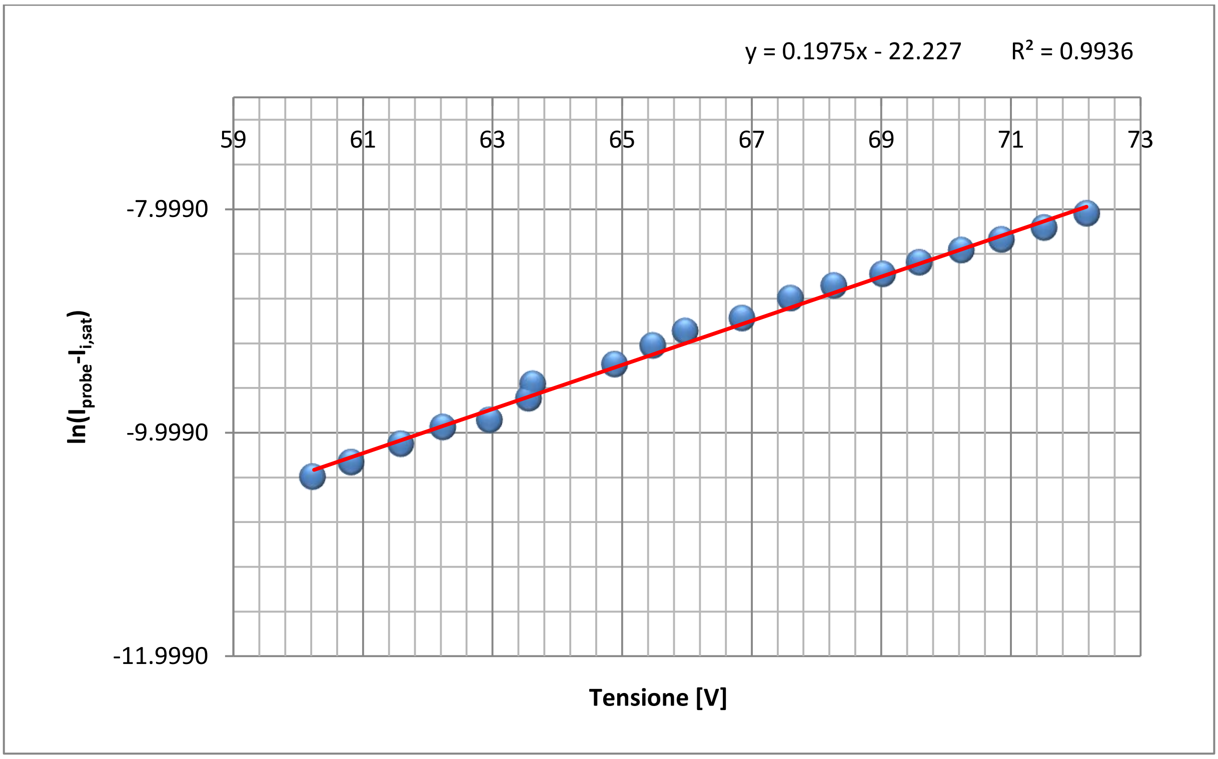

Figure 7.9 Linear best fit from the exponential part of the LP shape

7.4.2 Calculating electron density

Knowing both the electron temperature and the ion saturation current allows us to calculate the electron density using,

$$I_{i,sat} = A_s \exp\left(-\frac{1}{2}\right) q n_e \sqrt{\frac{k_B T_e}{M}} \tag{1}$$

$$n_e = \frac{I_{i,sat}}{q A_s \exp\left(-\frac{1}{2}\right)} \sqrt{\frac{k_B T_e}{M}} \tag{2}$$

where the new terms are M for the ion mass and A_s which represents the area of the probe sheath.

For cases in which the applied probe bias does not greatly exceed the value needed to obtain one of the saturation currents we may approximate the sheath area as the probe tip area. For significant over-biasing this is not a good approximation. In most cases this criteria is met and the approximation is one of the smaller sources of error for probe measurements. The concepts of sheath expansion and Debye length with respect to probe size are worthy of discussion in another effort.

For argon we have M = 6.62×10^{-26} kg. The planar probe used to collect this data has an area of $A_{probe} = 5.06 \times 10^{-6} m^2$ (this is the area of one side multiplied by two because it collects ions and electrons from both faces).

To calculate the electron density it is possible to directly insert the electron temperature in units of electron-Volts by noting the following relationship,

$$\frac{k_B T_e}{q} = T_e[eV] \tag{3}$$

where on the left side the temperature is in units of Kelvin.

For the temperature measured in this setup, T_e = 5.06 eV, the electron density is found to be $n_e = 1.76 \times 10^{15}$ particles per cubic meter.

In the preceding section the properties of our plasma have been determined under a few assumptions. Possibly the most significant assumption was that the plasma source (i.e. electron beam or electron spray) did not affect the IV trace. This is not absolutely correct and it is possible to include effects of the plasma source in our interpretation of the data. From a conceptual standpoint, we may expect that our system contains two separate electron populations. One population is the background plasma (hence referred to as the plasma electrons) and the other is from the plasma source directly (beam electrons).

Since the plasma electrons are generated by ionization from collisions between beam electrons and background neutral gas they cannot possibly be more energetic than the beam electrons.

If there are two separate electron populations in the system, then it may further be expected that the IV trace displays two separate linear regions when plotted in the $\ln|I_{probe} - I_{i,sat}|$ fashion. In order to discern these regions it is necessary to better define the behavior that corresponds to the plasma temperature. If there is a hot electron tail (referred to as a tail because this represents the tail end of the electron velocity, or energy, distribution function), then those electrons will continue to strike the probe even after we have made V_{probe} more negative. If these electrons are affecting the probe measurement, then we should expect to see a second linear region in the logarithmic plot for values of V_{probe} approaching the floating potential. As previously, we must avoid actually considering the floating potential because that is where the $I_{i,sat}$ effects have been subtracted to return a near zero electron current value.

It is not correct to use this temperature to calculate the density and plasma potential of the beam electrons. While they do skew the IV trace, we are still applying the general theory of quasi-neutrality and ion collection to the interpretation of the *IV characteristic*. There are no ions included in the beam distribution and the rest of our probe theory does not apply.

Conceptually, the claim is that the probe collects some of these beam electrons and treats them as plasma electrons. The probe cannot possibly know the difference between the different electrons it collects. To the extent that this simplified notion is true, the beam electrons result in an LP trace that returns a larger temperature than is correct for the plasma that the beam created.

The objective of those experiments was to realize a new type of diagnostic to put side by side to the spectroscopic and microwave diagnostics.

The results reported here it can be compared whit the results found in literature. In this way, we can say our measurement and calculation are pretty correct.

We start the experiments in a stationary plasma with steady conditions, but in the future, we desire to apply this conception in ipersonic flows.

CONCLUSIONS

The MHD interaction in a hypersonic flow had been experimentally investigated. A conical test body had been placed at the exit of the hypersonic nozzle. An ionized Argon flow at a Mach 15 and air flow at Mach 9 had been obtained.

Firstly a characterization of the plasma flow had been realized to obtain the information necessary to define the experimental conditions. Electron temperature and electron number density before the expansion in the nozzle had been esteemed by means of emission spectroscopy. Moreover the electron number density of the plasma at the nozzle exit had been evaluated by means of microwave absorption measurements. These observations showed deviations from thermodynamic equilibrium and a plasma ionization degree frozen during the nozzle expansion.

Numerical simulations of the plasma flow through the nozzle reproduced the experimental conditions with fair agreement. The differences between experimental and numerical results are due to the partial local thermodynamic equilibrium with an electron temperature larger than the gas temperature in the heating chamber in front of the nozzle and to the kinetic model approximation used in the code.

In the MHD interaction experiments, two sizes of the test body were utilized.

A reduction of the sizes of the body was done to keep it inside the uniformity region of the hypersonic flow at the nozzle exit. The electrical connection scheme allowed the short-circuiting of the Faraday current inside the plasma, enhancing the effect of the MHD interaction. Pressure, imaging, and electrical observations were done. The increases of the pressure above the conical surface were caused by the MHD interaction. The pressure increase in this experiment was between 7% and 15%.

The images around the test body showed a rather different flow field in the tests without and with MHD interaction. In the MHD tests, bright rings due to the azimuthally Faraday currents were observed. The Hall field was measured by means of electrical probes placed along the test body lateral surface.

Numerical simulations realized by means of a time dependent two dimensional code at low magnetic Reynolds numbers showed a good agreement with the measurements. The important role of the Hall parameter in the hypersonic MHD interaction process had been demonstrated.

The results of the experiments described in this work show the potential of the MHD technology for its utilization during the re-entry of hypersonic vehicles into the atmosphere.

A new experiment concerning MHD interaction used to change the surface pressure of sharp test article was carried out in Argon at Mach 15 in the framework of the Italian Space Agency CAST programme.

An ionization level similar to the one found in the past tests was observed even if the nozzle flow was non-symmetrical, presumably due to the manufacture process and the fact that it was designed for use in air. The results for pressure, flow-field imaging and electrostatic measurement show some discrepancies with respect to the theoretical expectations and previous tests .

Actually is born a new collaboration with CAST and ESA in the more higher wind tunnel, Capua, Naples.

In the present, the Langmuir probe diagnostic it not frequently use in supersonic flows. For this, in a near future we decide to put side by side this techniques with the spectroscopic and microwave diagnostic for the determination of the plasma parameters, electronic temperature and density.

BIBLIOGRAPHY

[1] H. R. Griem “Principles of Plasma Spectroscopy ” Cambridge University, Press, 2001

[2] L. Leger, E. Moreau and G. Touchard. Control of low velocity airflow along a at plate with a dc electrical discharge. Proc. IEEE-IAS World Conf. on Industrial Applications of Electrical Energy, 2001.

[3] E. Moreau. Airow control by non-thermal plasma actuators. J. Of Appl. Phys., 40:605-636, 2007.

[4] G. Neretti, “Diagnostic techniques for EHD and MHD interaction”, phD Thesis, 2009

[5] C.A. Borghi, M.R. Carraro, and A. Cristofolini. Magnetohydrodynamics interaction in the shock layer of a wedge in a hypersonic flow. IEEE Transaction on Plasma Science, 34(5), 2006.

[6] M.A. Heald and C.B Wharton. Plasma diagnostic with microwaves. John Wiley & Sons, 1965.

[7] M.A. Heald and C.B Wharton. Plasma diagnostic with microwaves. John Wiley & Sons, 1965.

[8] G. Gardet, G. Moulard, M. Courbon, F. Rogemond, and M. Druetta. Evaulation of the rotational temperature in n2 discharges using lowresolution spectroscopy. Meas. Sci. Technol., 11:333{34, 2000.

[9] H. R. Griem. Plasma Spectroscopy. McGraw Hill, 1964.

[10] P.A. Davidson “An introduction to Magnetohydrodynamics” Cambridge Texts in Applied Mathematics

[11] Gad-El-Hak M 2000. Flow Control. Cambridge University Press, 2000.

[12] E. Moreau. Airow controls by non-thermal plasma actuators. Journal Of Applied Physics, 40:605{636, 2007.

[13] B. Arad, Y. Gazit, and A. Ludmirsky. A sliding discharge device for producing cylindrical shock waves. J. of Appl. Physics, 20:360-367, 1987.

[14] S.B. Leonov and D.A. Yarantsev. Mechanisms of flow control by nearsurface electrical discharge generation. AIAA-2005-0780, 2005.

[15] C.S. Kalra, M.N. Shneider, and R.B. Miles. Numerical study of shockwave induced boundary layer separation control using plasma actuators. 46th AIAA Aerospace Science Meeting and Exhibit, AIAA-2008-1095, 2008.

[16] B. Eliasson and U. Kogelschatz. IEEE Trans. Plasma Sci., 19:309, 1991.

[17] Peter A. Davidson, Andre Thess “Magnetohydrodynamics” CISM courses and lectures no. 408

[18] F. Saemoto. The influence of high voltage discharge on flat plate drag at low reynolds number air flow. Master's thesis, Iowa State University, 1992.

[19] J.R. Roth. Industrial Plasma Engineering, volume 1. Bristol: Institute of Physics Publishing, 1995.

[20] J.R. Roth. Industrial Plasma Engineering, volume 2. Bristol: Institute of Physics Publishing, 2001.

[21] A. Schutze et al. The atmospheric-pressure plasma jet: a review and comparison to other plasma sources. IEEE Trans. Plasma Sci., 26:1685-94, 1998.

[22] L.B. Loeb. Electrical Coronas, Their Basic Physical Mechanism. Berkeley University of California Press, 1965.

[23] A.V. Likhanskii, M.N. Shneider, S.O. Macheret, and R.B. Miles. Modeling of interaction between weakly ionized near surface plasmas and gas flow. 44th AIAA Aerospace Sciences Meeting and Exhibit, AIAA-2006-1204, 2006.

[24] A. Veefkind, “Non-equilibrium phenomena in a discharge magnetohydrodaynamics generator” Rotterdam, 1970

[25] J.D. Swift, M.J.R. Schwar “Electrical probes for plasma diagnostic”, London, 1970

[26] M. Mitchner and C.H. Kruger. Partially Ionized Gases. Wiley-Interscience, New York, 1973.

[27] C. O. Laux, T.G. Spence, C.H. Kruger, R.N. Zane “Optical diagnostics of atmospheric pressure air plasmas”, Institute of Physics Publishing, 2003

[28] V. Lago et al “Entry conditions in planetary atmospheres: emission spectroscopy of molecular plasma arcjets” , Journal of Thermophysics and Heat Transfer, 2001

[29] C. Chelouah, E. Marode and G. Hartmann “Measurement of rotational and vibrational temperature in a low-pressure plasma device using the Abel transform and a spectral slit function”, J. Phys. D: Appl. Phys, 27 (1994)

[30] David Pace “Example of Langmuir Probe Analysis” , 2007

[31] G. Crolly and H. Oechsner “ Comparative determination of the electron temperature in Ar and N_2 plasma with electrostatic probes, optical emission spectroscopy OES and energy dispersive mass spectrometry EDMS”, The European Physical Journal Applied Physics, 2001

[32] M.V.V.S. Rao, R.J. Brunt and J.K. Olthoff “Resonant charge exchange and the transport of ions at high electric-field to gas-density ratios (E/N) in argon, neon and helium” Physical Review, 1996

[33] G.J. Womack “MHD power generation : engineering aspects”, London, 1969

[34] Robert L. Merlino “Understanding Langmuir probe current-voltage characteristics”, Department of Physics and Astronomy, University of Iowa, 2007

[35] A. Passaro, D. Baccarella, P. Caredda, A. Cristofolini, G. Neretti, V.M. Granciu "MHD Interaction in a weakly ionization Mach 15 Argon flow", Versailles, 2009

[36] A. Passaro, D. Baccarella, P. Caredda, A. Cristofolini, G. Neretti, V.M. Granciu "Characterization of a new Mach 9 nozzle for the HEAT hypersonic wind tunnel", Versailles, 2009

[37] S.G. Lee et al "direct measurement of plasma flow velocity using a Langmuir probe", University of Madison, 1992

[38] M. Gindrat et al "Characterization of supersonic low pressure plasma jets with electrostatic probes", Institute of Physics Publishing, 2004

[39] Gabriele Neretti and Dan Lev "Langmuir probe Analysis" , 8 April 2007

[40] Marco A. Gigos et al. New plasma diagnosis tables of hydrogen stark broadening including ion dynamics. J. Phys. B: At. Mol. Opt., 1996.

[41] J.S. Shang et al. Magneto-aerodynamic interactions in weakly ionized hypersonic flow. 40th Aerospace Sciences Meeting and Exibit, AIAA- 2002-0349, 2002.

[42] J.S. Shang. Recent research in magneto-aerodynamics. Progress in Aerospace Sciences, 2001

[43] V.A. Bityurin et al. Studies on Mhd interaction in hypervelocity ionized air flow over aero-surfaces. 34th Plasma dynamics and Lasers Conference, AIAA-2003-1365, 2003.

[44] V.A. Bityurin. Mhd activity in Russia. ILG-MHD International Work-shop on Magneto-Hydro-Dynamics Applications: State of the Art, 2003.

[45] A. Cristofolini. Numerical analysis of the Mhd interaction around a sharp cone. Proceedings of the Thirtieth Biennial IEEE Conference on Electromagnetic Field Computation, 2008.